UNIVERSITY OF CALIFORNIA SAN DIEGO

A Multi-Sensor Approach for Near-Shore Tsunami Early Warning and Monitoring Earthquake Effects on Structures

A dissertation submitted in partial satisfaction of the
requirements for the degree
Doctor of Philosophy

in

Earth Sciences

by

Jessie Kate Saunders

Committee in charge:

Jennifer Haase, Chair
Jeffrey Gee
Tara Hutchinson
Diego Melgar
David Sandwell
Peter Shearer

2019

The dissertation of Jessie Kate Saunders is approved, and it is acceptable in quality and form for publication on microfilm and electronically:

_____

_____

_____

_____

_____

_____

Chair

University of California San Diego

2019

DEDICATION

To my family.

EPIGRAPH

An understanding of the natural world and what's in it is a source of not only great curiosity but great fulfillment.

—Sir David Attenborough

TABLE OF CONTENTS

LIST OF FIGURES

LIST OF TABLES

ACKNOWLEDGEMENTS

To quote Michelle Obama, “The important parts of my story... lay less in the surface value of my accomplishments and more in what ungirded them – the many small ways I’d been buttressed over the years and the people who’d help build my confidence over time.” I have been so fortunate throughout my life to be surrounded by family, friends, teachers, and mentors who have helped me throughout my journey.

Firstly, thank you to all of my teachers throughout my education. To Randy Kinavey, who taught me to think critically and face challenges with enthusiasm. To all of my physics professors, who provided me with the fundamentals and taught me the elegance of science. To Jim McClain and Magali Billen, who mentored me during my undergraduate studies and encouraged my interest in geophysics. And to all of my professors at Scripps, who expanded my horizons and solidified my love for Earth Science.

My Ph. D. could not have occurred without my thesis committee. My advisor, Jennifer Haase, has been an integral part of my success. Thank you for always having your door open for me, for supporting my research, and for leading by example to think deeply about my work and to always ask questions. Thank you for encouraging and allow me to pursue activities outside of my specific research projects, including participating in research cruises and field classes, organizing a symposium and seminar series, as well as being a GP Student Representative, Teaching Assistant, and instructor for the Sally Ride Science Summer Academy. These activities have been invaluable experiences that have helped me grow not only in terms of my scientific abilities, but also in my leadership abilities and self-confidence. Diego Melgar, than you so much for all of your guidance and mentorship throughout my time at Scripps. And many thanks to Jeffrey Gee, Tara Hutchinson, David Sandwell, and Peter Shearer for all of your insightful feedback and encouragement of my work.

I also could not have done this without the continued support from members of my first-year cohort: Matthew Cook, John DeSanto, Adrian Doran, and Dara Goldberg. Thank you

all so much for your friendship over these past few years. Special thanks to Matt for being such a fantastic housemate and for sharing Granite with me. Having a resident therapy fluffy to snuggle with has been essential to my well-being. While all of us are moving on to other pursuits, I am so excited to watch your careers blossom. I hope our work allows us to cross paths frequently in the years ahead.

Thank you to Yehuda Bock and members of the Scripps Orbit and Permanent Array Center for supporting me during my first few years at Scripps and for facilitating my interest in earthquake and tsunami early warning. Thank you to the members of the Haase research group for all of your helpful discussions. Thank you to David Chadwell for giving me the opportunity to join the science party in a GPS-Acoustic recovery and redeployment cruise, and thank you to Yuri Fialko for letting me assist in GPS field surveys.

Thank you to Adrian Borsa and Christian Walls for all of your encouragement. Both of you have infectious enthusiasm and have been shining lights during my studies. Thank you for demonstrating how wonderful the Earth Science community can be.

Thank you to fellow IGPP students and postdocs, past and present, for building a rich network of camaraderie and support. Wesley Neely, Ekaterina Tymofyeyeva, Maya Becker, Susheel Adusumilli, Drake Singleton, Nicholas Lau, Joyce Sim, Daniel Trugman, Soli Garcia, and so many others, thank you for helping make IGPP an amazing place to work and learn. I have so many happy memories because of all of you, and I will always look back at my time at Scripps with fondness.

Lastly, and most importantly, I would like to thank my family. Mom and Dad, thank you for always encouraging my curiosity and creativity, and for helping foster my love of learning and passion for science. Kelly, thank you for always being there for me. And Aunt Lori and Kiki, thank you for making San Diego feel like home. I love you all so much.

Portions of this dissertation have been published or are expected to be published in peer-reviewed journals.

Chapter 2, in full, is a reprint of the material as it appears in Geophysical Research Letters: Saunders, J.K., and Haase, J.S., 2018, "Augmenting onshore GNSS displacements with offshore observations to improve slip characterization for Cascadia subduction zone earthquakes," *Geophysical Research Letters*, 45(12), 6008-6017, https://doi.org/10.1029/2018GL078233. The dissertation author is the primary investigator and author of this material.

Chapter 3 is currently being prepared for publication, and is coauthored with Jennifer Haase. The dissertation author is the primary investigator and author of this material.

Chapter 4, in full, is a reprint of the material as it appears in the Bulletin of the Seismological Society of America: Saunders, J.K., Goldberg, D.E., Haase, J.S., Bock, Y., Offield, D.G., Melgar, D., Restrepo, J., Fleischman, R.B., Nema, A., Geng, J., Walls, C., Mann, D., and Mattioli, G.S., 2016, "Seismogeodesy using GPS and low-cost MEMS accelerometers: Perspectives for earthquake early warning and rapid response," *Bulletin of the Seismological Society of America*, 106(6), 2469-2489, https://doi.org/10.1785/0120160062. The dissertation author is the primary investigator and author of this material.

Chapter 5 is part of a larger study currently being prepared for publication which is coauthored with Jennifer Haase, Mohamed Soliman, Omid Khandel, Frankie Martinez, and Imran Sheikh. The dissertation author is the primary investigator and author of the material presented in this chapter.

VITA

2013	B. S. with Honors in Applied Physics, University of California Davis
2014	M. Sc. in Earth Sciences, University of California San Diego
2019	Ph. D. in Earth Sciences, University of California San Diego

PUBLICATIONS

Saunders, J.K., and Haase, J.S., 2018, "Augmenting onshore GNSS displacements with offshore observations to improve slip characterization for Cascadia subduction zone earthquakes," *Geophysical Research Letters*, 45(12), 6008-6017.

Saunders, J.K., Goldberg, D.E., Haase, J.S., Bock, Y., Offield, D.G., Melgar, D., Restrepo, J., Fleischman, R.B., Nema, A., Geng, J., Walls, C., Mann, D., and Mattioli, G.S., 2016, "Seismogeodesy using GPS and low-cost MEMS accelerometers: Perspectives for earthquake early warning and rapid response," *Bulletin of the Seismological Society of America*, 106(6), 2469-2489.

Naliboff, J.B., Billen, M.I., Gerya, T., and **Saunders, J.**, 2013, "Dynamics of outer-rise faulting in oceanic-continental subduction systems," *Geochemistry, Geophysics, Geosystems*, 14(7), 2310-2327

ABSTRACT OF THE DISSERTATION

A Multi-Sensor Approach for Near-Shore Tsunami Early Warning and Monitoring Earthquake Effects on Structures

by

Jessie Kate Saunders

Doctor of Philosophy in Earth Sciences

University of California San Diego, 2019

Jennifer Haase, Chair

In this dissertation, we explore how high-rate displacement data from Global Navigation Satellite Systems (GNSS) sensors can be used in combination with other instrumentation, including strong-motion accelerometers and seafloor geodetic sensors, for applications to near-shore tsunami early warning and structural monitoring of earthquakes. Accurate estimates of fault slip amount and along-strike rupture extent are necessary for determining the coastal extent of high-amplitude tsunami waves. We describe how these values can be estimated using static slip inversions of coseismic data from GNSS sensors used in conjunction with seafloor coseismic data from hypothetical offshore networks. We find that a trench-parallel profile of offshore stations

over the deformation front is an optimized offshore network for this approach. We find that the most accurate slip estimates require horizontal seafloor coseismic data which is currently not feasible to obtain in real time. We then explore how using existing real-time technology – high-rate GNSS as well as onshore and offshore three-component strong-motion accelerometers – could be used in a rapid hypothesis test of modified kinematic slip inversions to confirm the depth of slip location of a megathrust earthquake given that shallow earthquakes produce the most dangerous tsunamis.

If the GNSS sensors and accelerometers are collocated, their data can be combined in a Kalman filter to produce seismogeodetic waveforms: broadband displacements that contain the high-frequency information from the accelerometers and low-frequency and static offset information from the GNSS sensors. As the GNSS and seismic monitoring networks were developed independently, many of these stations are not collocated. We compare with a shake table experiment how Micro-Electro-Mechanical Systems (MEMS) accelerometers perform relative to observatory-grade accelerometers at frequencies of interest, and evaluate their applicability to upgrading existing GNSS sensors into seismogeodetic stations for earthquake early warning and rapid response purposes. This experiment demonstrated the utility of the combined seismogeodetic data for structural monitoring, and we provide an example applying seismogeodetic instrumentation to record in-situ building motion for an aging reinforced concrete structure in Oklahoma, an oil producing region that is currently experiencing high rates of induced seismicity.

Chapter 1

Introduction

1.1 Background

Earthquakes and their effects pose significant threats to public safety and infrastructure. Coastal populations in subduction zone environments are especially vulnerable as these communities live with dual hazards of widespread damage from strong shaking induced by subduction zone earthquakes as well as the tsunamis resulting from these earthquakes. Innovations in methods for precise analysis of high-rate Global Navigation Satellite Systems (GNSS) observations and advances in data telemetry have expanded the use of GNSS from traditional geodesy to include monitoring the effects of these natural hazards. When used in combination with other geophysical instrumentation, GNSS data can provide detailed information about strong ground motion and building damage as well as aid in early warning and rapid response efforts.

The 2011 M_w9.1 Tohoku-oki earthquake and tsunami in Japan is an example where multiple natural hazards affected an area, with both the earthquake and the resulting tsunami having severe societal impacts. Yun and Hamada (2014) interviewed over 1,100 witnesses in areas that experienced severe tsunami inundation, and determined that early evacuation start time is a key factor in survival. As the sizes of coastal populations have been increasing in recent decades

(Center for International Earth Science Information - CIESIN, 2017), more people are becoming exposed to these hazards. Tsunami early warning systems, which detect that a tsunamigenic earthquake has occurred and alert coastal communities before the tsunami arrives, can aid the evacuation process and reduce fatalities.

Tsunamis are generated by offshore earthquakes where seafloor displacement from the earthquake displaces the water above it and creates a wave. The size of the tsunami depends on the extent of seafloor offset, where generally larger subduction earthquakes lead to greater seafloor displacement and larger tsunamis. However, the amount of seafloor displacement also depends on the depth of the rupture along the subduction interface. Figure 1.1 shows an illustrative example using the Okada (1985) analytical solutions for coseismic displacement due to slip on a fault. A shallow subduction rupture produces seafloor coseismic displacement with a sharp concentration of large uplift hear the updip edge of the rupture, where a deeper rupture with the same amount of slip produces a more diffuse pattern of vertical seafloor displacement. These different seafloor displacement patterns generate different tsunamis, where the concentrated seafloor uplift from the shallow rupture produces a higher-amplitude tsunami (Tanioka & Satake, 1996). The tsunami wave from a shallow rupture can be further augmented by its location near the trench, as the horizontal motion of steeply-sloping bathymetry causes additional vertical water displacement (Tanioka & Satake, 1996).

Subduction earthquakes exhibit depth-dependent slip behavior likely due to variations in rheological properties with depth (Lay et al., 2012). Subduction zone earthquakes typically nucleate and rupture in the central portion of the megathrust, around 15-50 km depth. The shallowest portion of the megathrust, from the trench to about 15 km depth, has lower rigidity and high pore pressures associated with subducted sediments and the presence of fluids along the subduction interface, characteristics that can enable aseismic, stable slip (e.g., Byrne et al., 1988; Hyndman et al., 1997; Moore & Saffer, 2001; Wang & Hu 2006). This region is typically considered to have velocity-strengthening frictional properties which can inhibit rupture

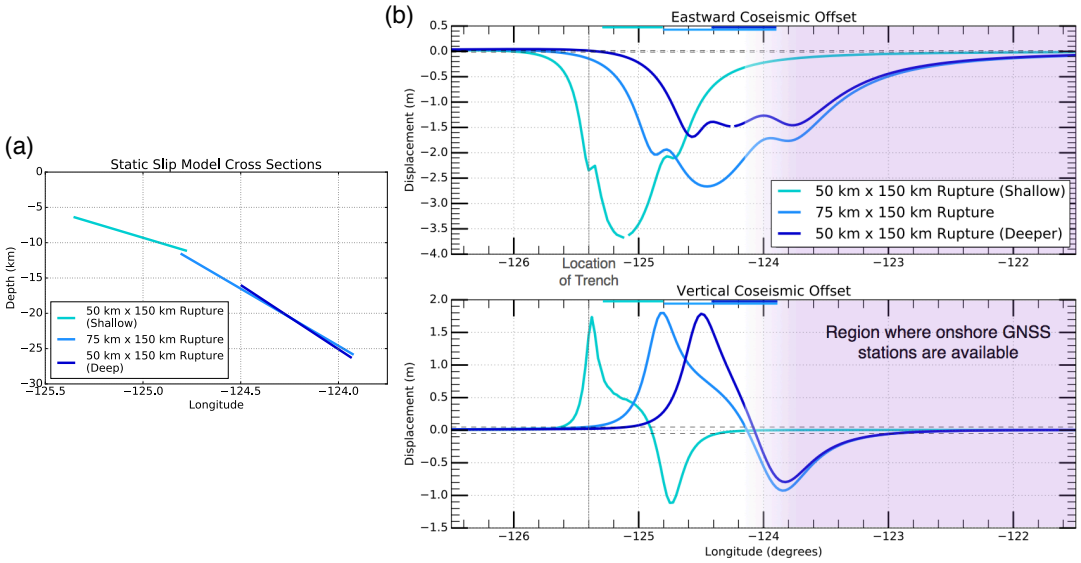

Figure 1.1: Comparison of seafloor coseismic displacements from uniform slip models on different depths of the subduction interface. **(a)** Cross sections of the static slip models. Each model has 5 m uniform slip, and the slip locations are chosen to approximate the Cascadia subduction zone. **(b)** Coseismic deformation along a fault-perpendicular profile. The lines at the top of each subplot indicate the fault extent for each rupture. The approximate region of onshore slip is shaded in purple. Coseismic offsets are computed using the Okada (1985) analytical solution for surface displacement from fault slip in a homogeneous half-space.

propagation near the trench (e.g., Hu & Wang, 2008; Saffer & Tobin, 2011). However, slip inversion and back-projection analyses of megathrust ruptures have demonstrated that some great earthquakes that nucleate in the central portion of the megathrust can propagate updip and rupture into this shallow region. Examples of this type of rupture include the 2015 M_w8.3 Illapel, Chile earthquake (Melgar, Fan et al., 2016) and the extensively-studied 2011 M_w9.0 Tohoku-oki, Japan earthquake (e.g., Fujiwara et al., 2011; Ide et al., 2011; Lay et al., 2011; Yokota et al., 2011; Kodiara et al., 2012; Kozdon & Dunham, 2013; Melgar & Bock, 2015). These studies have shown that the portions of the ruptures in the shallow megathrust tend to be depleted in high-frequency energy, have slower rupture velocities with longer slip durations, and produce large amounts of slip on the fault (Lay & Bilek, 2007; Lay et al., 2012).

Earthquakes have also been observed to rupture exclusively the shallowest portion of the

subduction interface. These earthquakes exhibit the characteristic rupture behaviors for shallow subduction slip described above, and as such, have been dubbed *tsunami earthquakes* because they produce anomalously large tsunamis compared to their seismically-derived magnitudes (Kanamori 1972; Polet & Kanamori, 2000). Two recent tsunami earthquakes, the 2006 M_w7.8 Java and the 2010 M_w7.8 Mentawai, Indonesia, tsunami earthquakes, produced disproportionally large tsunamis with maximum local run-ups of 14 and 9 m, respectively, and resulted in hundreds of fatalities (Ammon et al., 2006; Lay et al., 2011). Often, coastal populations are caught off-guard by the tsunamis from these types of earthquakes because without strong high-frequency shaking, people do not always realize that a large earthquake and tsunami have occurred and that they need to evacuate to higher ground. Near-source tsunami early warning systems could help alert people of these events and aid in evacuation efforts.

The development and evolution of tsunami early warning systems have been largely influenced by damaging tsunamis, where during the aftermath of these disasters societies make adjustments to the systems to mitigate damage and fatalities in future events (Bernard & Titov, 2015). The first tsunami warning center in the United States was created at the Honolulu Seismic Observatory in response to the 1946 Alaska tsunami. This became the Pacific Tsunami Warning Center (PTWC) after the 1960 M_w9.5 Chile earthquake and tsunami prompted the United Nations to create an international warning system for the Pacific basin. Operated by the National Oceanic and Atmospheric Administration (NOAA), the PTWC issues warning alerts to countries around the Pacific when a tsunami is detected. At first, the PTWC relied on data from tide gauges in order to estimate the amplitude of the tsunami, but because tide gauge observations are strongly affected by local bathymetry, false alarm rates were as high as 75% (Yanagi, 1996; Bernard, 2005). This motivated the development of the Deep-ocean Assessment and Reporting of Tsunamis (DART) buoys, seafloor pressure sensors attached to buoys for real-time data telemetry. DART buoys are deployed far from the coast in deep waters $>$2500 m in order to avoid effects from coastal bathymetry and to reduce noise from wind-driven waves (González et al., 2005). The assimilation

of tsunami observations from DART buoys as well as earthquake magnitude estimates from teleseismic and w-phase inversions into tsunami forecast models greatly improved predictions of the tsunami amplitude and arrival times (Titov et al., 2005; Hayes et al., 2011; Hirshorn et al., 2013). After the devastating 2004 M_w9.1 Sumatra-Andaman earthquake, which created a tsunami that killed over 200,000 people (Shearer & Bürgmann, 2009), the DART buoy network was significantly expanded into a global early warning system.

This type of tsunami early warning system is very robust for far-field tsunamis, where the DART buoys are located between the tsunami source and the coastal populations that require early warning. As tsunamis take many hours to travel across ocean basins, these communities tend to have hours in order to prepare for the tsunami. In contrast, populations located on coasts nearest the earthquake only have several to tens of minutes before the tsunami arrives. Often, the tsunami reaches the nearest DART buoy at around the same time as the tsunami arrives at the coast closest to the rupture, making the methods that work for far-field warnings not feasible for near-source tsunami early warning. Indeed, while the evacuation of one million people during the 2015 M_w8.3 Illapel, Chile earthquake and tsunami was considered a great success, the evacuation orders were not issued until after the tsunami first arrived at the coast closest to the epicenter (Melgar, Allen et al., 2016; Tang et al., 2016).

Japan has the longest-operating near-source tsunami early warning system, with the first instrumental system established in Sendai in 1941 (Shuto & Fujima, 2009). The system was earthquake-based from the beginning, where the amplitude of shaking and epicentral distance determined from seismometer data were used to select appropriate warnings from empirical forecasts. In 1952, the Japanese Meteorological Agency (JMA) began national tsunami early warning observations based on this approach, and by 1995, the seismic network in Japan had expanded to where earthquakes could be detected and have their size estimated within 3 minutes of origin time (Bernard & Titov, 2015). Pre-computed earthquake and tsunami scenarios were developed, where warnings are issued based on the scenario that most closely matches the rapid

magnitude and hypocenter calculations from onshore seismic data (Uchiike & Hosono, 1995; Tatehata, 1997; Hoshiba & Ozaki, 2014). However, traditional magnitude estimation techniques from near-field seismic sensors suffer from saturation (Brown et al., 2011), and the magnitude can be grossly underestimated for large earthquakes. This is unfortunately what occurred during the 2011 M_w9.0 Tohoku-oki earthquake and tsunami, where initial magnitude estimates used in early warnings did not rise above M_w8 (Hayes et al., 2011; Hoshiba & Ozaki, 2014).

The resulting underestimation of the amplitude of the 2011 Tohoku-oki tsunami prompted a re-evaluation of the Japanese near-source tsunami early warning system (Tsushima & Ohta, 2014). To prevent underestimations of future tsunamis, a dense array of ocean bottom pressure sensors, strong-motion accelerometers, and seismometers were deployed along the Japan trench (Uehira et al., 2012). These instruments are connected by fiber optic cables that allow for the transmission of observations in real-time. Using this network, direct observations of tsunami amplitude by ocean bottom pressure sensors could be used as the main data for tsunami early warning, bypassing the issue of magnitude saturation from seismic instruments (e.g., Tsushima et al., 2009, 2012; Tanioka, 2018; Yang et al., 2019). However, seafloor pressure data at stations located near and inside the source region are complicated: the seismic waveforms contain acoustic reverberations in the water column as well as the acceleration of the instrument; and the coseismic offset and tsunami are of opposite sign, so these signals obscure each other until the tsunami propagates away from the rupture region (Saito & Tsushima, 2016). Much research still needs to be done to determine how best to process these data to discriminate the tsunami signal in real time and officially incorporate these methods into early warning systems. Additionally, the high cost of installation, maintenance, and operations for a dense cabled seafloor network can be prohibitive for many countries.

A complimentary approach to improving near-source tsunami warning is to improve rapid earthquake source characterization using near-field observations from seismic and GNSS sensors. As earthquake magnitude increases, the amplitude of high-frequency shaking saturates

(Haskell, 1964; Brune, 1970), thus for large earthquakes with M_w >7.5, it is important to obtain low-frequency shaking and static displacement observations to avoid magnitude underestimation using near-field strong-motion data.

After the 2004 Sumatra-Andaman earthquake and tsunami, it was recognized that GNSS observations can provide a useful dataset for tsunami early warning (Blewitt et al., 2006, 2009). By analyzing high-rate GNSS displacement waveforms from large earthquakes, an empirical magnitude-scaling relationship using the peak ground displacement (PGD) and hypocentral distance from GNSS stations was developed that can provide magnitude estimations of large earthquakes without saturation effects (Crowell et al., 2013; Melgar et al., 2015; Ruhl et al., 2018). Pseudo-real-time simulations of GNSS data from the 2011 Tohoku-oki earthquake demonstrate that centroid moment tensors can be computed from rapid coseismic offset estimates, which can then be used to inform finite fault models of the earthquake (Melgar et al., 2012, 2013; Crowell et al., 2012).

Near-source, high-rate GNSS data have been demonstrated to improve slip inversion solutions of recent great earthquakes (e.g., Larson et al., 2003; Ji et al., 2004; Miyazaki et al., 2004; Melgar & Bock, 2015). This has led to the development of earthquake early warning algorithms that use GNSS data to rapidly characterize the earthquake source (Grapenthin et al., 2014; Minson et al., 2014; Crowell et al., 2016). These algorithms incorporate real-time estimations of coseismic offsets (e.g. Allen & Ziv, 2011) into static finite fault inversions to rapidly estimate fault slip.

Simulated real-time demonstrations of these methods have shown that these can provide useful updates to warnings of strong ground motion for large M_w7.5+ earthquakes (Ruhl et al., 2017; Ruhl et al., 2018), and are currently being tested for implementation into the ShakeAlert earthquake early warning system for the West Coast of the United States (Cochran et al., 2018; Kohler et al., 2018). Near-shore tsunami early warning systems could use these slip inversion results as initial conditions to rapid tsunami simulations, which could provide detailed tsunami

wave amplitude and timing information that could inform updates to the initial tsunami alert.

Seismogeodetic combinations of GNSS and accelerometer data increase the sensitivity of the displacement observations and help resolve the source for smaller earthquakes (e.g. Melgar, Geng et al., 2015) as well as for more distant recordings. Traditionally, near-field seismology as well as structural monitoring employ strong-motion accelerometers for observing ground and building motion. Strong-motion accelerometers have a high dynamic range and can avoid clipping when subjected to high-amplitude shaking, which make them a popular instrument for building monitoring and near-field strong-motion seismology. However, instrument rotations and tilts can introduce offset errors in the acceleration time series, which manifest as unphysical drifts when the acceleration data are doubly-integrated into displacements (Graizer, 1979; Iwan et al., 1985; Boore, 1999; 2001; Trifunac & Todorovska, 2001; Boore et al., 2002; Emore et al., 2007; Smyth & Wu, 2007).

In both structural monitoring and strong-motion seismology, accelerometer data is typically integrated into displacements then highpass filtered (Boore & Bommer, 2005). While this removes the baseline drift, this process also removes all information about the coseismic displacement necessary for characterizing large earthquakes in the near field. Low-frequency motions and static displacements are also necessary observations for structural monitoring of tall buildings that have low resonance frequencies as well as for determining building damage using rooftop drift measurements. Traditional baseline correction schemes that try to recover static observations using strong-motion data alone are largely subjective, involving detrending the integrated acceleration data to remove baseline drift effects, and then visually inspecting the resulting acceleration, velocity,and displacement waveforms (Boore, 2011). However, this procedure is only able to recover coseismic displacements to within GNSS error levels $\sim$5% of the time (Emore et al., 2007).

Comparisons with high-rate GNSS data show that automated baseline correction schemes can contain errors beyond the static offset, contaminating displacement waveforms at frequencies

up to 0.5 Hz (Melgar, Bock et al., 2013). These errors can be significantly reduced when collocated GNSS displacements are incorporated into the baseline correction scheme. Using a method that simultaneously solves for the acceleration baseline offsets and the integrated displacements, Emore et al. (2007) found that even 30 s GNSS observations are sufficient for constraining the integrated displacements. Another approach is to use a multi-rate Kalman filter, a method that optimally combines the high-frequency shaking information from the strong-motion accelerometers and the low-frequency shaking information from the GNSS observations (Smyth & Wu, 2007; Bock et al., 2011).

1.2 Scientific Objectives

This dissertation focuses on combining observations from multiple instrument types in order to provide broader views of shaking behavior for use in tsunami early warning and structural monitoring. We use synthetic rupture scenarios to explore how a multi-sensor approach using GNSS sensors, accelerometers, and ocean-bottom pressure sensors can help determine the location of slip for a tsunamigenic subduction zone earthquake and aid near-source tsunami early warning efforts. We focus on the Cascadia subduction zone for this work, as it has a high tsunamigenic earthquake hazard as well as a dense network of real-time monitoring instruments. We also discuss how seismogeodetic data from GNSS sensors and strong-motion accelerometers can be used in structural monitoring, and we apply this approach to a building in Oklahoma where we record the building response to shaking from earthquakes in situ. The main objectives of this dissertation are as follows:

1. Examine how offshore coseismic observations can augment onshore GNSS displacements and improve static slip inversion results;

2. Determine whether the early part of near-field, high-rate GNSS displacement waveforms can distinguish shallow subduction zone slip versus only deep slip in order to address the

potential hazard of tsunami earthquakes;

3. Determine whether the addition of offshore data from ocean-bottom pressure sensors and strong-motion accelerometers installed on the seafloor significantly improve these rapid slip and tsunami scenarios;

4. Determine the sensitivity of combined GNSS/low-cost accelerometer sensors for earthquake early warning and rapid response applications; and

5. Examine how combined GNSS/accelerometer sensors can be applied to structural monitoring in a region of high induced seismic activity.

1.3 Outline of the Dissertation

This dissertation is comprised of six chapters. Chapters 2 and 3 examine how GNSS precise point positioning used in conjunction with strong-motion accelerometers and seafloor instrumentation can improve rapid slip characterization for $M_w \sim 8$ megathrust earthquakes. The rupture location along the subduction interface for earthquakes of this size greatly affects the size of the resulting tsunami, where shallow ruptures close to the trench can generate a tsunami much larger than expected for the earthquake's magnitude. Accurately estimating the slip location and slip amount within the first few minutes after a megathrust earthquake can reduce uncertainties in the predicted tsunami and has the potential to improve evacuation alerts. We focus on the Cascadia subduction zone, which has a dense real-time GNSS network as well as several ocean bottom pressure sensors streaming data in real time through fiber optic cable networks. We first examine in Chapter 2 how static slip inversions of synthetic data from hypothetical $M_w 8$ earthquakes at varying depths can be improved by using coseismic displacement estimates from both onshore GNSS as well as offshore instruments. We determine an optimal offshore cabled network configuration that can provide accurate estimates of the along-strike rupture extent, a

metric that strongly affects where the high-amplitude tsunami waves will impact the coastline.

In Chapter 3, we explore how the early portion of the GNSS displacement waveform, from the P-wave to PGD, can be used in kinematic slip inversions to provide rapid estimates of rupture characteristics with currently available instrumentation. Like in Chapter 2, we use synthetic data from a suite of kinematic rupture scenarios in Cascadia to test our approach. We apply depth constraints on the slip inversions in a hypothesis test to determine whether the rupture is likely shallow or deep. We assess whether approximations made about the timing of the rupture using available hypocenter and magnitude estimates can reduce the size of the inversion while still robustly determining the potential for shallow slip. We also test the improvement in resolving rupture parameters by including additional data in the slip inversions: onshore seismogeodetic velocities from GNSS sensors collocated with strong-motion accelerometers, and offshore velocities from seafloor accelerometers.

The seismogeodetic combination produces broadband displacements and velocities that contain the high-frequency shaking information observed by the accelerometer as well as the low-frequency shaking and static offset information observed by the GNSS sensors. Due to different instrument site requirements and the independent development of the seismic and geodetic networks, many of the existing instruments are not collocated. In Chapter 4, we examine how low-cost Micro-Electro-Mechanical Systems (MEMS) accelerometers can provide a robust option for densifying the seismogeodetic network for earthquake early warning and rapid response applications by installing these sensors at existing GNSS stations. As these MEMS accelerometers are less sensitive to ground motion compared to observatory-grade accelerometers, we need to assess the reliability of the MEMS accelerometer observations during strong motion. We use an experiment on the Network for Earthquake Engineering Simulation (NEES) Large High-Performance Outdoor Shake Table (LHPOST) at UC San Diego to compare the performance of MEMS accelerometers with observatory-grade accelerometers at frequencies of interest for earthquake monitoring and engineering purposes. We also observe four M$\sim$4 earthquakes on

seismogeodetic field stations with the first generation of these MEMS accelerometers, demonstrating that the lower limit of sensitivity for MEMS accelerometers with this dynamic range is suitable for earthquake early warning and rapid response purposes.

The LHPOST experiment described in Chapter 4 was in conjunction with an assessment of a novel dampening system to reduce the amplitude of shaking for tall buildings (Fleischman et al., 2015), and demonstrated the utility of seismogeodetic instrumentation for observing the response of buildings to seismic shaking. We seek to use this instrument combination to record structural response to seismic shaking in situ, and in Chapter 5, we describe a building monitoring project in Oklahoma, a region experiencing high seismicity from anthropogenic sources. We have instrumented a 12-story, aging reinforced-concrete structure on the Oklahoma State University Campus, and have estimated the building's response to ten M4+ earthquakes that have occurred in the first year of monitoring. We use waveforms from one of these earthquakes in a finite element simulation of the building to assess the accuracy of the simulation that will be used to determine the building's behavior during severe ground shaking. The severe ground shaking waveforms that will be input to this finite element model will be synthesized from semi-stochastic kinematic rupture model scenarios from a nearby M_w6 earthquake. We describe how we create these kinematic rupture models. To determine that the approach is suitable for this region, we compare ground motion characteristics from synthetic waveforms of rupture scenarios similar to the 2016 $M_w5.8$ Pawnee, Oklahoma, earthquake with observations as well as with a regional ground motion prediction equation. We finish the dissertation in Chapter 6 with some concluding remarks.

Chapter 2

Augmenting onshore GNSS displacement with offshore observations to improve slip characterization for Cascadia subduction zone earthquakes

2.1 Abstract

For the Cascadia subduction zone, $M_w \sim 8$ megathrust earthquake hazard is of particular interest because uncertainties in the predicted tsunami size affect evacuation alerts. To reduce these uncertainties, we examine how augmenting the current Global Navigation Satellite Systems (GNSS) network in Cascadia with offshore stations improves static slip inversions for $M_w \sim 8$ megathrust earthquakes at different rupture depths. We test two offshore coseismic data types: vertical-only bottom pressure sensors, and pressure sensors combined with GNSS-Acoustic aided horizontal positions. We find amphibious networks best constrain slip for a shallow earthquake compared to onshore-only networks when offshore stations are located above the

rupture. However, inversions using vertical-only offshore data underestimate shallow slip and tsunami impact. Including offshore horizontal observations improves slip estimates, particularly maximum slip. This suggests that while real-time GNSS-Acoustic sensors may have a long development timeline, they will have more impact for static inversion-based tsunami early warning systems than bottom pressure sensors.

2.2 Introduction

The Cascadia subduction zone, where the Juan de Fuca plate is subducting under the North America plate, is a region of high earthquake and tsunami hazard for the west coast of the United States. While no great earthquakes of $M_w \geq 8$ have occurred in the Cascadia subduction zone during its documented history beginning around 1790 (Atwater et al., 1995), paleoseismic studies using turbidites, shoreline subsidence, and tsunami deposits confirm the region is capable of great earthquakes (Goldfinger et al., 2003, 2012; Nelson et al., 2006). In addition to $M_w \sim 9$ events, the paleoseismic record shows that the southern portion of Cascadia offshore Oregon experiences $M_w \sim 8$ tsunamigenic earthquakes (Goldfinger et al., 2012).

The local tsunami impact from M_w 8 megathrust earthquakes is strongly dependent on earthquake depth. Rupture of the shallowest portion of the subduction interface, from $\sim$15 km depth to the trench, can produce long-duration earthquakes that have anomalously low seismic moment and short-period energy release accompanied by large coseismic offsets (Lay et al., 2012; Lay & Bilek, 2007). Such events are called "tsunami earthquakes" due to their disproportionately large tsunamis compared to their seismically-determined magnitude (Kanamori, 1972; Polet & Kanamori, 2000). In Cascadia, it is difficult to determine shallow rupture potential as the pattern of subduction interface coupling is not well-constrained near the deformation front due to the lack of present-day seismicity and long-term offshore geodetic data (Pollitz & Evans, 2017; Schmalzle et al., 2014). However, local tsunami warning systems should be prepared for a shallow

megathrust rupture.

Standard warning level thresholds for tsunami early warning used by the National Oceanic and Atmospheric Administration Tsunami Warning Centers are tsunami wave heights of 30 cm, 1 m, and 3 m (Whitmore et al., 2009). M_w8 subduction zone earthquakes can generate tsunamis that fall within the 1-3 m range and exceed 3 m in the case of shallow rupture. It is therefore important to correctly estimate tsunami wave heights in order to issue appropriate warnings. Early warning systems that rely only on hypocenter and magnitude estimates using seismic sensors may miscalculate the potential impact of tsunami earthquakes because the lack of high-frequency energy may underestimate earthquake magnitude (Kanamori, 1972). Magnitude estimates using long-period W-phase are less susceptible to this miscalculation (Kanamori & Rivera, 2008; Zhao et al., 2017), but near-field GNSS data provide observations that can allow for detailed tsunami warning models in faster time frames (Melgar, Allen, et al., 2016).

Near-source GNSS displacement data measure low-frequency motions and coseismic offsets helpful for characterizing tsunamigenic earthquakes (Melgar et al., 2012). Magnitude can be rapidly estimated through peak ground displacement (PGD) scaling (Crowell et al., 2013; Melgar et al., 2015), and the pattern of onshore coseismic displacement can be used to estimate downdip rupture extent (Singh et al., 2012). The Pacific Northwest has a dense, real-time GNSS network that is being incorporated into early warning systems that use rapid coseismic offsets estimations to compute finite fault slip distributions (Crowell et al., 2016; Grapenthin et al., 2014; Minson et al., 2014). These fault slip distributions can be input to tsunami simulations to provide tsunami wave height estimates for early warnings. However, the one-sided distribution of data from land-based networks may be unable to uniquely determine the slip distribution of a M_w8 rupture, especially for a shallow tsunami earthquake. Measurements of offshore coseismic displacement could help reduce this non-uniqueness, if strategically placed.

In this project, we examine how augmenting the current real-time GNSS stations in the Pacific Northwest with offshore sensors can improve the static slip estimates of shallow

ruptures for tsunami early warning. At the 2017 Offshore Geophysical Monitoring in Cascadia Workshop (University of Washington, 2017; report available at www.cascadiaoffshore.org), various network configurations were discussed along with different offshore instrument types, including preliminary analysis of this project (Saunders & Haase, 2017). In addition to GNSS-Acoustic (GNSS-A) sensors, fiber-optic strainmeters (Blum et al., 2008; Zumberge, 1997) were considered as potential sources of horizontal deformation information. Ocean bottom strong-motion accelerometers were also discussed. These could be useful for kinematic slip inversions, but are excluded in this study because of the difficulty estimating coseismic displacements due to baseline offset integration errors (Boore & Bommer, 2005). Linking these sensors on a cabled array would provide real-time data streaming, which adds constraints on network design and additional motivation for this sensitivity study.

Here, we test multiple offshore station configurations and different offshore coseismic data types, using ocean bottom pressure and GNSS-A sensors as our hypothetical offshore instrumentation. As these instruments have different expected data uncertainties, we use synthetic slip models for our analysis. This also allows us to assess the influence of these data types and their uncertainties on the resulting rapid tsunami forecast for these slip models. The station configurations examined here do not form an exhaustive list, but capture the main differences between proposed network concepts for static slip inversion.

2.3 Methods

2.3.1 Slip Models and Tsunami Prediction

We consider two synthetic ruptures of M_w8.0 with dimensions chosen using the empirical scaling relationships of subduction zone earthquakes by Blaser et al. (2010). The fault model is a 10 km uniform grid approximation of the McCrory et al. (2012) 3-D Cascadia slab geometry. Both slip models have uniform 5 m slip with linear slip taper at the rupture edges (Figure 2.1).

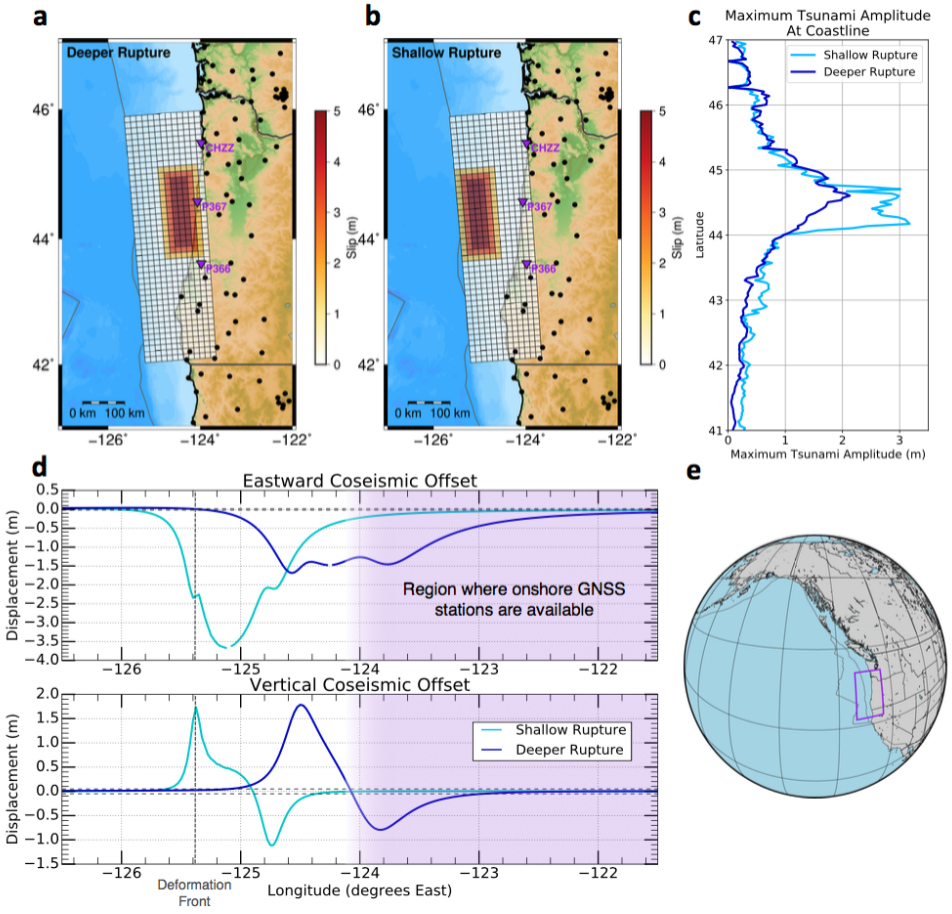

Figure 2.1: Input slip models for the **(a)** deeper rupture and **(b)** shallow rupture. **(c)** Maximum tsunami amplitude at the coastline for the input ruptures. **(d)** Eastward and vertical coseismic offsets for the input slip models along a transect that runs through the center of the ruptures. The region where onshore GNSS stations are available is shaded in purple. **(e)** Location of the modeling region.

The first slip model is between 20-30 km depth, which produces coastal subsidence similar to paleoearthquake observations (Atwater et al., 1995). Coseismic offsets are computed using Green's functions from the frequency-wavenumber approach of Zhu and Rivera (2002) at the low-frequency limit with a 1-D multi-layered Earth structure model for Cascadia (Gregor et al., 2002). The second model places slip in the shallow subduction interface above 15 km, the depth range of observed tsunami earthquakes (Lay et al., 2012). The shallow rupture produces little coseismic displacement onshore, which will make it difficult for land-based instrumentation alone to characterize the rupture region.

We then compute wave amplitudes at the coastline from tsunamis generated by the input ruptures using the GeoClaw open-source software, which solves the two-dimensional shallow water equations using a finite volume approach (Berger et al., 2011; LeVeque et al., 2011). We use the Shuttle Radar Topography Mission (SRTM) 15+ dataset (Sandwell et al., 2014) as the input bathymetry in our tsunami simulations because input bathymetry with larger grid spacing can produce spurious coastal wave height estimates (Figure 2.S1). We forward compute vertical coseismic offsets for a grid on the seafloor and interpolate to the SRTM15 grid spacing before input to the GeoClaw simulations, where we assume instantaneous seafloor uplift. We also include the vertical displacement of water caused by horizontal motion of steeply-sloping bathymetry, which can contribute significantly to the tsunami if slip occurs near the deformation front (Tanioka & Satake, 1996). The deeper and shallow slip models generate tsunamis with maximum wave heights of 2 m and 3 m at the coastline, respectively (Figure 2.1), which would trigger different evacuation levels.

2.3.2 Station Configuration and Offshore Data Types Tested

We test five station configurations in this study (Figure 2.2). The first is the existing real-time GNSS network in the Pacific Northwest. This network is comprised of the Plate Boundary Observatory (Herring et al., 2016) and the Pacific Northwest Geodetic Array (Popovici et al., 2015). The second configuration is onshore GNSS augmented with a dense offshore network with 0.4° station spacing similar to the Japanese S-net system (Uehira et al., 2012). The third and fourth networks are the GNSS network with offshore trench-perpendicular transect profiles with 2° and 1° latitude profile spacing, respectively. And the fifth network is the GNSS network with an offshore trench-parallel line of stations above the deformation front.

For each rupture, synthetic coseismic offsets are computed at all stations, and Gaussian noise is added before inversion. We assume GNSS errors with standard deviation 1.5 cm in the horizontal and 5 cm in the vertical for the onshore coseismic displacements assuming a

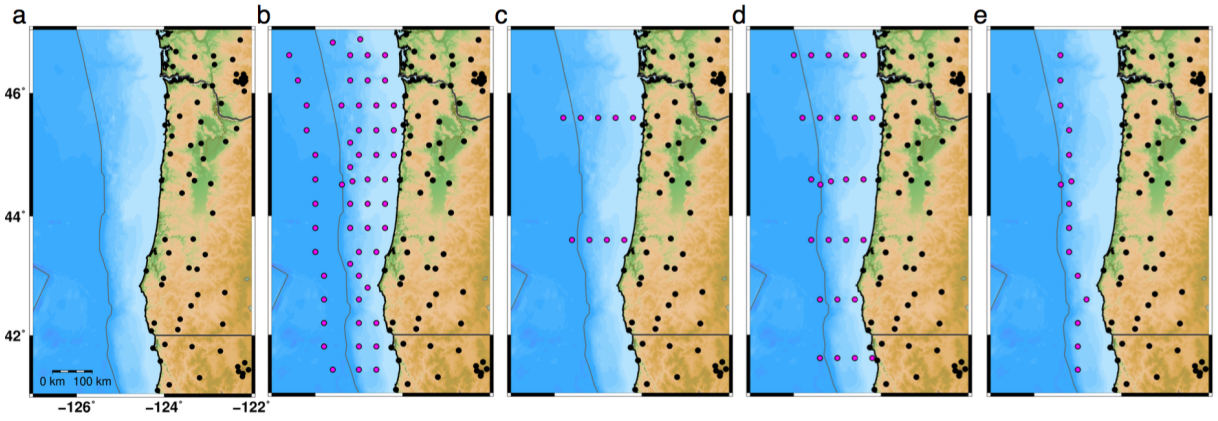

Figure 2.2: Networks considered in this study. Black dots show existing real-time GNSS stations locations and magenta dots show hypothetical offshore instrument locations. **(a)** GNSS-only configuration. The other networks are the GNSS network augmented with the following offshore networks: **(b)** a configuration similar to the S-net cabled array offshore Japan, **(c)** a sparse transect profile configuration, **(d)** a dense transect profile configuration, and **(e)** a trench parallel profile configuration.

high-rate, real-time precise point positioning solution (Geng et al., 2013). For offshore coseismic data, we assume errors with standard deviation 5 cm in the horizontal based on GNSS-Acoustic observations (Chadwell, 2016) and 1.5 cm in the vertical based on seafloor pressure sensor accuracy (Tsushima et al., 2009).

We test two types of offshore coseismic data configurations in the static slip inversions: vertical-only and three-component. Vertical coseismic offsets have been measured accurately offshore using existing seafloor pressure sensors (Bürgmann & Chadwell, 2014; Saito & Tsushima, 2016). Such data can be obtained in near real-time through cabled systems like the S-net in the Japan subduction zone, DO-NET in the Nankai subduction zone (Kawaguchi et al., 2008), and the OOI and NEPTUNE cabled arrays for the Cascadia subduction zone (Kelley et al., 2014). Horizontal coseismic data could be acquired by a GNSS-Acoustic (GNSS-A) system composed of acoustic transponders on the seafloor linked to a GNSS receiver on the sea-surface directly above the transponders (Bürgmann & Chadwell, 2014). GNSS-A receivers deployed along the Japan Trench recorded $\sim$50 m of horizontal displacement near the trench after the 2011 M_w9.0 Tohoku-oki earthquake (Fujiwara et al., 2011). These observations were key in confirming that

the Tohoku-oki earthquake ruptured into the shallow megathrust. Real-time observations of these large horizontal displacements would be very useful in determining the rupture location during a megathrust earthquake. GNSS-A networks such as the one in the Nankai subduction zone are surveyed in annual campaigns (Tadokoro et al., 2012; Yokota et al., 2015), but the addition of buoys or remotely operated vehicles could help develop real-time capabilities in the future (Chadwell, 2016).

2.3.3 Static Slip Inversion Methodology

In the forward problem, coseismic displacements can be computed given an earthquake slip model and Green's functions that relate slip on a buried fault to surface deformation over a layered half space. These Green's functions can also be used to invert for earthquake slip if the coseismic deformation is known. We perform static slip inversions using the open-source MudPy inversion code (Melgar & Bock, 2015) with the assumptions that slip is oriented within 45° of the dip-slip direction and occurs on a known fault geometry, the subduction interface. This allows the static slip inversion problem to be solved using a non-negative least squares approach (Trifunac, 1974). We employ Laplacian spatial smoothing, where the optimal smoothing weight is objectively chosen using the minimization of Akaike's Bayesian Information Criterion (ABIC) given a range of inversion results with different smoothing parameter weights (Akaike, 1998; Ide et al., 1996). We perform slip inversions for every combination of rupture, station configuration, and offshore data type using 15 realizations of observational noise. The resulting fault slip estimates are used to compute the vertical seafloor deformation and input to the tsunami calculation. We compare the slip and tsunami wave height estimates at the coastline from the slip inversion results to that produced by the input slip models to determine which offshore network and offshore data type provide the most valuable additions to the GNSS network.

A comparison of model resolution matrices for these configurations is included in the Supplementary Information (Text S1, Figures 2.S2-S6). While these are informative, they do not

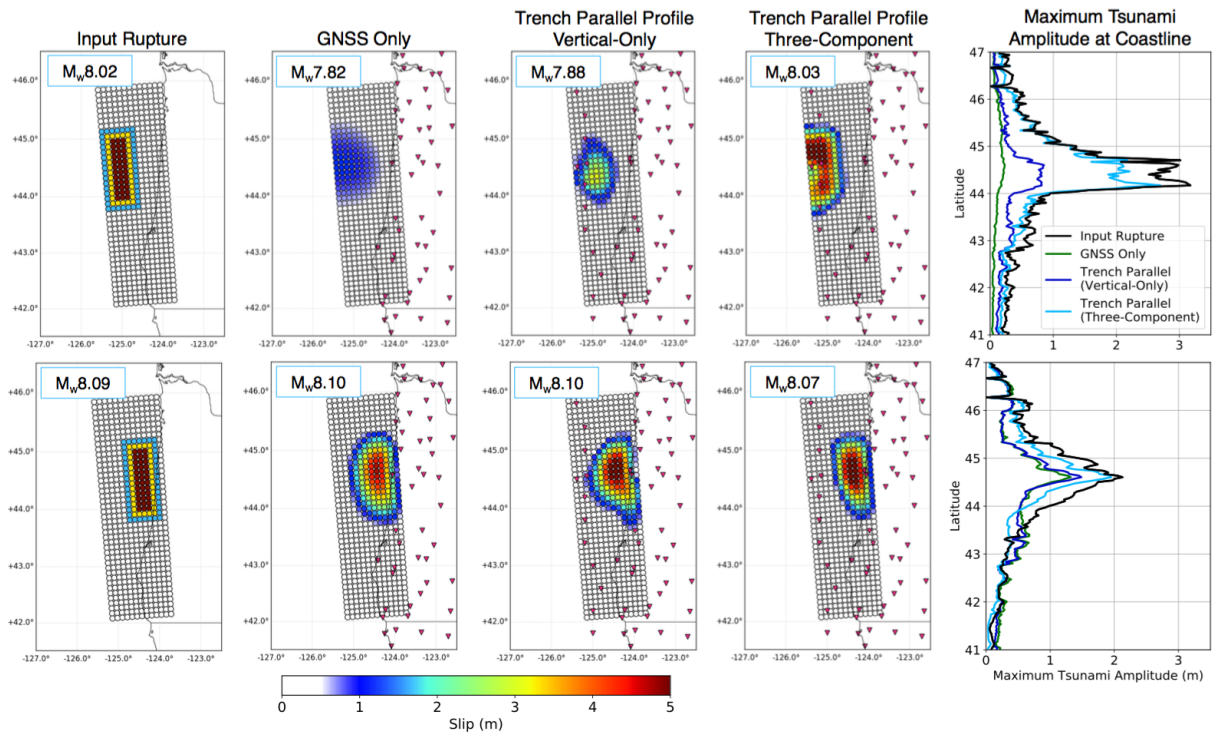

Figure 2.3: Comparison of input ruptures, slip inversion results using GNSS-only and the Trench Parallel Profile offshore configuration, and their resulting tsunamis. The top row shows the shallow rupture, and the bottom row shows the deeper rupture.

consider the impact of data uncertainty. The optimal solution is determined objectively based on the ABIC criterion, which considers the relative size of the data uncertainties with the deformation amplitudes when selecting the regularization weighting. An important point we consider in this study is that the data types have different levels of uncertainty that would affect the slip inversion results, and affect the choice of offshore network that is implemented.

2.4 Results

The quality of the retrieved slip inversion and tsunami results are compared among offshore data types (vertical-only and three-component) for each rupture. Figure 2.3 shows one realization of slip inversion results using GNSS-only and the Trench Parallel Profile configurations. Example static slip inversion results for all station configurations and both offshore data types are

shown in Figures 2.S7 and 2.S8 for the shallow and deeper ruptures, respectively. The tsunami wave height estimates along the coastline for these inversion solutions are shown in Figure 2.S9. For the deeper rupture, all station configurations recover the slip distribution and maximum slip. Some smearing of slip is present in the updip direction for the GNSS-only and vertical-only offshore inversion results that is reduced by having three-component offshore data directly updip of the rupture (Figures 2.3, 2.S8).

For the shallow rupture, the GNSS-only inversion correctly places slip in the shallow region, but significantly underestimates the amount of slip due to the lacking stations near the rupture (Figure 2.1d). This is similar for the sparse transect profiles. When there are stations located directly above the rupture, maximum slip improves. However, slip is consistently underestimated when using vertical-only offshore data compared to three-component offshore data. The along-strike extent is not recovered unless there are multiple offshore stations above the rupture in the along strike direction.

We provide a quantitative measure of the differences among network configurations in Figure 2.4. The quality of the solution is measured in four ways: 1) rms difference between recovered and input fault slip (2.4a); 2) difference between recovered and input maximum fault slip (2.4b); 3) difference between maximum tsunami amplitude at the coast for the recovered and input slip models (2.4c); and 4) percentage of coastline hit by high amplitude waves for recovered relative to input fault slip tsunami simulations (2.4d). These measures are plotted with respect to the number of additional offshore stations, where the error bars are determined from the standard deviation of the parameters from all noise realizations. These figures show that there is significant improvement in all measures for the shallow rupture by incorporating three-component data, and can be accomplished with only a moderate number of stations.

Utilizing offshore data brings maximum wave height estimates to within 0.5 m (70%) for vertical-only data, and three-component offshore networks with stations located above or directly up-dip of the rupture estimate maximum wave height to within 0.25 m (90%) for the deeper

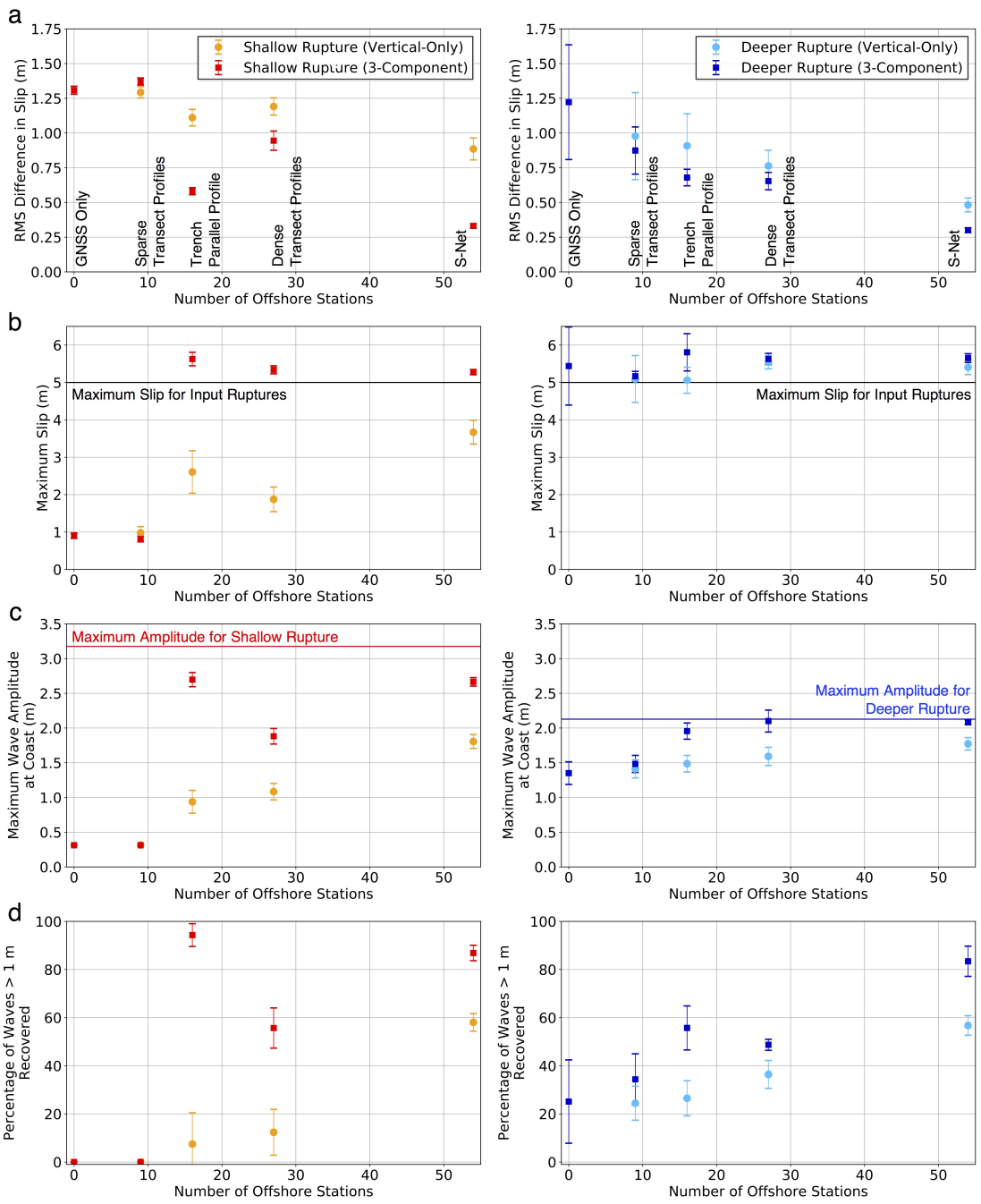

Figure 2.4: Comparison of slip inversion results using the two offshore coseismic data types. Left panels compare configurations for the shallow rupture and right panels for the deeper rupture. Inversion solutions using vertical-only offshore data are in lighter-colored circles while those using three-component offshore data are in darker-colored squares. Rows show the comparison of **(a)** rms difference in slip, **(b)** maximum slip, **(c)** maximum tsunami wave heights, and **(d)** percentage of high amplitude waves >1 m at the coastline recovered in the tsunami estimates. All comparisons are plotted against the number of additional offshore stations in the networks. Error bars indicate the standard deviation of these values from all noise realizations.

rupture. For the shallow rupture, the tsunami simulations based on GNSS-only and offshore data that lack sites above the source (the Sparse Transect Profiles) severely underestimate tsunami impact, estimating maximum wave height at $<10\%$ of the input model, because maximum slip is not recovered. Tsunami simulations improve when using the other offshore configurations, but still tend to underestimate maximum tsunami wave height. Adding three-component offshore data improves maximum wave height estimates by at least 20% compared to estimates using vertical-only offshore data.

In addition to the maximum tsunami wave height at the coastline, the coastal extent of high-amplitude waves is a useful metric for determining the potential tsunami evacuation region. Figure 2.4c shows that offshore networks with multiple stations located above the rupture in the along-strike direction (the S-net and Trench Parallel Profile configurations) are able to estimate the extent along the coastline hit by the highest amplitude tsunami waves (>1 m) when using three-component offshore data. This is most obvious for the shallow rupture. The ability of the network geometry to constrain the percentage of coastline affected with >1 m waves is quantified in Figure 2.4d.

2.5 Discussion

Among the networks investigated, increasing the number of offshore stations generally improves slip inversion results in terms of matching maximum slip and rms difference as well as improving tsunami wave height estimates along the coast. For the deeper rupture, adding additional offshore stations does not significantly improve slip results and tsunami simulations with either offshore data type due to the rupture's proximity to onshore stations. However, three-component offshore data directly above the rupture region are required to obtain the most improvement in slip and tsunami estimates for the shallow rupture.

The S-net configuration produces the most accurate slip inversion solutions and tsunami

simulations, but maximum tsunami wave height is still underestimated for the shallow rupture by 15% for three-component offshore data and 45% for vertical-only offshore. Transect profile spacing of 1° latitude improves the likelihood that sites will be located over the rupture plane for a M_w8.0 earthquake compared to transects with greater spacing. While this configuration will estimate maximum slip for fault patches underneath the offshore stations using three-component coseismic data, the profiles are too sparse to be able to accurately determine along-strike rupture extent, and underestimates the coastal extent that will experience tsunami amplitudes $>$1 m by 45%.

The preferred offshore station configuration is the trench parallel profile because it provides the most improvement in the shallow slip solution while also limiting the number of offshore stations. The trench parallel profile configuration captures the along-strike rupture extent, and when using three-component offshore data, the resulting tsunami computation accurately estimates the coastal impact of tsunami waves with $>$1.0 m amplitude and produces comparable tsunami amplitudes to the S-net configuration. Additionally, such GNSS-A stations in combination with onshore stations will provide robust long-term plate boundary deformation measurements above the shallow subduction interface. These offshore observations are necessary for determining the locking pattern of the Cascadia subduction interface (Pollitz & Evans, 2017; Schmalzle et al., 2014).

An additional verification step that could be implemented on a practical timescale for early warning is to confirm shallow megathrust slip using high-rate onshore GNSS displacement waveforms. To explore this, we examine 1 Hz synthetic displacement waveforms for the four ruptures shown in Figure 2.3: the input model of shallow slip, the slip inversion results using GNSS-only, and the two trench parallel profile inversion results (vertical and three-component; Figure 2.5). We develop the static slip model into a kinematic rupture following the approach of Melgar et al. (2016) and Graves and Pitarka (2010) (Text S3). As expected, all ruptures produce similar coseismic offsets, but there are deterministic differences in the early portion

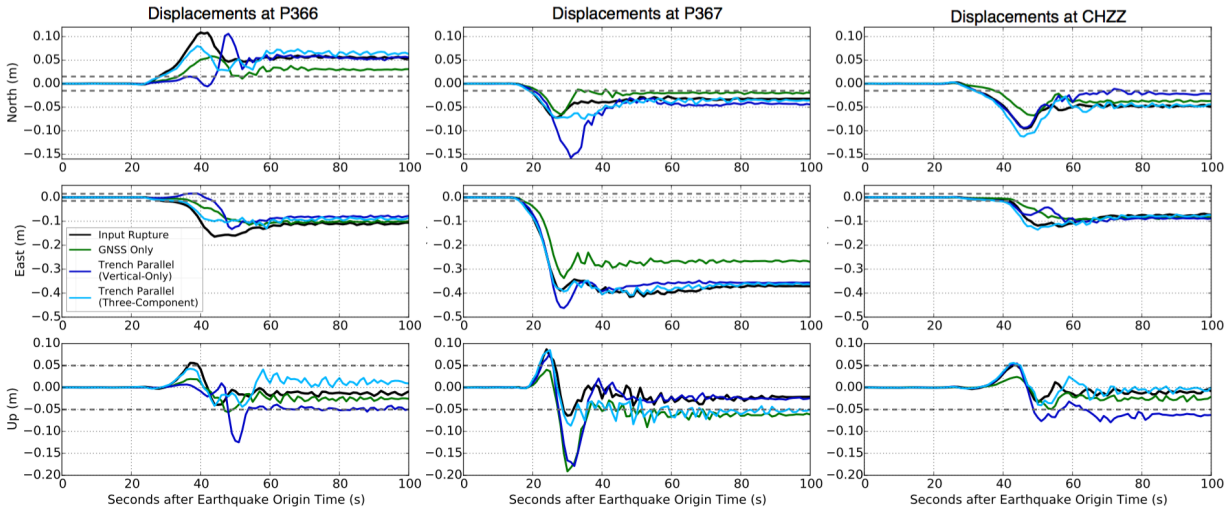

Figure 2.5: Comparison of displacement waveforms for the shallow rupture model and three static inversion results shown in Figure 2.3 at three stations highlighted by the pink diamonds in Figure 2.1. The dashed lines indicate sensitivity levels of real-time GNSS data.

of the displacement waveforms that could be used for quality verification for the static slip solution, notably in differences in the amplitude and timing of the PGD of the waveforms in each component. Underestimation of the PGD by the GNSS-only and vertical-only offshore slip models indicates larger slip offshore is required to match the observed waveforms. For example, the east component at station P367 shows a 5 cm difference between the PGD of the input model and the GNSS only slip model. The timing differences of the PGD is likely due to underestimation of along-strike rupture extent. Such comparisons of the first part of the waveform can be useful for determining if the static slip inversion underestimates the slip, and rapidly checking solution quality.

2.6 Conclusions

Offshore data near the Cascadia subduction zone improves maximum tsunami height predictions by >20% for a deep (>15 km) M_w8 megathrust earthquake assuming known fault geometry. For a shallow megathrust rupture, maximum tsunami height estimates are improved

by >2.5 m (>75%) when using strategically-placed offshore stations. An error of 2.5 m has significant consequences where the 1 m to 3 m wave height estimate determines whether an evacuation order is issued. Vertical-only offshore data (for example, derived from ocean-bottom pressure sensors) improves shallow slip estimates when combined with onshore data, but slip is consistently underestimated, which in turn underestimates the tsunami impact even with a dense offshore station configuration with 30-40 km station spacing. Offshore estimates of horizontal coseismic displacement improve retrieval of maximum slip, and fewer stations are required to compute a tsunami prediction with necessary accuracy sufficient for warning. Among the networks tested, an offshore station configuration with sites located parallel to the deformation front on the hanging wall satisfactorily recovers the along-strike rupture extent and the length of coastline that experienced high-amplitude tsunami waves. The onshore high-rate displacement waveforms from first motions to PGD can be used to check the quality of the static slip inversions.

2.7 Supporting Information

2.7.1 Introduction

This document contains supplementary text and figures that provide more detail on methods used in this paper, as well as information about what synthetic data is available in the online archive. Figure 2.S1 illustrates the need for selecting higher resolution bathymetry in the tsunami modeling. Text S2 describes a resolution analysis of the station configurations considered in this study. Figures 2.S2-2.S6 show the model resolution for the different station configurations. Figures 2.S7 and 2.S8 show example slip inversion results for all station configurations in addition to those shown in Figure 2.3 of the manuscript. Figure 2.S9 shows the average tsunami wave height estimates as a function of distance along the coastline for the corresponding slip inversion results. Figure 2.S10 shows the full analysis of the quality metrics for all station configurations in addition to those shown in Figure 2.4 of the manuscript. Text S3 summarizes the approach to

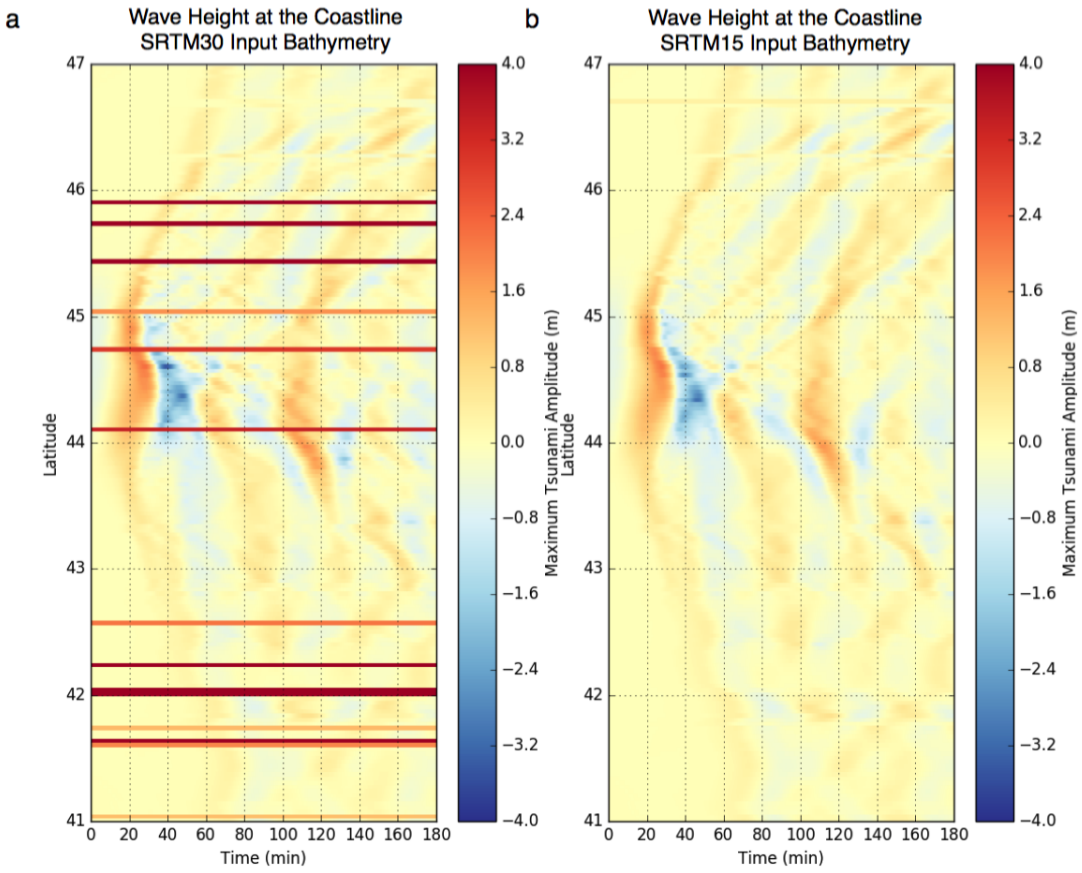

Figure S2.1: Tsunami wave height at the coastline for the deeper input rupture using **(a)** SRTM30 input bathymetry at 30 arc second resolution and **(b)** SRTM15 input bathymetry at 15 arc second resolution. The tsunami models using 30 arc second grid spacing produce some spurious points of constant wave height values. These errors are caused during the generation of the rougher bathymetry grid in the adaptive grid approach, where finer grid points are averaged to form one value in the rougher grid. The locations where the errors occur are points where the average height at the point is above the water level and does not experience inundation during the tsunami simulation. These errors do not occur when using 15 arc second resolution with no adaptive grid.

convert the static inversion solutions into kinematic forward rupture models. We also include a description about the synthetic displacements for each simulation available in the online archive.

2.7.2 Data and Model Resolution

The data and model resolution matrices can be computed through the singular value decomposition of the generalized inverse $\mathbf{G}^{-g}$, using the formulation of Menke (2012) as

$$\mathbf{G}^{-g} = [\mathbf{G}^T\mathbf{G}]^{-1}\mathbf{G}^T = \mathbf{V}_p\Delta_p^{-1}\mathbf{U}_p \tag{2.1}$$

The model resolution matrix $\mathbf{R}$ can be written as

$$\mathbf{R} = \mathbf{G}^{-g}\mathbf{G} = \mathbf{V}_p\mathbf{V}_p^T \tag{2.2}$$

The diagonal elements of $\mathbf{R}$ reflect how well the individual model parameters can be resolved given a particular data distribution. We compute $\mathbf{R}$ for the different station configurations examined in this study without including the regularization (smoothing) to examine the relative impact on resolution. These comparisons are shown in Figures 2.S2-2.S6.

When the regularization is included in the inversion scheme to prescribe a certain level of smoothness to the slip inversion estimate, the model resolution also depends on this smoothing:

$$\mathbf{R} = \mathbf{V}_S\mathbf{V}_p^T \tag{2.3}$$

where $\mathbf{V}_S$ is a combination of the matrix of eigenvectors $\mathbf{V}_p$, the smoothing parameters used in the regularization, and the west applied to the regularization. The value of the smoothing weight cannot be determined without knowing the data uncertainties as well as the signal-to-noise ratio of the data. Conducting inversions on a sample earthquakes allows us to objectively determine the appropriate weight to assign to the smoothing (regularization constraints) to fit the data within the expected uncertainties by minimizing the ABIC value (Akaike, 1998; Ide et al., 1996) using a range of smoothing weights. For example, while the expected idealized model resolution is slightly higher for the dense transect profiles (Figure S5) compared to the trench-parallel profile (Figure 2.S6), the trench-parallel profile configuration is able to consistently recover the along-strike slip extent and provide better tsunami wave height estimates for the shallow rupture.

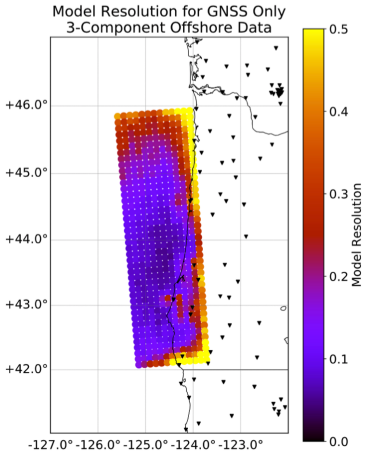

Figure S2.2: Value of the diagonal element of the resolution matrix for the fault model slip parameters for the GNSS-only network.

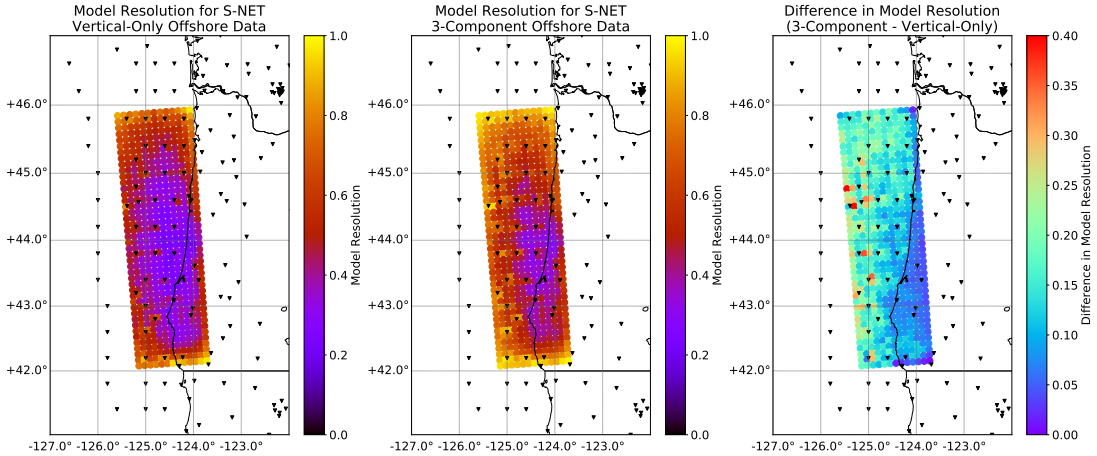

Figure S2.3: Value of the diagonal element of the resolution matrix for the S-Net configuration using (left) vertical-only offshore data and (middle) three-component offshore data. (right) For illustrative purposes we show the difference in model resolution when using three-component offshore data compared to vertical-only offshore data.

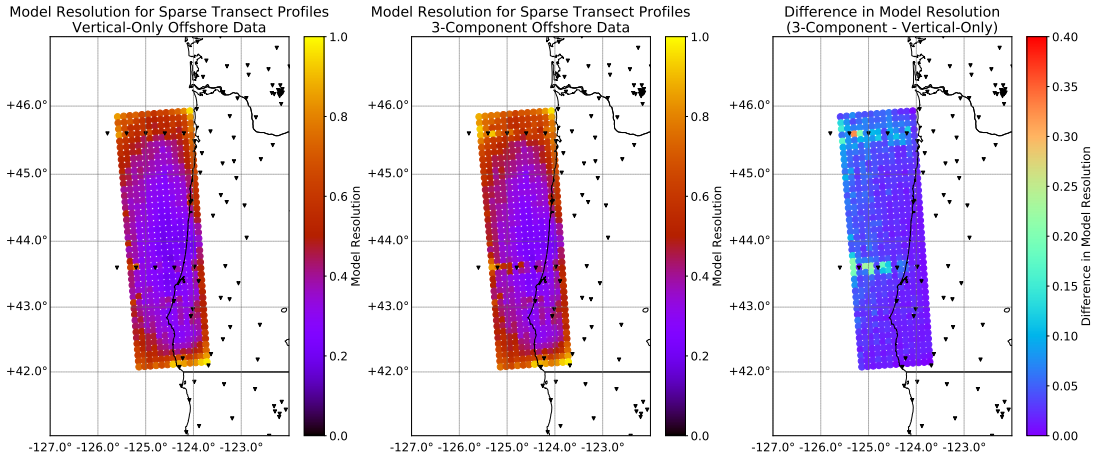

Figure S2.4: Fault model resolution for the Sparse Transect Profile configuration using (left) vertical-only offshore data and (middle) three-component offshore data. (right) Illustrative difference in model resolution when using three-component offshore data compared to vertical-only offshore data.

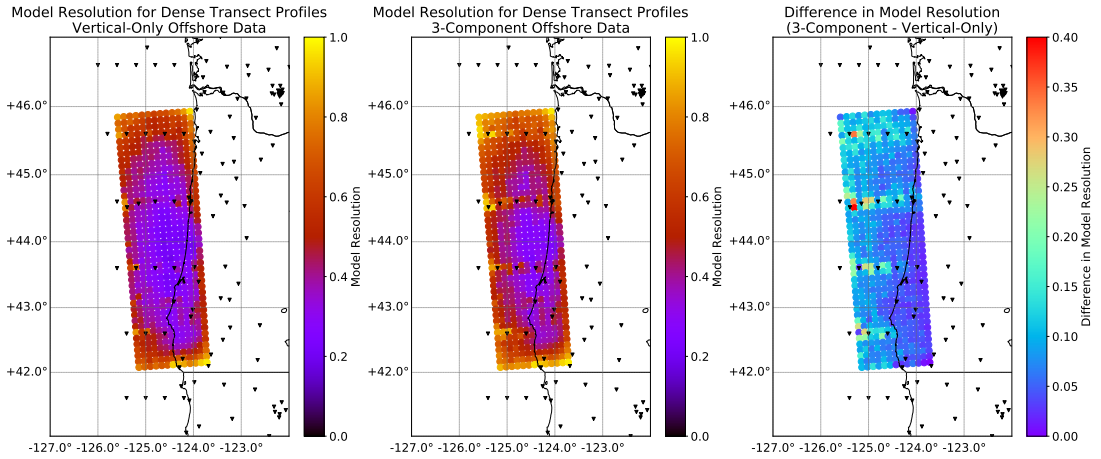

Figure S2.5: Value of the diagonal element of the resolution matrix for the Dense Transect Profile configuration using (left) vertical-only offshore data and (middle) three-component offshore data. (right) Illustrative difference in model resolution when using three-component offshore data compared to vertical-only offshore data.

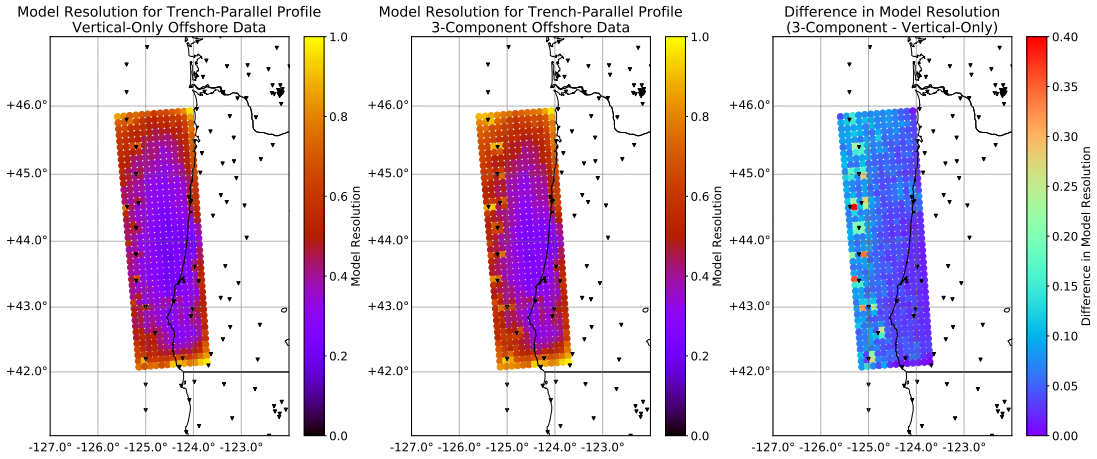

Figure S2.6: Value of the diagonal element of the resolution matrix for the Trench-Parallel Profile configuration using (left) vertical-only offshore data and (middle) three-component offshore data. (right) Illustrative difference in model resolution when using three-component offshore data compared to vertical-only offshore data.

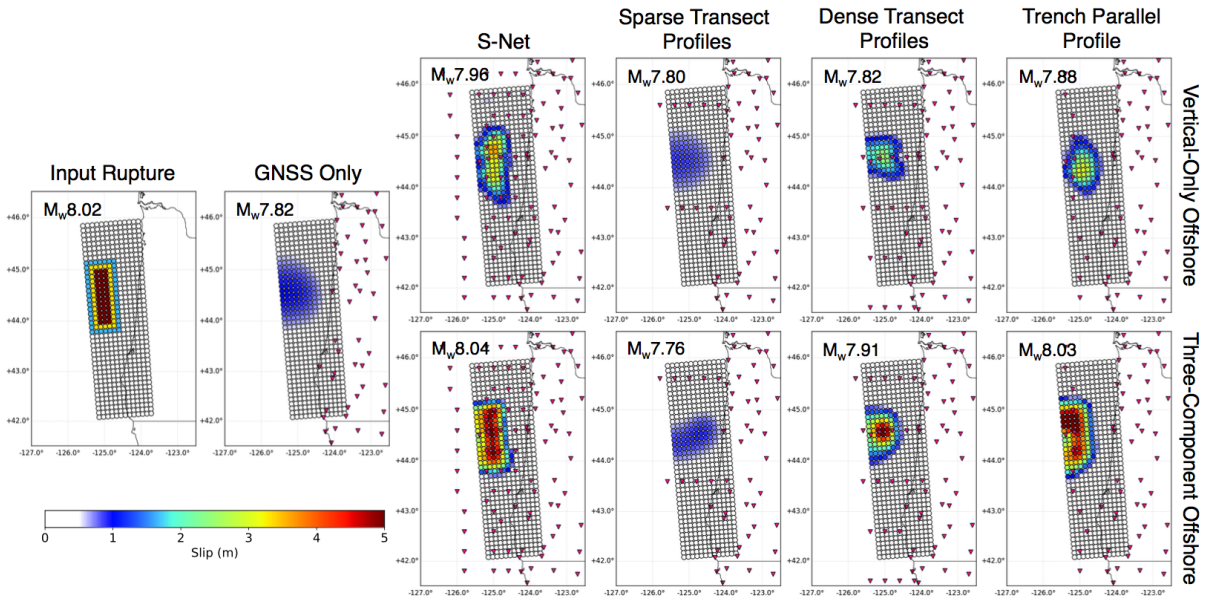

Figure S2.7: Example slip inversion results for the shallow rupture model for all inversions. The vertical-only offshore data results on the top row and three-component offshore data on the bottom row. One of the inversion results from the 15 realizations of random Gaussian noise is shown for each configuration, and results are similar for the other realizations.

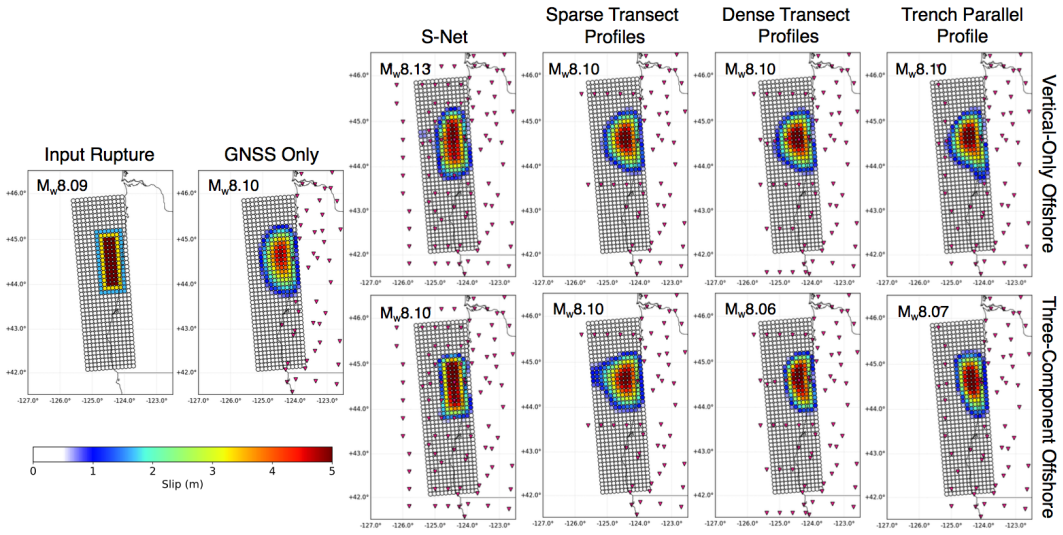

Figure S2.8: Example slip inversion results for the deeper rupture model for all inversions. The vertical-only offshore data results on the top row and three-component offshore data on the bottom row. One of the inversion results from the 15 realizations of random Gaussian noise is shown for each configuration, and results are similar for the other realizations.

2.7.3 Kinematic Forward Modeling

To examine how the high-rate displacement waveforms as measured onshore could be used to help verify the static slip inversion solutions, we examine the four ruptures shown in Figure 2.4 of the main text: the input model of shallow slip, the slip inversion results using GNSS only, and the two inversion results (vertical and three-component) with the trench parallel profile. We develop the static slip model into a kinematic rupture following the approach of Melgar et al. (2016) and Graves and Pitarka (2010). We assumed a Dreger-type slip rate function (Mena et al., 2010) that concentrates moment rate at the beginning of the slip window. The duration of slip at each subfault T_i scales with the depth d and the square root of slip at each subfault s_i as

$$T_i = \begin{cases} 2ks_i^{1/2} & d < 10 \text{ km} \\ ks_i^{1/2} & d > 15 \text{ km} \end{cases} \tag{2.4}$$

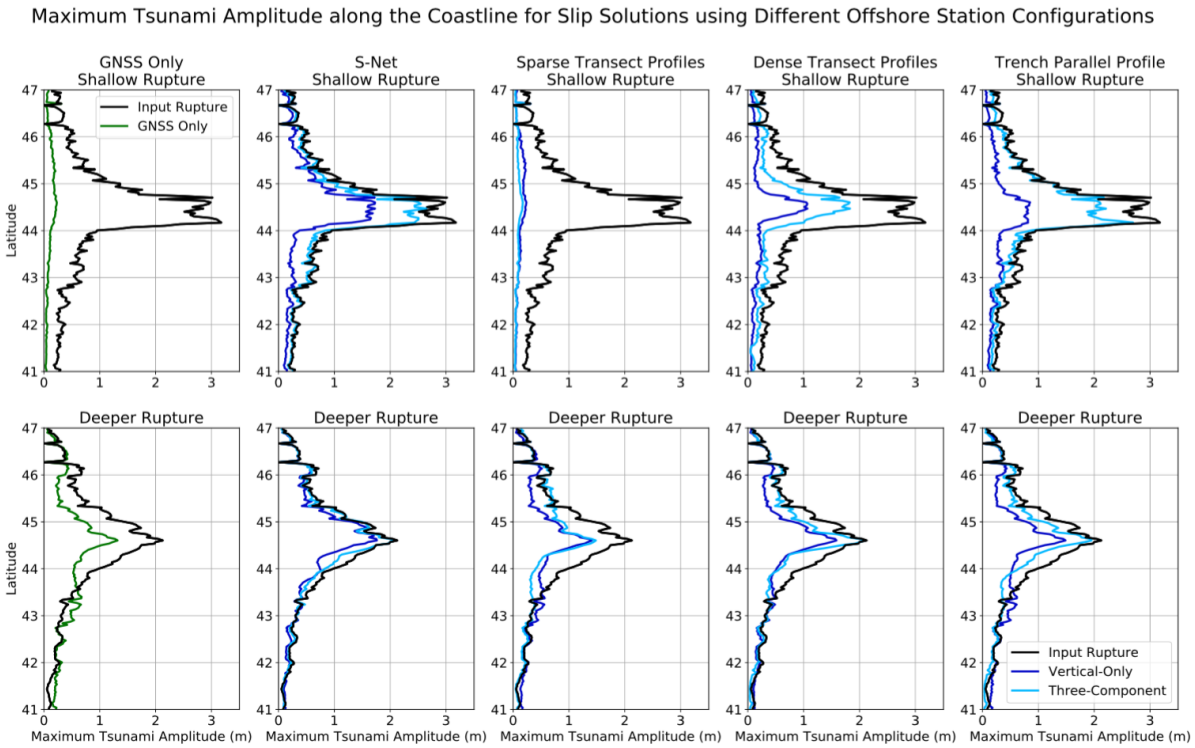

Figure S2.9: Maximum tsunami amplitude at the coastline. The maximum wave heights from the input rupture models are shown in black. Colored lines show the maximum wave heights from tsunami simulations computed from the slip inversion results averaged over all noise realizations.

where k is chosen such that the average slip duration over the rupture region corresponds to the empirical relationship in Somerville et al. (1999):

$$\langle T \rangle = 4.308 \times 10^{-7} \times M_0^{1/3} \tag{2.5}$$

where M_0 is the scalar moment in N-m. The rupture velocity, v_r, depends on the subfault depth:

$$v_r = \begin{cases} 0.56 \times v_s & d < 10 \text{ km} \\ 0.8 \times v_s & d > 15 \text{ km} \end{cases} \tag{2.6}$$

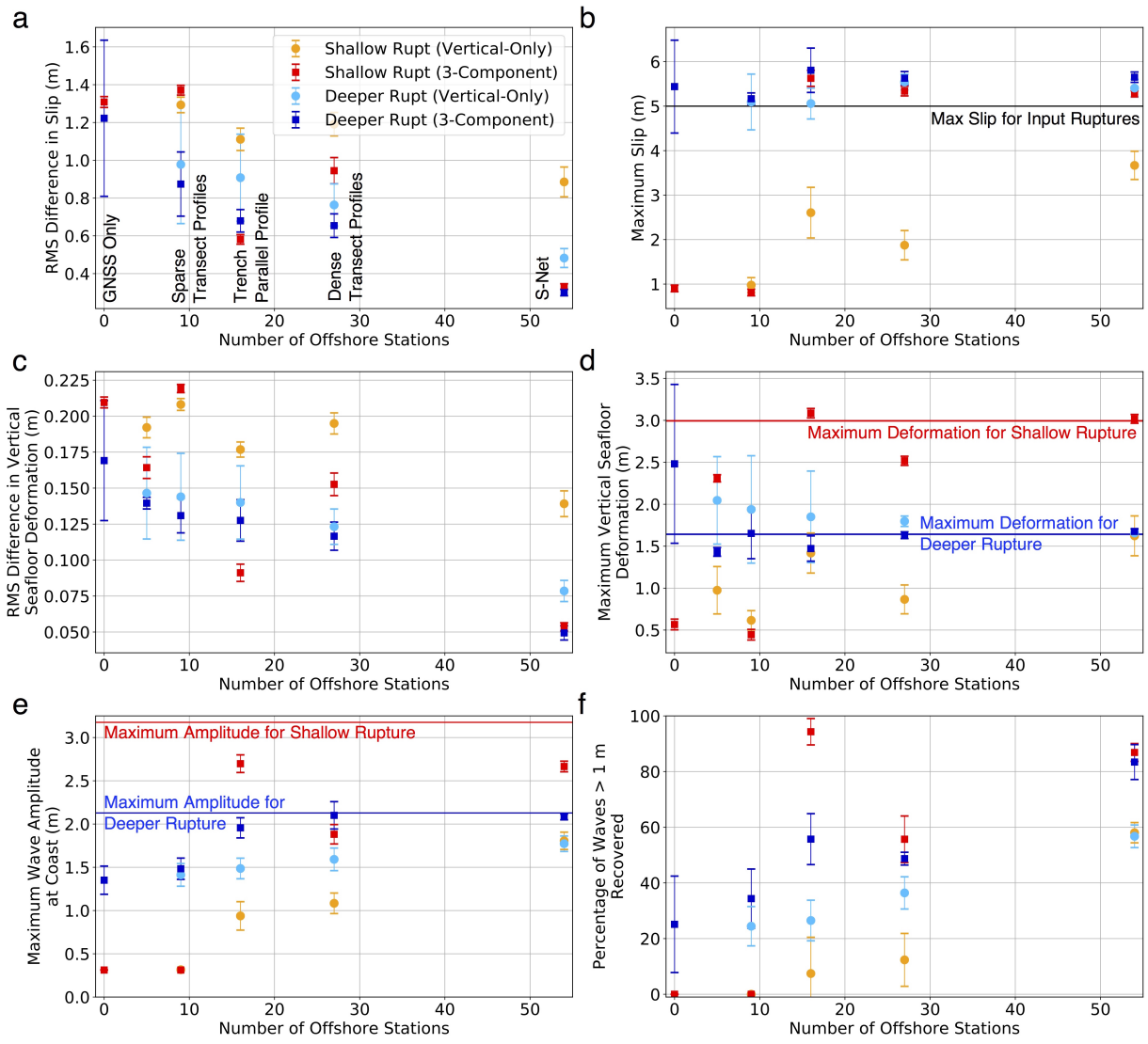

Figure S2.10: Compiled metrics comparing slip inversion results using the two types of offshore coseismic data (vertical-only in lighter colored circles and three-component in darker colored squares) for the shallow rupture (warm colors) and deeper rupture (cool colors). Subplots show the **(a)** rms difference in slip, **(b)** maximum slip, **(c)** rms difference in vertical seafloor deformation, **(d)** maximum seafloor deformation, **(e)** maximum wave amplitude at the coastline, and **(f)** percentage of high-amplitude waves >1 m at the coastline recovered in the tsunami estimates. All comparisons are plotted against the number of additional offshore stations in the networks used in the inversions. Error bars indicate the standard deviation of these values from all noise realizations.

where v_s is the shear wave speed in the velocity model. We compute 1 Hz displacement waveforms at GNSS stations near the rupture using the frequency-wavenumber approach of Zhu and Rivera (2002). Example waveforms at four stations are shown in Figure 2.5 of the main text.

2.8 Acknowledgements

This work is published in **Saunders, J.K., and Haase, J.S., 2018, "Augmenting onshore GNSS displacements with offshore observations to improve slip characterization for Cascadia subduction zone earthquakes,"** ***Geophysical Research Letters*****, 45(12), 6008-6017. https://doi.org/10.1029/2018GL078233**. The dissertation author was the primary investigator and author of this paper.

This work was funded by NASA grant NNX16AO32H through the NASA Earth and Space Science Fellowship. We thank Diego Melgar for assistance in the use of MudPY and the GeoClaw tsunami propagation software. We thank Junle Jiang for his helpful discussions and assistance regarding the tsunami modeling software. We thank Editor Gavin Hayes, Tim Melbourne and an anonymous reviewer for their constructive feedback and reviews. We appreciate the technical support from the IGPP Help Desk staff. We used the following software: fk code for computing the Green's functions (www.eas.slu.edu/People/LZhu/downloads/fk3.2.tar); MudPy slip inversion code (github/dmelgarm/MudPy); FakeQuakes kinematic forward modeling code (github/dmelgarm/FakeQuakes); and GeoClaw tsunami modeling software (geoclaw.org). Figures for this paper were made using Geodetic Mapping Tools and Python. Synthetic data used in this work can be found at http://agsweb.ucsd.edu/seismogps/cascadia/.

Chapter 3

Kinematic inversions for distinguishing shallow megathrust slip for tsunami early warning

3.1 Abstract

Rheological differences along the subduction interface are proposed to cause differences in the rupture characteristics of tsunamigenic megathrust earthquakes. Earthquakes that occur in the shallowest portion of the subduction zone are called "tsunami earthquakes" because they produce disproportionally large tsunamis for their seismically-derived magnitude. Tsunami earthquakes are generally depleted in high-frequency shaking compared to typical megathrust earthquakes, which makes it particularly difficult for coastal populations near the earthquake to know to self-evacuate to higher ground. Near-source tsunami early warning systems that rapidly estimate the earthquake slip location and amount could provide further information for expert opinion to determine whether the event is a shallow tsunami earthquake and that initial warnings need to be elevated.

The depth-dependent changes in rupture characteristics of megathrust earthquakes can lead to differences in the early portion of the displacement waveforms, particularly evident from the P-wave onset to peak ground displacement. We explore what key conclusions can be drawn from rapid kinematic slip inversions. We test an approach to assess confidence in the slip solution by applying additional depth-dependent spatial constraints in kinematic slip inversions using the early portion of these waveforms. We use a suite of synthetic kinematic rupture models of M_w ~8 Cascadia earthquakes located along different depths of the subduction interface as the input to the slip inversions. We examine how the depth-dependent inversion constraints and different data types affect the recovered estimates of maximum slip as well as the rupture extent in both the along-dip and along-strike directions. Estimating the along-dip rupture extent will help with categorizing the earthquake as a shallow tsunami earthquake or not, while knowing the along-strike rupture extent is vital for determining the region of coastline that will require evacuation from high-amplitude tsunami waves. We also test the improvement in resolving rupture parameters by combining multiple data types: onshore high-rate GPS displacements, onshore velocities derived from strong-motion accelerometers, and future measurements from offshore seafloor sensors which could be made available in real time using fiber optic cable networks.

3.2 Introduction

Coastal populations in subduction zone environments live with dual risks of widespread damage from strong shaking by subduction zone earthquakes and from the tsunamis resulting from these earthquakes. The size of the tsunami depends on the extent of seafloor that is displaced during the earthquake, where generally larger subduction earthquakes lead to greater seafloor displacements and larger tsunamis. However, the amount of seafloor displacement also depends on the source mechanism, the distribution of slip with depth, and the depth-dependent rheological

properties along the subduction interface.

Subduction zone earthquakes typically nucleate and rupture in the central portion of the megathrust, around 15-50 km depth (Lay et al., 2012). The shallowest portion of the megathrust, from the trench to about 15 km depth, generally has lower rigidity and high pore pressures associated with subducted sediments and the presence of fluids along the subduction interface can enable aseismic, stable slip (e.g., Byrne et al., 1988; Hyndman et al., 1997; Moore & Saffer, 2001; Wang & Hu 2006). This region is typically considered to have velocity-strengthening frictional properties which can inhibit rupture propagation near the trench (e.g., Hu & Wang, 2008; Saffer & Tobin, 2011). However, earthquakes have been observed to rupture exclusively the shallowest portion of the subduction interface.

Slip inversion and back projection studies of these shallow subduction earthquakes compared to typical subduction zone earthquakes show that shallow ruptures tend to be depleted in high-frequency energy, have slower rupture velocities with longer slip durations, and produce large amounts of slip on the fault (e.g., Kanamori, 1972; Kanamori & Kikuchi, 1993; Lay & Bilek, 2007; Newman et al., 2011). Due to the large amount of fault slip near the trench, these shallow earthquakes produce anomalously large tsunamis compared to their seismically-derived magnitudes, and as such, have been given the name "tsunami earthquakes" (Kanamori, 1972; Polet & Kanamori, 2000). Two recent tsunami earthquakes, the 2006 M_w7.8 Java and the 2010 M_w7.8 Mentawai, Indonesia, tsunami earthquakes, produced disproportionately large tsunamis with maximum local run-ups of 14 and 9 m, respectively, and resulted in hundreds of fatalities (Ammon et al., 2006; Lay et al., 2011). Witnesses of the 2010 Mentawai tsunami earthquake described the shaking to have a gentle rocking motion that lasted for several minutes (Hill et al., 2012). While this is characteristic for tsunami earthquakes, this was significantly different from the strong high-frequency shaking felt by residents during the recent tsunamigenic 2007 M_w8.4 Bengkulu, Indonesia, earthquake in the same region (Lay et al., 2011). While some residents evacuated after the earthquake, many did not realize that the earthquake was strong enough to

generate a tsunami and did not begin evacuation until they heard the tsunami (Fritz et al., 2011). Near-source tsunami early warning systems could help alert people of these events and aid in evacuation efforts.

The National Oceanic and Atmospheric Administration (NOAA) operates an international tsunami early warning system (Synolakis & Bernard, 2006). These tsunami warning centers use the hypocenter and magnitude calculated from teleseismic waves and w-phase inversions to issue initial tsunami warnings and watches (Hayes et al., 2011; Hirshorn et al., 2013). These warnings are then updated upon direct observation of the tsunami waves at DART buoys, which are deep ocean pressure gauges attached to buoys for real-time telemetry (Titov et al., 2005). While these observations can provide accurate early warnings to coastal populations in the far field ($>$1000 km) from the tsunami source (Titov et al., 2005), this approach is not feasible for near-source warnings because the tsunami often reaches the closest DART buoys at around the same time it arrives at the nearest coastline.

Japan has the longest-operating near-source tsunami early warning system, with the first instrumental system established in Sendai in 1941 (Shuto & Fujima, 2009; Bernard & Titov, 2015). The system is operated by the Japanese Meteorological Agency (JMA), and tsunami warnings are issued based on the pre-computed earthquake scenario that most closely matches the rapid magnitude and hypocenter calculations from onshore seismic data (Uchiike & Hosono, 1995; Tatehata, 1997; Hoshiba & Ozaki, 2014). However, traditional magnitude estimation techniques from near-field seismic sensors suffer from saturation (Brown et al., 2011), and the magnitude can be grossly underestimated for large earthquakes. This is unfortunately what occurred during the 2011 M_w9.0 Tohoku-oki earthquake and tsunami, where initial magnitude estimates used in early warnings did not rise above M_w8 (Hayes et al., 2011; Hoshiba & Ozaki, 2014).

The resulting underestimation of the amplitude of the 2011 Tohoku-oki tsunami prompted a re-evaluation of the Japanese near-source tsunami early warning system (Tsushima & Ohta, 2014). To prevent underestimations of future tsunamis, dense cabled arrays of offshore seafloor

pressure sensors, the S-net and DONET arrays, were installed in the Japan and Nankai subduction zones (Kawaguchi et al., 2008; Uehira et al., 2012). These instruments provide direct near-field observations of the tsunami before it arrives at the coastline, and early warning methods are being developed that use the near-field tsunami amplitudes for scenario-matching and rapid tsunami simulations (e.g., Tsushima et al. 2009, 2012; Tanioka, 2018; Yang et al., 2019). However, seafloor pressure observations in the near field during an earthquake contain a complicated mix of signals: the seismic waveforms contain acoustic reverberations in the water column as well as the acceleration of the instrument; and the coseismic offset and tsunami signal are of opposite sign, so these signals obscure each other until the tsunami propagates away from the rupture region (Saito & Tsushima, 2016). Additionally, the high cost of installation, maintenance, and operations for a dense cabled seafloor network can be prohibitive for many countries.

A complimentary approach to improve near-source tsunami early warning, particularly in regions without dense offshore arrays, is to provide detailed information about the earthquake source as rapidly as possible using near-field observations from strong-motion accelerometers and Global Navigation Satellite Systems (GNSS) sensors. Finite fault slip inversions use information about the coseismic offset and ground motion measured on the surface to calculate how the fault moved during the earthquake. These methods provide information on the location and amount of slip, which can then be used in both scenario-matching approaches and rapid tsunami simulations. Several algorithms that use real-time estimations of the coseismic displacement from high-rate GNSS observations to invert for the total fault slip have been developed for earthquake early warning applications, where the objective is to issue alerts of strong ground motion before the seismic waves arrive (Grapenthin et al., 2014; Minson et al., 2014; Crowell et al., 2016). Simulated real-time demonstrations of these algorithms have shown that they provide improved early warnings of strong ground motion for large M_w7.5+ earthquakes (Ruhl et al., 2017; Crowell et al., 2018).

The largest subduction zone earthquakes ($M_w \sim$9) tend to have large rupture regions

accompanied by large coseismic offsets which are easily distinguishable in GNSS observations. Smaller tsunamigenic earthquakes of M_w ~8 tend to produce smaller coseismic displacements which may be difficult to distinguish above the GNSS noise level depending on the rupture location in relation to the coast (Saunders & Haase, 2018).The along-strike location of a M_w ~8 rupture influences the region of coastline impacted by high-amplitude waves, while the along-dip rupture location determines whether the earthquake is a shallow tsunami earthquake that generates amplified tsunami waves. As demonstrated in Saunders and Haase (2018) with synthetic rupture scenarios, static slip inversions using onshore-only coseismic data have difficulty resolving slip accurately in the case of shallow tsunami earthquakes because of the small coseismic offset onshore where the GNSS instruments are located. While offshore vertical coseismic data from seafloor pressure sensors improve static slip estimates of tsunami earthquakes compared to onshore-only solutions, these data are not sufficient to obtain slip inversion solutions that correctly predict the along-strike extent of the rupture. Adding offshore horizontal coseismic data that might be derived in the future from GNSS-Acoustic sensors results in slip solutions that accurately estimate the coastal extent of high-amplitude tsunami waves, but such observations are currently not feasible to obtain in real time.

For our analysis, we use a suite of synthetic kinematic rupture models developed for the Cascadia subduction zone for evaluating early warning algorithms (Melgar et al., 2016). The Cascadia subduction zone, while currently seismically quiescent, is capable of large tsunamigenic earthquakes, with the last major earthquake occurring in 1700 AD (Satake et al., 2003). Turbidite records gathered along the Pacific Northwest coastline suggest a paleoseismic record of earthquakes ranging between ~M_w8-9 (e.g., Atwater et al., 1995; Goldfinger et al., 2003, 2012; Nelson et al., 2006). As it is unclear whether the Cascadia subduction interface is locked to the trench (Schmalzle et al., 2014; Pollitz & Evans, 2017; Li et al., 2018), it would be useful for near-source tsunami early warning tsunami early warning systems for this region to be able to identify if an earthquake that occurs is a shallow tsunami earthquake.

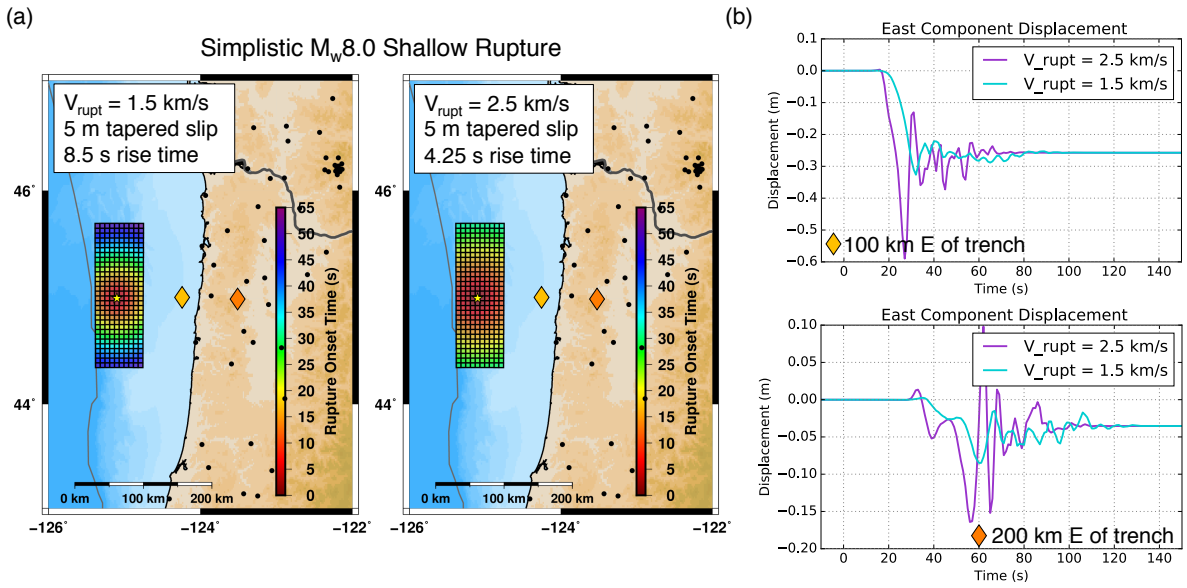

Figure 3.1: Comparison of synthetic displacement waveforms from two M_w8 kinematic ruptures with different rupture velocities and slip durations. **(a)** The two kinematic rupture models, colored by the rupture onset time. Both rupture scenarios have 5 m uniform slip with linear slip taper around the rupture edges. The yellow star indicates the location of the hypocenter, and the two diamonds are the station locations where synthetic displacement waveforms are computed. **(b)** Comparison of synthetic displacement waveforms in the east component for the two rupture models at distances of 100 km and 200 km from the trench. While both ruptures produce the same coseismic offsets, the displacements from the slower rupture (blue lines) have smaller amplitude and later peak ground displacement timing compared to the faster rupture (purple lines).

Utilizing high-rate GNSS displacement waveforms in the inversion scheme can provide additional rupture information about the timing of and location of slip that could improve slip solutions. Forward simulations show that low rupture velocities that might be expected in shallow tsunami earthquakes provides significantly different time series in the early portion of near-field displacement waveforms (Figure 3.1). Figure 3.1 shows two M_w8 rupture models with the same static slip distribution, where the rupture velocities are 1.5 km/s and 2.5 km/s, which covers the range of expected values that might be observed for shallow tsunami earthquakes and typical megathrust earthquakes, respectively (Lay et al., 2012). The slower rupture model also has longer local slip duration like in a tsunami earthquake, and produces shaking with smaller amplitude and

Table 3.1: List of data fit criteria for the slip inversion results using different depth constraints in order to confirm the location of slip. Our goal is to be able to determine the possibility of shallow slip in the case of a megathrust earthquake because that will determine whether the tsunami alert issued based on the earthquake magnitude needs to be amplified.

Rupture Location	**No Depth Constraint**	**Shallow Constraint**	**Deep Constraint**	**Can we rule out the possibility of shallow slip?**
Shallow	Good	Good	Poor	No, shallow slip confirmed
Deep	Good	Poor	Good	Yes, shallow slip ruled out
Both	Good	Good	Good	No, inconclusive

a delay in the arrival of the peak ground displacement (PGD).

We explore whether applying additional down-dip spatial constraints in the kinematic slip inversions using the early portion of GNSS displacement waveforms (P-wave to PGD) can be used to rapidly determine whether shallow slip has occurred. We set this up as an inverse problem where we test the hypothesis that there exists a slip model constrained to be shallower than 12 km that fits the GNSS displacement data to the level of the errors. If this fails, this information can be rapidly considered in the warning decisions to indicate low probability that it is an anomalous tsunami earthquake. Table 3.1 summarizes our hypothesis testing scheme for the set of experiments. We test the improvement in resolving rupture parameters by combining onshore displacement waveforms with velocities derived from seismogeodetic combination of GNSS data with collocated strong-motion accelerometers (e.g. Bock et al., 2011; Saunders et al., 2016). We also test the improvement in slip inversion solutions when including offshore velocity waveforms obtained from hypothetical strong-motion accelerometers on the seafloor.

3.3 Methods

3.3.1 Kinematic Rupture Scenarios

To test our ability to retrieve accurate slip models, we use as truth synthetic waveform data from a suite of 43 $\sim M_w 8$ kinematic rupture models of the Cascadia subduction zone (Melgar

et al., 2016). These rupture models vary in slip location and amount, and allow us to robustly assess our inversion approach. Figure 3.2 shows the hypocenter locations of the scenarios used in our analysis. We use the 64 high-rate GNSS station locations in Melgar et al. (2016). These are a subset of the many GNSS stations operated by the Plate Boundary Observatory (Herring et al., 2016) and Pacific Northwest Geodetic Array (Popovici et al., 2015) that provide 1 Hz positions in the Cascadia region in real time. The offshore station locations correspond to the locations of seafloor pressure sensors in the OOI and NEPTUNE cabled arrays (Kelley et al., 2014), three GPS-Acoustic campaign stations (Chadwell et al., 2018), and a hypothetical trench-parallel profile of stations (Saunders & Haase, 2018). The following is a brief summary of the rupture generation process, described in detail in Melgar et al. (2016).

A target magnitude is provided, and empirical magnitude scaling relations (Blaser et al., 2010) set the rupture dimensions. The rupture region is placed randomly on the subduction interface, in this case a $\sim$10 km discretized finite element model of the Cascadia subduction zone (McCrory et al., 2012). A slip distribution following a von Karman correlation function is generated and the hypocenter is randomly chosen within the rupture region. The von Karman correlation function was empirically determined to be a good description for slip distribution behavior through analysis of slip inversion solutions of real earthquakes (Mai & Beroza, 2002). In the Melgar et al. (2016) scenario catalog, the ruptures are specified to have purely dip-slip motion.

Following the procedure of Graves and Pitarka (2010) and modified for subduction zone environments, the background rupture velocity varies with depth and the local shear wave velocity v_s as

$$v_r = \begin{cases} 0.56 \times v_s & \text{d } < 10 \text{ km} \\ 0.8 \times v_s & \text{d } > 15 \text{ km} \end{cases} \tag{3.1}$$

where there is a linear increase in rupture velocity between these depth values. The rupture velocity is then perturbed slightly such that the portions of the fault with large slip rupture faster.

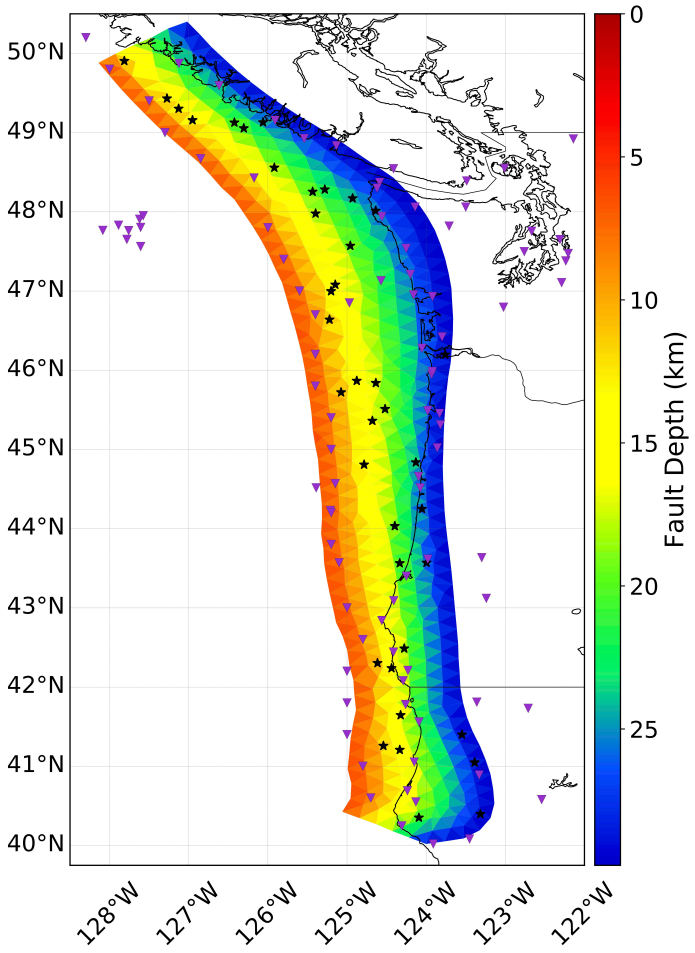

Figure 3.2: Map of hypocenter locations of the rupture scenarios used in the inversion analysis (black stars). The fault model used for both the rupture scenarios and the slip inversions is also shown, colored by the depth. Station locations are indicated by the purple triangles.

The source time function (STF) has a Dreger-type functional form (Mena et al., 2010), where the local rise time, T_i, varies with depth, seismic moment, and slip as

$$T_i = \begin{cases} 2ks_i^{1/2} & \text{d} < 10 \text{ km} \\ ks_i^{1/2} & \text{d} > 15 \text{ km} \end{cases} \tag{3.2}$$

The variable k is set such that the average rise time follows the empirical scaling relationship

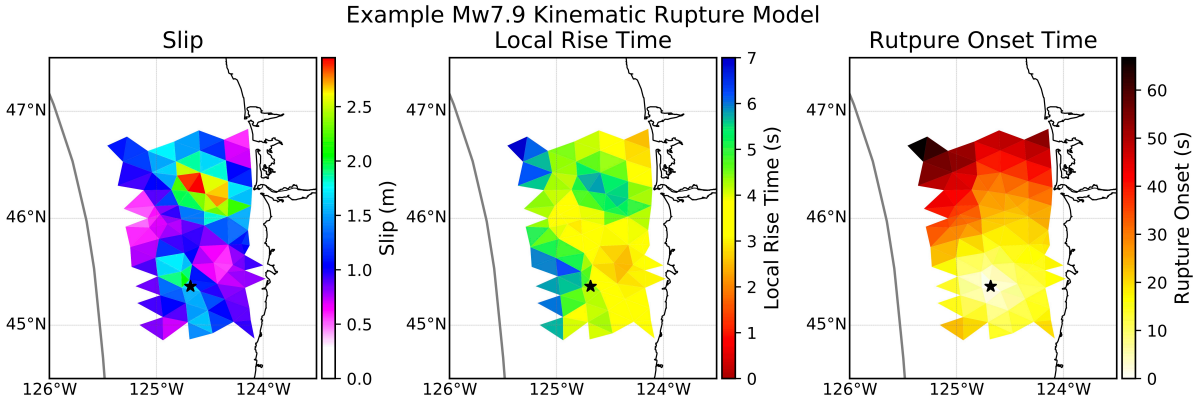

Figure 3.3: Example rupture scenario that illustrates the depth- and slip-dependent characteristics imposed on the timing of the rupture. The black star indicates the hypocenter of the rupture.

described in Somerville et al. (1999):

$$\langle T_i \rangle = 4.308 \times 10^{-7} M_0^{1/3} \tag{3.3}$$

where the moment, M_0, is in units of N-m. Figure 3.3 shows an example rupture scenario that illustrates the depth- and slip-dependent characteristics imposed on the timing of the rupture.

Melgar et al. (2016) also provide 1 Hz displacement waveforms for these scenario earthquakes at the 64 real-time GNSS station locations. We expand this synthetic dataset to include collocated velocities at all of these GNSS stations as well as offshore velocity waveforms at the offshore stations in Figure 3.2. We use the same velocity model (Gregor et al., 2002) and frequency-wavenumber method for computing Green's functions (Zhu & Rivera, 2002) as Melgar et al. (2016) to forward compute additional synthetic velocity waveforms at these stations for the rupture scenarios we consider in our slip inversion analysis. Noise is then added to these synthetic data before performing slip inversions.

3.3.2 Inverse Problem Setup

We follow the linear least squares approach of Hartzell and Heaton (1983) to set up the slip inversions. In this method, a prescribed fault surface is discretized into L subfaults. Following the notation of Ide et al. (1996), the jth component of displacement, u, at location x and time t can be expressed as the time evolution of slip on each subfault summed over the fault:

$$u_j(x,t) = \sum_{i,k,l} \int g_{ijl}(x,t;\tau) a_{ikl} \phi_k(\tau) \mathrm{d}\tau \tag{3.4}$$

where $g_{ijk}(x,t;\tau)$ is the Green's function representing the jth component of displacement at (x,t) when an impulsive source in the ith slip direction occurs on the lth subfault at time $t = \tau$. The form of the source time function for the ith slip component on the lth subfault in the kth time window is expressed by $\phi_k(\tau)$, and a_{ikl} is the amplitude of that source time function. This problem can be linearized by prescribing a form for the source time function ϕ and specifying a rupture velocity or range of rupture velocities (Trifunac, 1974). After these are specified, the only unknowns that remain are values of a_{ikl}. The problem can now be represented in the form of the matrix equation

$$d \cong Gm \tag{3.5}$$

where m is the model vector composed of the a_{ikl} values for each slip direction component on each subfault, G is the matrix of Green's functions convolved with the specified source time function, $\int g_{ijk}(x,t;\tau)\phi(\tau)\mathrm{d}\tau$, and d is the data vector of waveforms in each component at each station.

This equation can be solved using a linear least squares approach, but the solution is unstable because G is an ill-conditioned matrix. We stabilize the solution by including smoothing constraints in the inversion:

$$\begin{pmatrix} G \\ \lambda_s L_s \\ \lambda_t L_t \end{pmatrix} m \cong \begin{pmatrix} d \\ 0 \\ 0 \end{pmatrix} \tag{3.6}$$

where L_s and L_t are spatial and temporal regularization matrices, respectively, and λ_s and λ_t are the corresponding scalar weights. The values of the weights determine how much the inversion prioritizes fitting the model to the data compared to satisfying the smoothing constraints. For our slip inversions, we choose the spatial regularization matrix L_s to be an identity matrix. We perform slip inversions using a range of λ_s values, where the preferred weight is chosen by selecting the inversion solution that minimizes the Akaike's Bayesian Information Criterion (Akaike 1998; Ide et al., 1996). The slip vectors are also rotated 45° in the inversion to allow us to constrain the slip to the positive dip-slip direction using a nonnegative least squares approach.

In our slip inversions, we use the same discretized model of the Cascadia subduction zone as well as the same 1D velocity model as Melgar et al. (2016). We use the same frequency-wavenumber approach to compute the Green's functions (Zhu & Rivera, 2002), and we specify a Dreger-type source time function (Mena et al., 2010). While such assumptions are idealistic because they match the methods used to create the synthetic data used in the slip inversions, these choices will allow us to better determine the maximum potential benefit of our proposed approach to distinguish megathrust slip location.

For each rupture scenario we only use data from stations that reach PGD within 90 s of the earthquake origin time. We use the early portions of these waveforms in the slip inversions: up to 5 s before the P-wave onset and 5 s after the PGD. We perform slip inversions using the open-source MudPy inversion code (Melgar & Bock, 2015). We test three cases of depth-dependent regularizations:

1. No additional constraint

2. Constrain slip to be shallow (< 12 km)

3. Constrain slip to be deep ($>$ 12 km).

We use the data misfit as a criterion to examine whether the hypothesis that the slip is shallow or deep as implemented with the constraint can be proven to be true or false (Table 3.1).

Typically in linearized kinematic slip inversions, uncertainties in the time history of slip are taken into account using the multi-time window approach (Ide et al., 1996). In that method, slip can occur over multiple overlapping time intervals, where the source time function often takes the form of a triangle function. This allows for variations in local rupture velocity and slip duration, and can lead to the reconstruction of complicated source time functions. For the problem that we are considering, we are most interested in the slip amount and location on the fault. To make our kinematic slip inversions more tractable for early warning applications, we impose assumptions on the rupture kinematics to reduce the size of the inversion to one time window and remove the need for temporal regularizations L_t. We assume that the earthquake's hypocenter, origin time, and magnitude are available before the inversion process begins, as these are parameters that will be computed by earthquake early warning algorithms (Allen et al., 2009). We specify a Dreger-type STF where the local rise time depends on the PGD magnitude as calculated using updated PGD-magnitude scaling relations from Ruhl et al. (2018):

$$\log(\text{PGD}) = A + B \times M_w + C \times M_w \times \log(R) \tag{3.7}$$

where PGD is in meters, R is the hypocentral distance in kilometers, and A, B, and C are regression coefficients with values -5.919, 1.009, and -0.145, respectively. We set a rupture velocity equal to the background v_r defined in Equation 3.1, and compute the start time of slip at each subfault using the hypocenter estimate and distance to the subfault.

For each rupture, we perform slip inversions using the three spatial constraints and using the following data type combinations:

1. Onshore GNSS displacements only

2. Onshore velocities only

3. Onshore GNSS displacements and collocated velocities

4. Onshore GNSS displacements and collocated velocities, and offshore velocities

We examine if there is a particular combination of data types that best discriminates between shallow and deep slip using our hypothesis testing scheme. We also assess how well the preferred slip inversions solve for the maximum slip and rupture area, metrics that are necessary for accurately determining the near-shore tsunami impact (Saunders & Haase, 2018).

3.4 Results

Figure 3.4 shows slip inversion solution results using the three depth constraints for an example shallow rupture with GNSS displacements as the input data. Examining the slip solutions, we observe that the shallow slip constraint produces a similar rupture pattern in the shallow portion as the slip inversion with no depth constraint, but the shallow constraint inversion does not have the downdip slip smearing effects shown in the no depth constraint case. The deep constraint inversion solution has lower overall slip and slip is placed along the upper edge of the depth limits in the inversion constraint. When comparing the displacement waveforms for these inversion solutions (Figure 3.5), we observe that displacement is underestimated for stations with large slip in the deep constraint solution, as expected for this shallow rupture. However, most waveforms show very similar-amplitude waveforms for the three inversion cases. When we compare the inversion results for another example shallow rupture that is located further from the coast (Figures 3.6 and 3.7), we see that with all three slip constraints, slip is underestimated on the fault, and do not produce significantly different waveforms.

Figures 3.8 and 3.9 show slip solutions and displacement waveform comparisons for an example deep rupture with GNSS displacements as the input data. We observe that the shallow

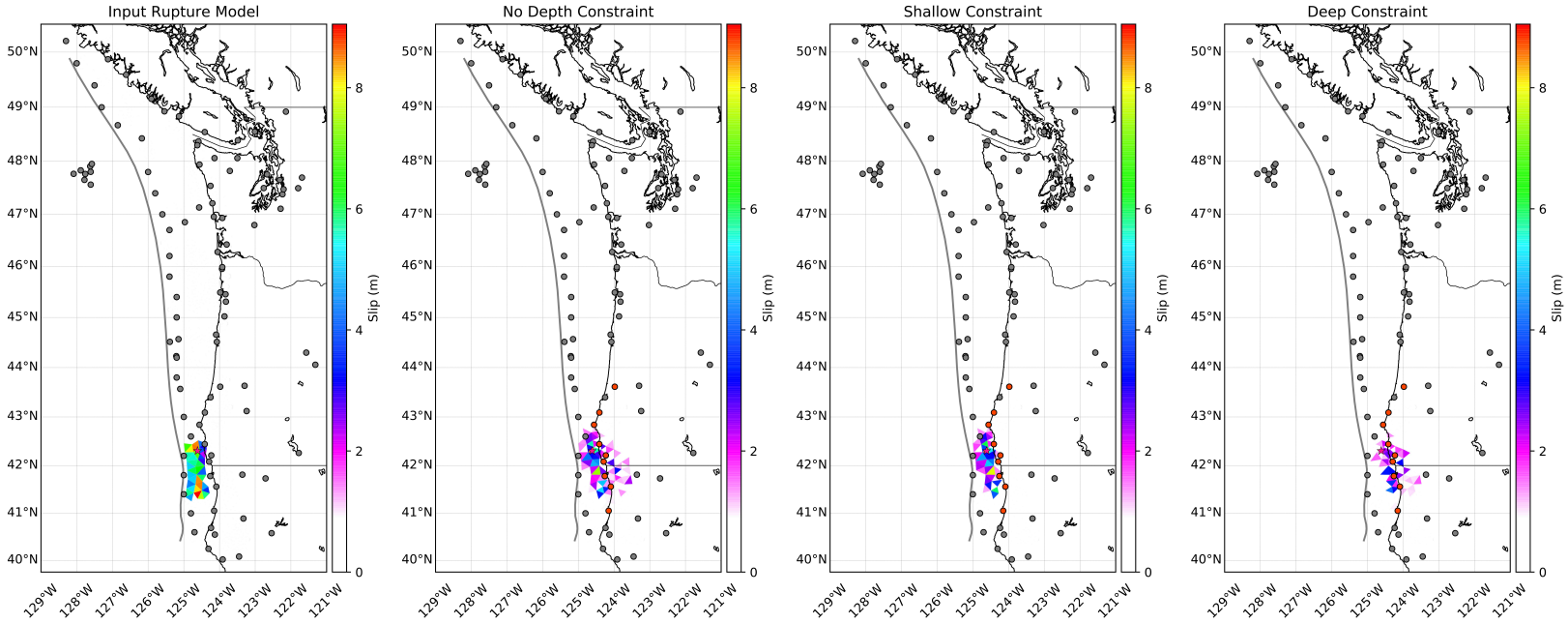

Figure 3.4: Slip solution comparisons using different depth constraints for an example shallow rupture, where the input rupture model is shown on the left. The slip inversions were performed using GNSS displacements only, where the stations used in the inversions are highlighted by the orange circles. The location of the trench is shown by the gray line and the hypocenter of the rupture scenario is shown by the star.

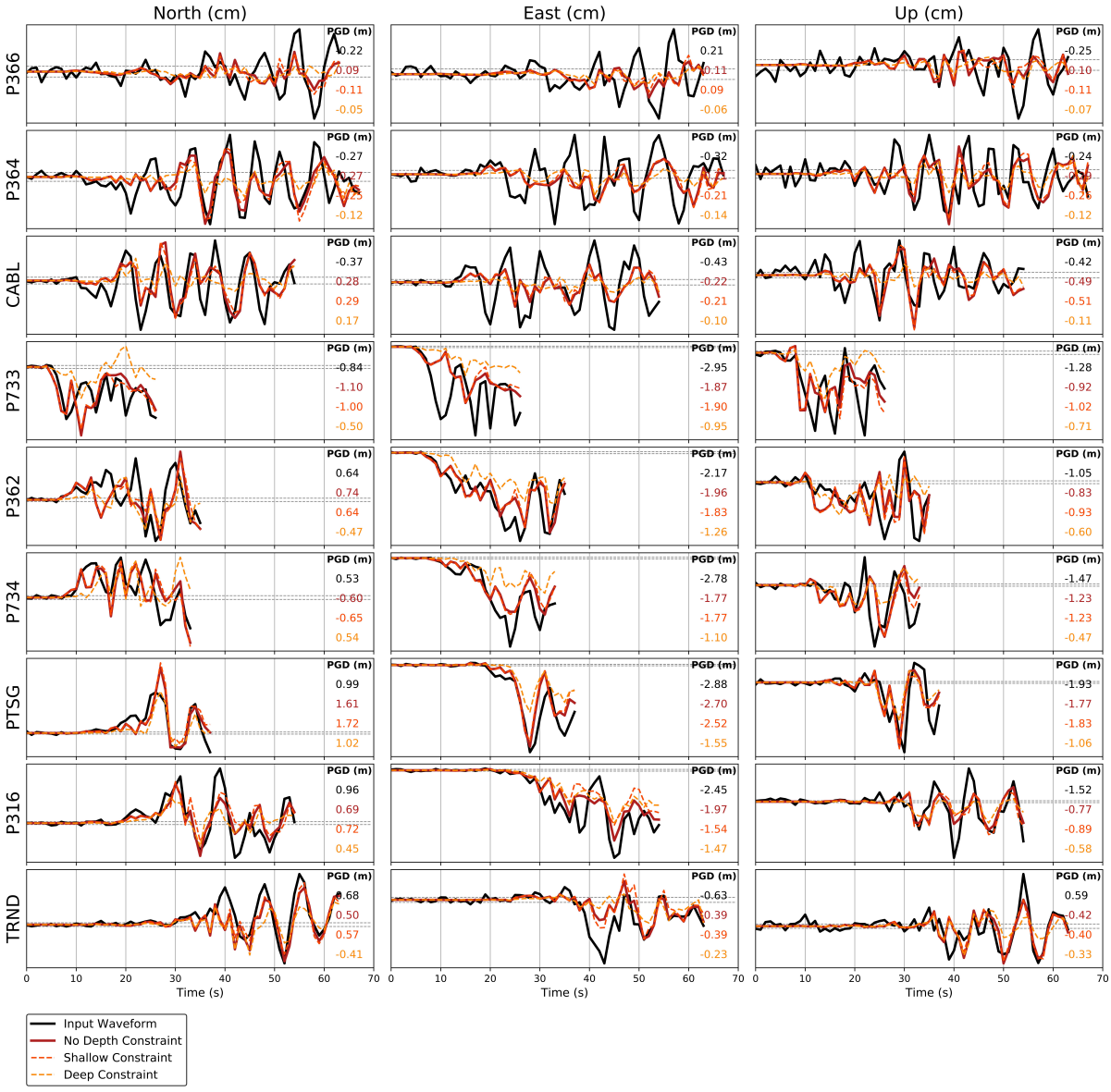

Figure 3.5: Displacement waveform comparisons of the slip inversion solutions for the same example shallow rupture shown in Figure 3.4. The input waveforms are shown in black, while the colored lines show the synthetics reproduced from inversion solutions with different depth constraints. The dashed gray lines show the expected sensitivity of GNSS displacement data at 2.5 cm in the horizontal components and 5 cm in the vertical component. The waveforms are plotted relative to the earthquake origin time, and the stations are arranged from north to south.

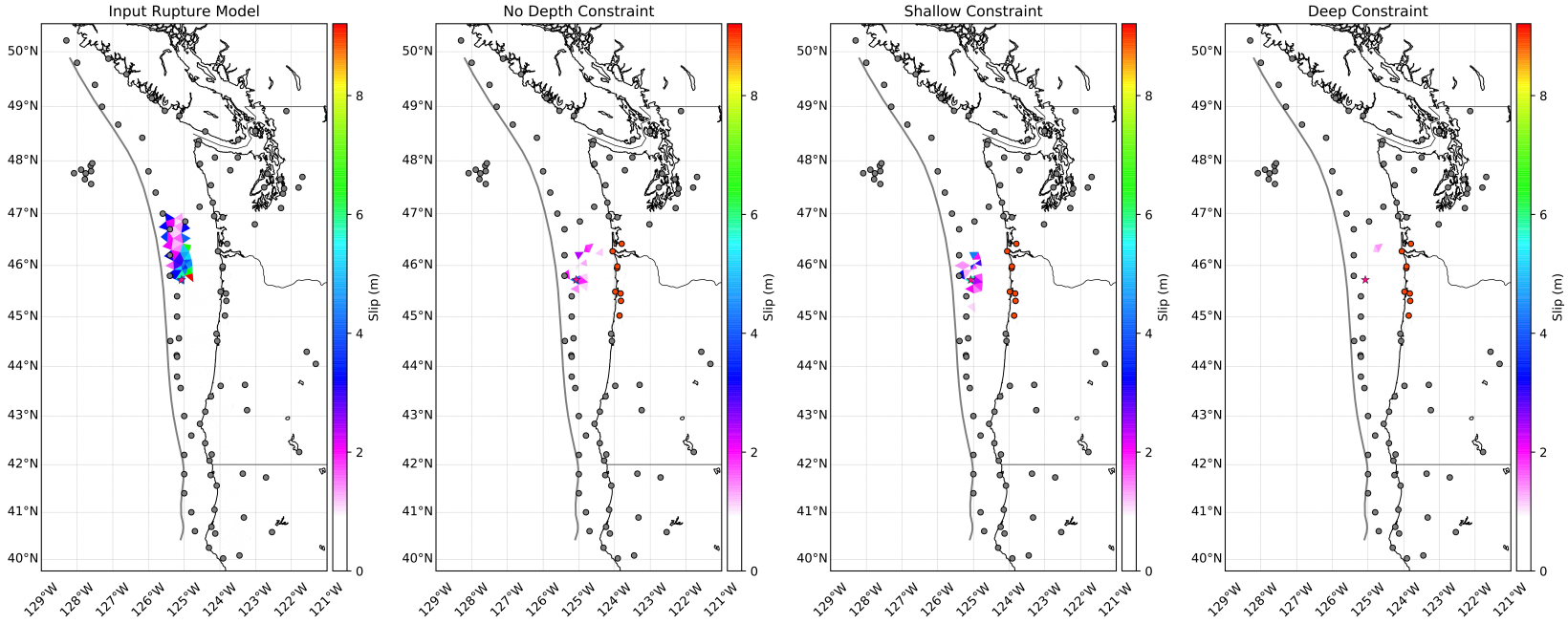

Figure 3.6: Slip solution comparisons using different depth constraints for an example shallow rupture, where the input rupture model is shown on the left. The slip inversions were performed using GNSS displacements only, where the stations used in the inversions are highlighted by the orange circles. The location of the trench is shown by the gray line and the hypocenter of the rupture scenario is shown by the star.

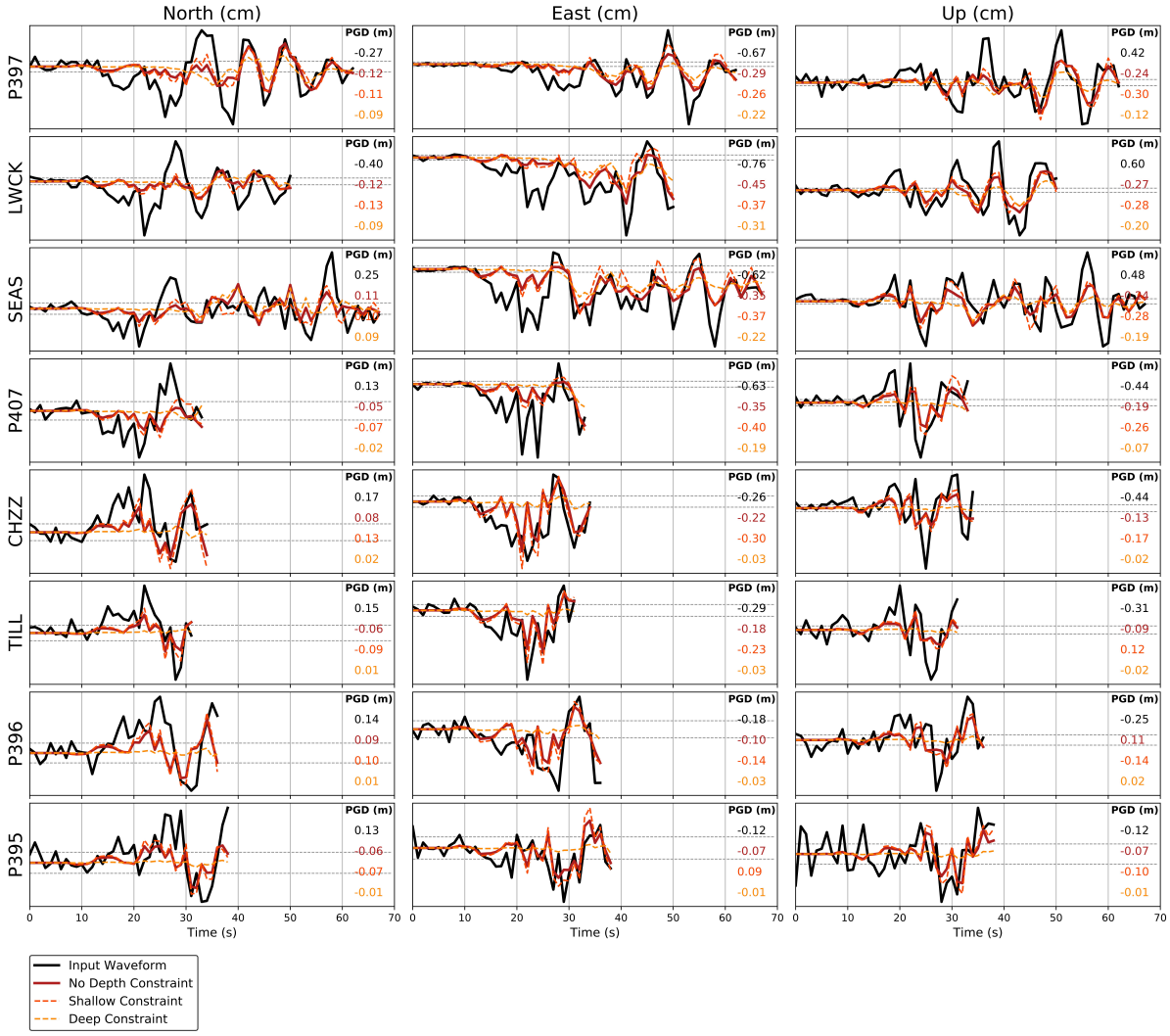

Figure 3.7: Displacement waveform comparisons of the slip inversion solutions for the same example shallow rupture shown in Figure 3.6. The input waveforms are shown in black, while the colored lines show the synthetics reproduced from inversion solutions with different depth constraints. The dashed gray lines show the expected sensitivity of GNSS displacement data at 2.5 cm in the horizontal components and 5 cm in the vertical component. The waveforms are plotted relative to the earthquake origin time, and the stations are arranged from north to south.

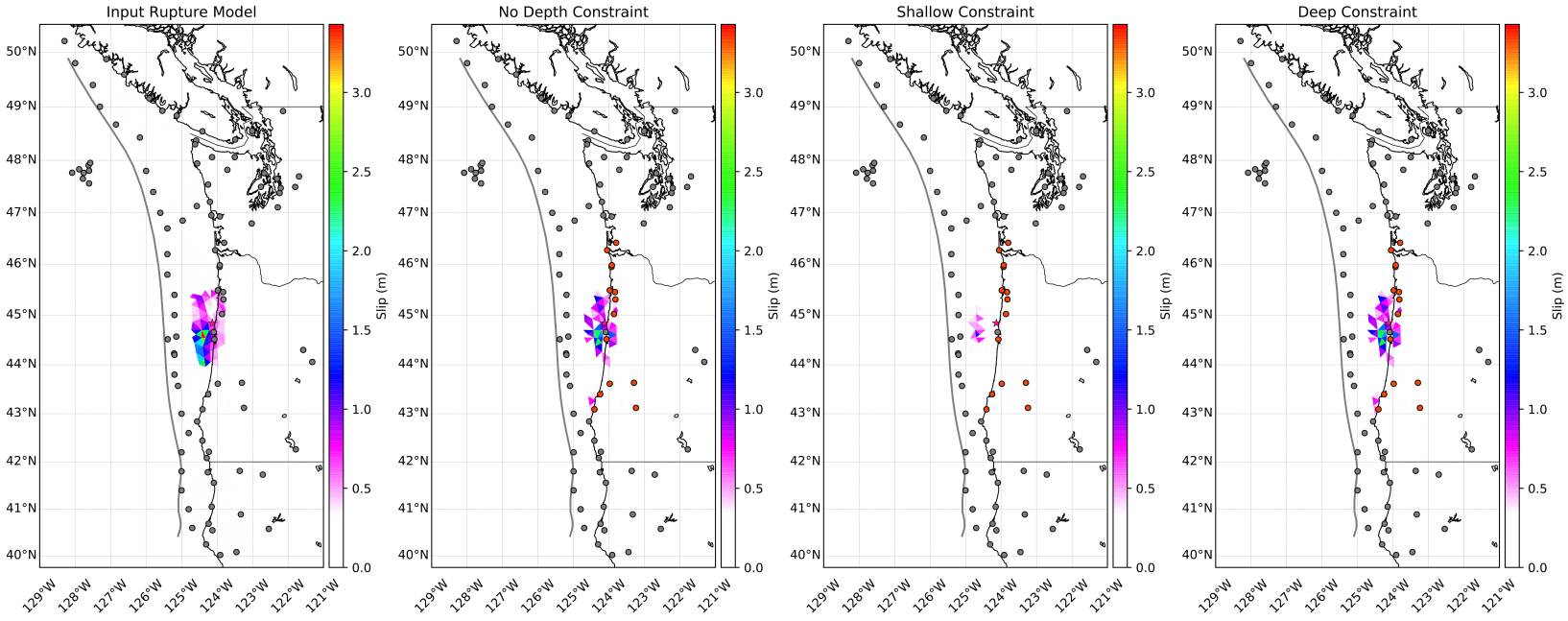

Figure 3.8: Slip solution comparisons using different depth constraints for an example deep rupture, where the input rupture model is shown on the left. The slip inversions were performed using GNSS displacements only, where the stations used in the inversions are highlighted by the orange circles. The location of the trench is shown by the gray line and the hypocenter of the rupture scenario is shown by the star.

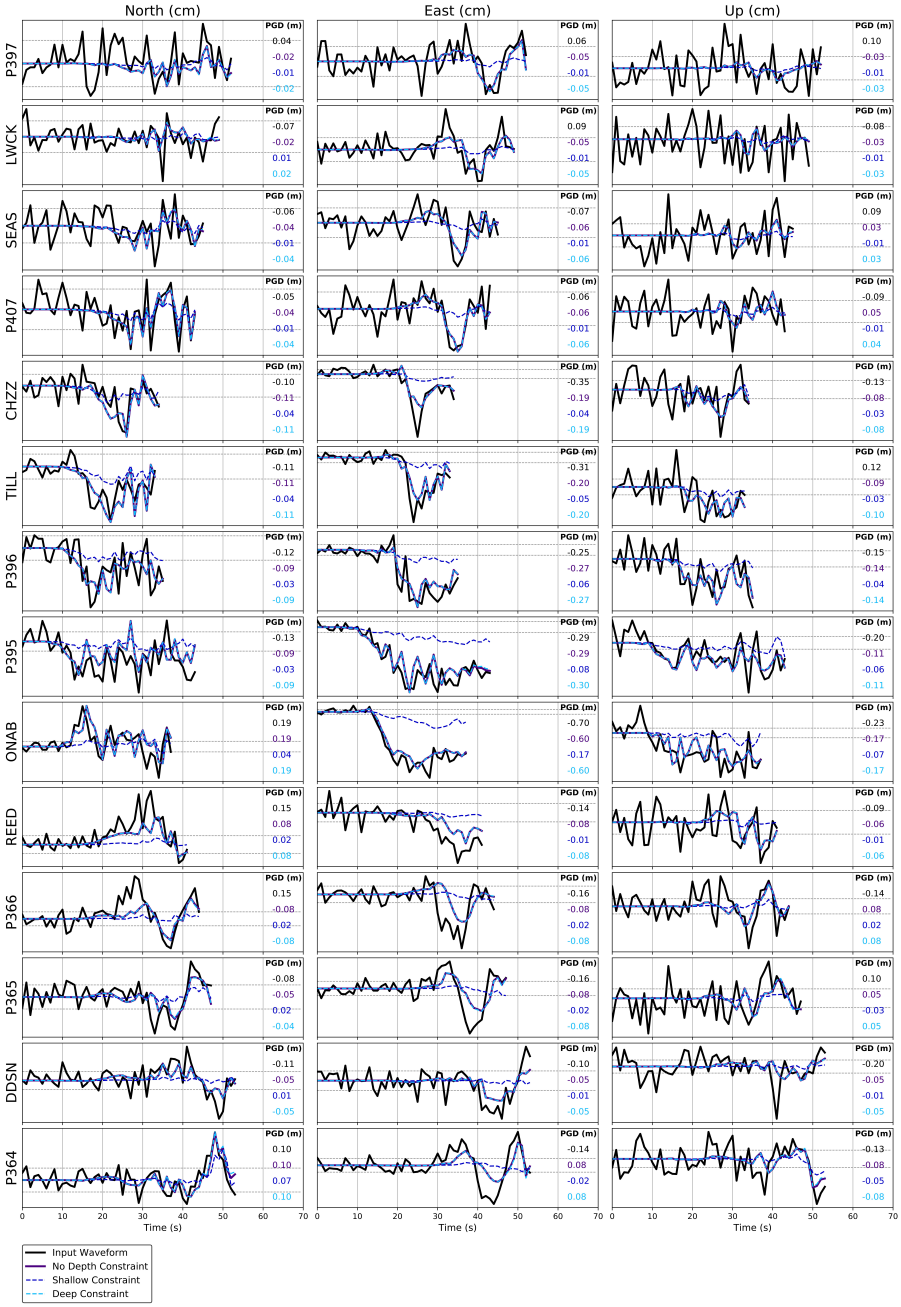

Figure 3.9: Displacement waveform comparisons of the slip inversion solutions for the same example deep rupture shown in Figure 3.8. The input waveforms are shown in black, while the colored lines show the synthetics reproduced from inversion solutions with different depth constraints. The dashed gray lines show the expected sensitivity of GNSS displacement data at 2.5 cm in the horizontal components and 5 cm in the vertical component. The waveforms are plotted relative to the earthquake origin time, and the stations are arranged from north to south.

constraint case significantly underestimates the amount of slip because it is not possible to fit the data with shallow slip. The slip inversions that have no depth constraint and that are constrained to be deeper underestimate slip by approximately 1 m, but generally show the same pattern of slip as the input model. Comparing the displacement waveforms reveal a systematic underestimation in the displacement waveforms for the shallow slip constraint, which is what we expect to happen for a deeper rupture.

Figure 3.10 shows a summary of the slip inversion solutions between the different data types, categorized by rupture type and slip inversion constraint. We compare three measures of data misfit: the normalized error in the PGD at each station, the RMS error to the input displacement waveforms, the misfit of all data used in each inversion. We assess the quality of the retrieved model using the error in magnitude and error in maximum slip. For the hypothesis-testing procedure to allow us to confidently discriminate shallow ruptures from deeper ruptures, waveforms from solutions using the correct depth constraint should exhibit small errors while waveforms from solutions using the incorrect depth constraint should exhibit large errors. For the deeper ruptures, there is a significant difference in the PGD error, where the PGD using the incorrect shallow constraint is grossly underestimated compared to the PGD values from inversions using either no depth constraint or the correct deeper constraint. However, the displacement waveform RMS differences for each depth still have a significant overlap. For the shallow ruptures, neither the PGD error nor the RMS difference in the displacement waveforms show significant differences between the depth constraints.

For all inversions and data types, the PGD is underestimated by at least 20% and none of the inversions have displacement waveform RMS differences below 5 cm, the noise level of high-rate GNSS data in the vertical component. Augmenting the GNSS displacements with collocated velocities and offshore velocities in the inversions does not significantly affect or improve inversion solutions. Velocity-only slip inversions have larger errors likely because these data are not sensitive to the lower-frequency shaking information. Filtering the data to lower

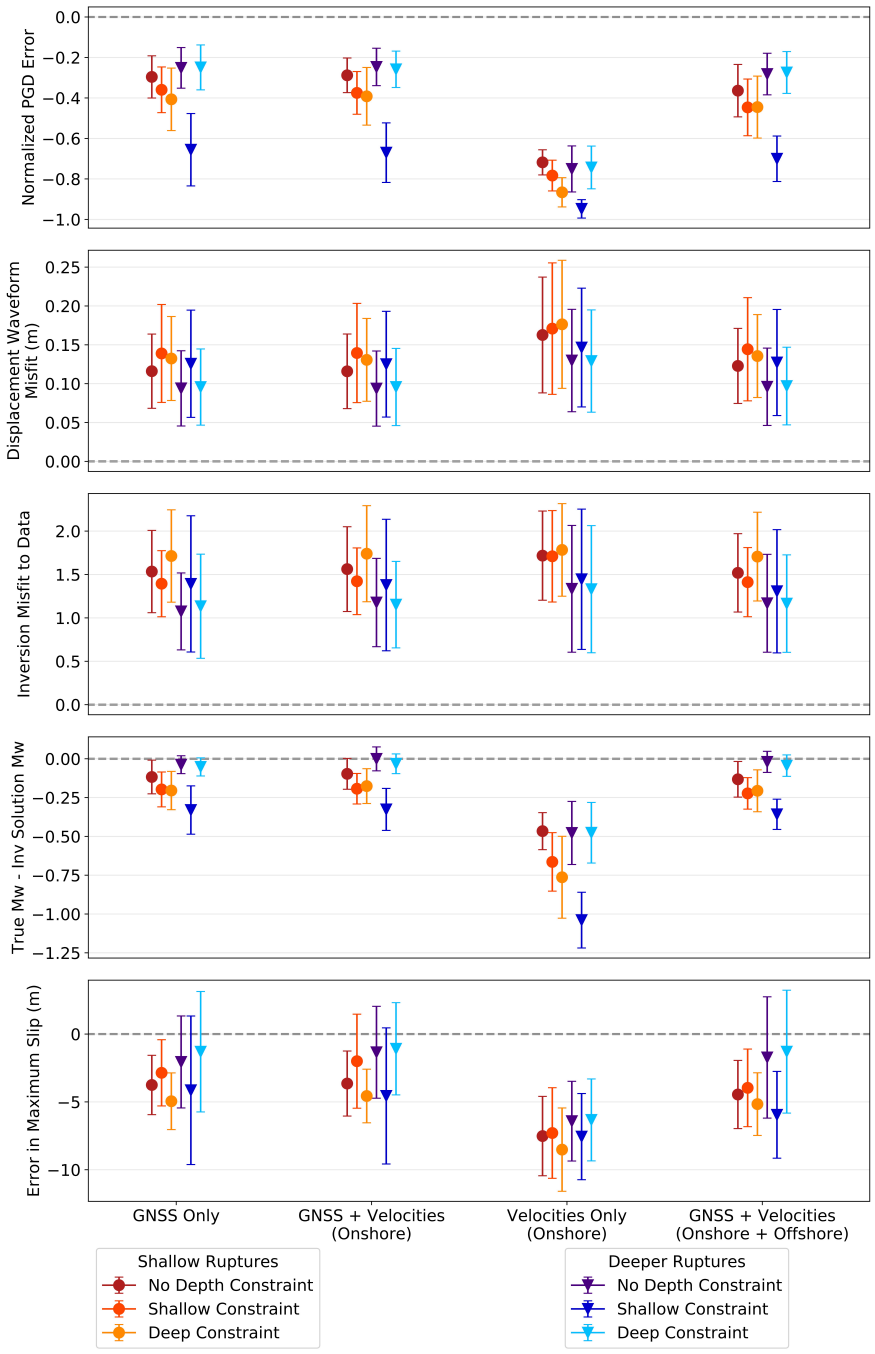

Figure 3.10: Comparison of mean slip inversion results using different combinations of data types, separated by rupture depth. Reds show the mean results for the shallow ruptures, and blues show the mean results for the deeper ruptures. Each rupture type is further separated by the depth constraints used in the slip inversions. For the hypothesis-testing procedure in Table 1 to hold as a good procedure for determining shallow vs. deep slip, the shallow ruptures need to have significantly better slip inversion solutions when using the shallow slip constraint compared to using the deep constraint, and the deeper ruptures need to have significantly better slip inversion solutions when using the deep constraint compared to using the shallow constraint.

frequencies could potentially improve waveform fits, and will be tested in future analysis.

3.5 Discussion

It is likely that our assumptions about the local rise time and the rupture velocity are adding additional errors into the retrieved slip solution because we traded flexibility in the rupture timing to reduce the size of the Green's function matrices to be inverted. We can use the exact values of these parameters from the input rupture models in order to isolate which of our rupture timing assumptions is most affecting the slip inversion results. We perform four sets of slip inversions, using GNSS displacements as the input data, where we use the following rupture timing parameters:

1. Specified local rise time and specified rupture velocity
2. Input local rise time and input rupture velocity
3. Input local rise time and specified rupture velocity
4. Specified local rise time and input rupture velocity

Figure 3.11 shows a summary of the kinematic slip inversion solutions using GNSS displacements as the input data, separated into shallow and deep rupture categories. We observe the PGD error when applying the shallow constraint is clearly separated from the PGD error when applying the deep constraint, thus the shallow hypothesis can be rejected for the case of a deeper rupture. For a shallow rupture, knowing the rupture velocity results in a separation between the PGD error for the different depth constraints and allows for the hypothesis to be able to confirm the presence of shallow slip. For the RMS errors in displacement waveforms, knowing the rupture timing in the inversions allows the hypothesis test to work for the case of a deeper rupture using the RMS error as a criterion, but there is still significant overlap in the RMS error for the shallow

ruptures. Of the two rupture timing parameters considered, knowing the rupture velocity is more important than knowing the exact local rise time. The rupture velocity determines how the slip propagates during the rupture, which affects the timing of shaking at the stations.

A comparison of inversion results with known rupture timing but with different combinations of input data types is shown in Figure 3.12. As shown in the previous figure, knowing the rupture timing allows us to exclude the possibility of slip in the case of a deeper rupture and shallow rupture when using PGD misfit as a criterion. For the RMS misfit error, the error is significantly underestimated when the deeper constraint is incorrectly applied in the inversion, but there are still overlaps in the displacement waveform RMS errors for all the shallow versus deep constraints, so RMS misfit is not as robust a criterion. Augmenting the GNSS displacement data with collocated velocities and offshore velocities significantly changes the misfit results for PGD. The offshore data also allows for more accurate determination of maximum slip values, which could lead to improved tsunami simulations.

3.6 Summary

The local impact of the tsunami generated by a M_w8 megathrust earthquake strongly depends on the depth of the earthquake along the subduction interface. Tsunami earthquakes, which occur in the shallowest portion of the megathrust near the trench, produce anomalously large tsunamis but low amounts of high-frequency shaking for their magnitude. This lack of high-frequency shaking makes it difficult for local populations to know to self-evacuate to higher ground, so near-source tsunami early warning systems need to be able to identify whether a shallow tsunami earthquake has occurred and elevate early warning alert levels if necessary.

In this chapter, we examined how modified kinematic slip inversions utilizing the early portions of near-field displacement and velocity waveforms, from the P-wave onset to PGD, can confirm the presence of shallow rupture using a hypothesis test with different depth-dependent

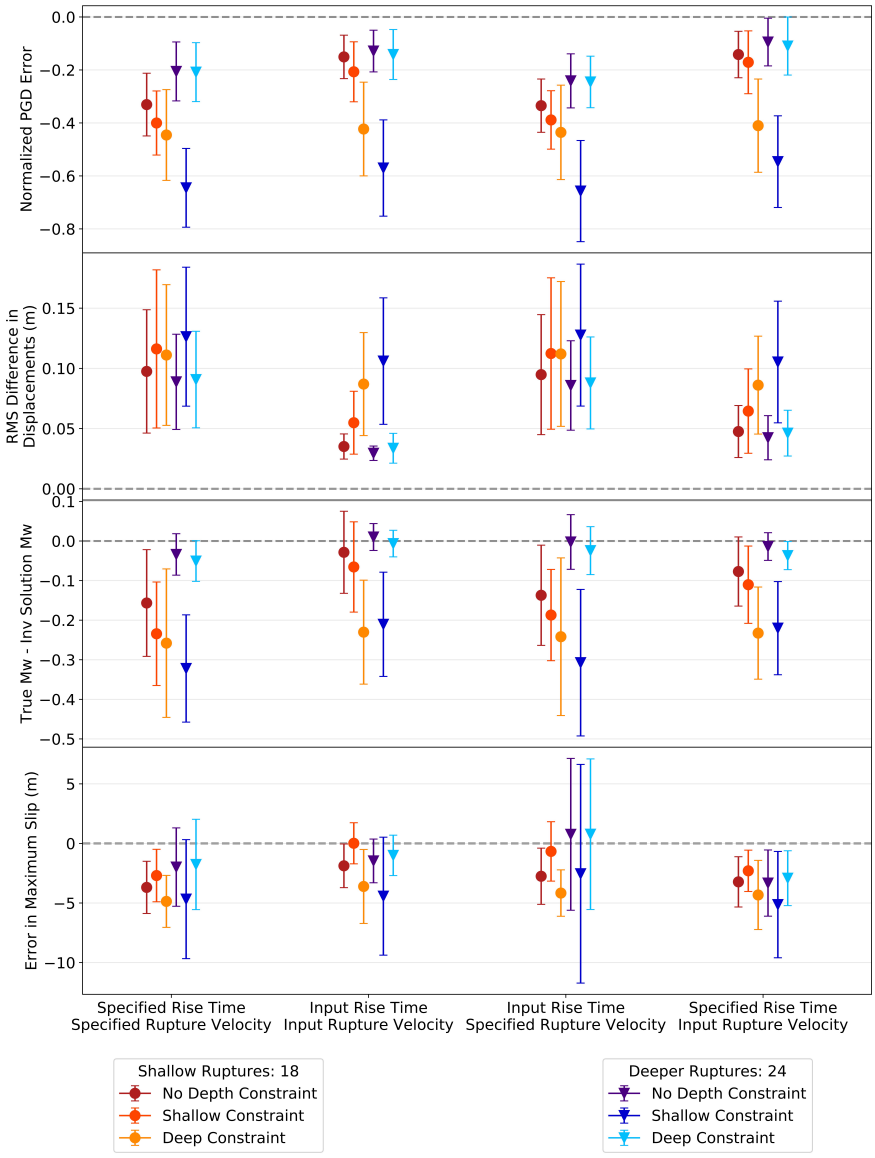

Figure 3.11: Comparison of mean slip inversion results using different timing assumptions, separated by rupture depth. The slip inversion results summarized here used onshore GNSS displacements as the input data. Reds show the mean results for the shallow ruptures, and blues show the mean results for the deeper ruptures. Each rupture type is further separated by the depth constraints used in the slip inversions. For the hypothesis-testing procedure in Table 1 to hold as a good procedure for determining shallow vs. deep slip, the shallow ruptures need to have significantly better slip inversion solutions when using the shallow slip constraint compared to using the deep constraint, and the deeper ruptures need to have significantly better slip inversion solutions when using the deep constraint compared to using the shallow constraint.

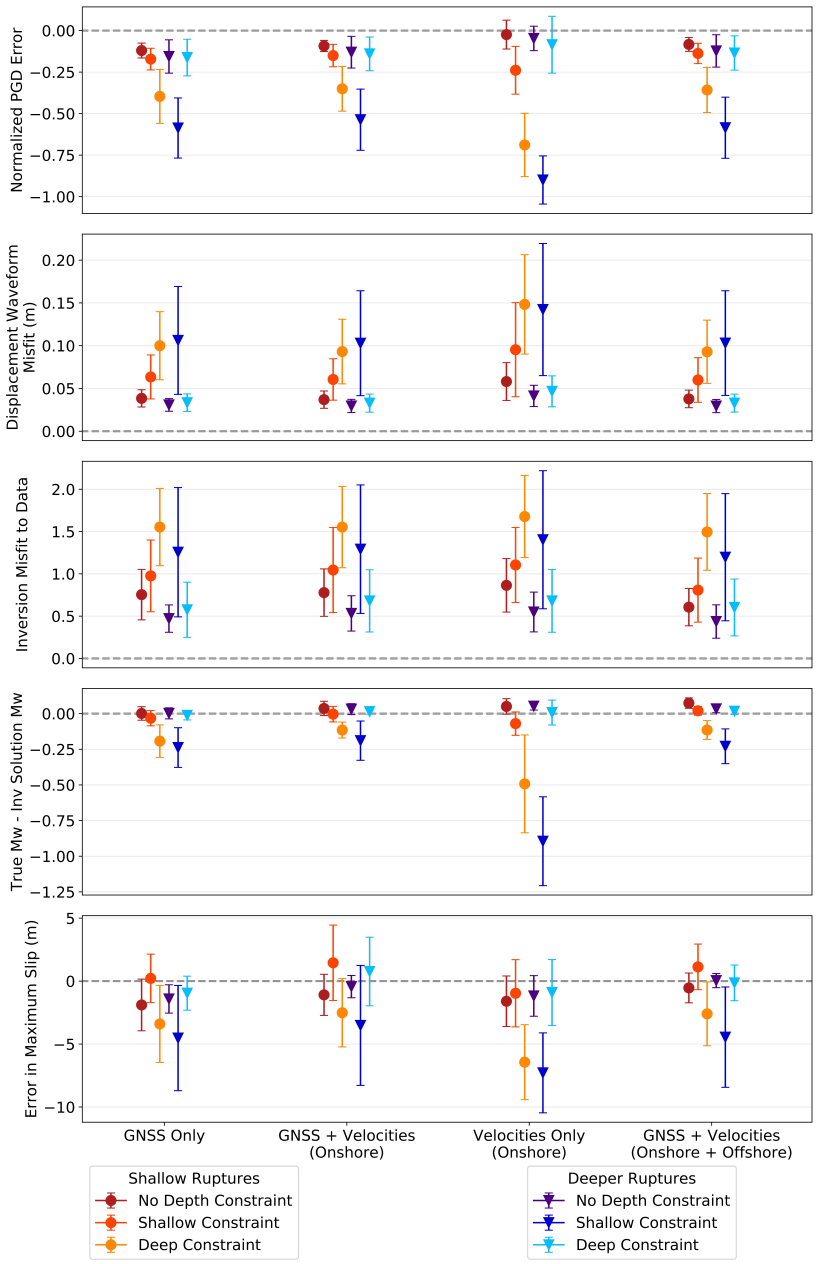

Figure 3.12: Comparison of mean slip inversion results using different data types, separated by rupture depth. The rupture velocity and local rise time values used in the slip inversions are the same as the input rupture scenarios. Reds show the mean results for the shallow ruptures, and blues show the mean results for the deeper ruptures. Each rupture type is further separated by the depth constraints used in the slip inversions. For the hypothesis-testing procedure in Table 1 to hold as a good procedure for determining shallow vs. deep slip, the shallow ruptures need to have significantly better slip inversion solutions when using the shallow slip constraint compared to using the deep constraint, and the deeper ruptures need to have significantly better slip inversion solutions when using the deep constraint compared to using the shallow constraint.

slip constraints. We assessed our approach using kinematic rupture scenarios at different depths that were designed for the Cascadia subduction zone (Melgar et al., 2016). In this preliminary work, we approximated the source time function with a single time window and approximate the rupture velocity in an attempt to reduce the size of the matrix in the inversion problem. In hindsight, these assumptions limited our ability to fit the data more than anticipated, so future work should allow more free parameters for the source time function.

We found that inversions using GNSS displacement waveforms show significant differences in recovered PGD values for a deeper rupture depending on the depth-constraint used, where using the incorrect shallow constraint results in a significantly underestimated PGD value. PGD error was a much more robust measure to use for the misfit criterion than the RMS error because differences in overall waveform fits for deeper ruptures are not significant between the depth constraints, which make it difficult to confirm the presence of deeper slip and exclude the possibility of shallow slip. The RMS data misfit for all cases is also above the noise level of the data for all inversions. Adding additional data in the form of onshore and offshore velocity waveforms do not improve the overall data misfit values nor do they separate the inversion solutions using the different depth constraints. Further investigation into the timing approximations used to modify the kinematic inversions indicates that errors in the rupture velocity are the biggest contributors to the uncertainties in the slip inversion results.

If the timing of the rupture is known, specifically the rupture velocity, the data misfit, in particular PGD error, for the inversion solutions of a deeper rupture can be used to confirm that the rupture is deep even when only the GNSS displacement waveforms are used in the inversion. The differences are even greater when offshore velocities are used. This suggests that incorporating more flexibility in the slip inversions with regard to the rupture timing may improve data misfit when the correct depth constraint is used. Future work will examine whether adding two additional time windows into the slip inversion, one slightly slower and the other slightly faster than the approximated rupture velocity, will improve rupture timing and therefore reduce

data misfit for the correct depth constraint.

3.7 Acknowledgements

Chapter 3 is currently being prepared for publication, and is coauthored with Jennifer Haase. The dissertation author is the primary investigator and author of this material.

This work has been funded by NASA grand NNX16AO32H through the NASA Earth and Space Science Fellowship. We thank Diego Melgar for assistance in the use of the the FakeQuakes code (github.com/dmelgarm/FakeQuakes). Kinematic rupture model forward modeling and slip inversions utilized the MudPy software (github.com/dmelgarm/MudPy). Green's functions were computed using the frequency-wavenumber method of Zhu and Rivera (2002) as implemented in the fk code (www.eas.slu.edu/People/LZhu/downloads/fk3.2.tar).

Chapter 4

Seismogeodesy using GPS and low-cost MEMS accelerometers: perspectives for earthquake early warning and rapid response

4.1 Abstract

The seismogeodetic method computes accurate displacement and velocity wavefoRMS by optimally extracting high-frequency information from strong motion accelerometers and low-frequency information from collocated Global Positioning System (GPS) instruments. These broadband observations retain the permanent (static) displacement, are immune to clipping and magnitude saturation for large earthquakes, and are sensitive enough to record P-wave arrivals. These characteristics make seismogeodesy suitable for real-time applications such as earthquake early warning. The Scripps Institution of Oceanography (SIO) has developed an inexpensive Micro-Electro-Mechanical Systems (MEMS) accelerometer package to upgrade

established GPS stations. We compare the performance of our MEMS accelerometer to an observatory-grade accelerometer using an experiment at the University of California San Diego Large High-Performance Outdoor Shake Table. We show that the two types of accelerometers agree in frequency ranges of seismological and engineering interest, and produce equivalent seismogeodetic estimates of displacement and velocity. To date, 27 SIO MEMS packages have been installed at GPS monitoring stations in southern California and the San Francisco Bay Area and have recorded four earthquakes (M4.2, M4.1, and two of M4.0). The P-wave arrivals are distinguishable in the seismogeodetic observations at distances of up to $\sim$25 km away, but not in the GPS-only displacements. There is no significant permanent deformation for these small events. This study demonstrates the lower limit of detectability, and that seismogeodetic wavefoRMS can also be a reliable early confirmation that an event is not large or hazardous. It also raises the possibility of rapid magnitude estimation through scaling relationships.

4.2 Introduction

Earthquake early warning and rapid response using traditional seismic instruments rely on near-field data to minimize the time between earthquake origin and issuance of a warning (Allen et al., 2009 and references therein). For large magnitude earthquakes, ground motions can exceed the dynamic range of seismometers, thus, seismic networks also include strong motion accelerometers whose lower gains permit the on-scale recording of ground accelerations. The accelerometers are designed to have high enough dynamic range to measure regional earthquake signals from small-magnitude earthquakes ($\sim$M3.5), yet not clip when the instrument experiences strong local shaking. The relationship between magnitude and ground displacement derived using seismic sensors reaches saturation for large earthquakes, making it difficult to discern the earthquake magnitude above a certain threshold with rapidly-available near-field acceleration data (Brown et al., 2011; Hoshiba & Ozaki, 2014). Rapid magnitude estimates that rely on

teleseismic methods (Kanamori & Rivera, 2008; Duputel et al., 2011; Hayes et al., 2011) are not timely enough for earthquake early warning. Reliable estimation of large earthquake magnitude from near-field accelerometers requires the integration and double integration of acceleration wavefoRMS into velocity and displacement wavefoRMS, respectively. Such a calculation yields velocities and displacements with unrealistic drift because integration amplifies small errors, known as baseline offsets, in the acceleration data. The cause of these baseline offsets remains largely unresolved, however, potential sources have been suggested, including numerical error in integration, cross-axis sensitivity, and unmodeled tilts and rotations (Graizer, 1979; Iwan et al., 1985; Boore, 1999; 2001; Boore et al., 2002; Emore et al., 2007; Smyth & Wu, 2007).

Great effort has been made to develop automated correction schemes for removing baseline drift in integrated acceleration data. The simplest approach involves highpass filtering the integrated waveform (Boore & Bommer, 2005). Filtering results in the loss of the static offset, which is an impediment to accurate magnitude estimation in real time. More complicated methods have been explored (Iwan et al., 1985; Boore, 1999; 2001; Emore et al., 2007; Wu & Wu, 2007; Chao et al., 2010), including utilization of the GPS static offset from post-processing as a constraint (Wang et al., 2011; Wang et al., 2013). These approaches can produce wavefoRMS with complicated errors present from the static offset (0 Hz) up to $\sim$0.5 Hz, thus rendering them unreliable for earthquake early warning (Melgar, Bock et al., 2013). This suggests that accurate baseline corrections require a greater constraint than just the static offset from GPS measurements. In any case, the static offset is not accurately available until seismic shaking has ended, which can be 2-3 minutes for great earthquakes such as the 2011 M_w9.0 Tohoku-oki, Japan earthquake (Simons et al., 2011).

GPS observations can also be used to estimate dynamic displacements (Nikolaidis et al., 2001; Larson et al., 2003; Bock et al., 2004; Langbein & Bock, 2004; Genrich & Bock, 2006; Larson, 2009), as well as static displacements, and have been applied to earthquake early warning (Blewitt et al., 2006; Crowell et al., 2009; Allen & Ziv, 2011; Colombelli et al., 2013; Grapenthin

et al., 2014). Direct geodetic measurements of broadband displacements with GPS are well-suited in the near field of significant earthquakes as arbitrarily large displacements can be detected without clipping (Larson et al., 2003; Bock et al., 2004). Furthermore, magnitude saturation for large earthquakes is avoided when using displacement directly without filtering (Crowell et al., 2013; Melgar et al., 2015). A growing number of earthquakes have been observed and modeled in post-processing with high-rate GPS (1 Hz or greater) in the near-source of medium or larger earthquakes for a variety of fault mechanisms (Miyazaki et al., 2004; Ozawa et al., 2011; Crowell et al., 2012; O'Toole et al., 2012; Ohta et al., 2012; Wright et al., 2012; Melgar, Crowell et al., 2013; Galetzka et al., 2015), with some studies also including accelerations as independent observations (Ji et al., 2004; Kobayashi et al., 2006). GPS has an advantage over strong motion data by measuring displacement directly and in an absolute frame of reference. Translational motion can be determined with uncertainties less than 2-3 cm in real-time analysis (Geng et al., 2013), with the remaining errors mainly due to residual ionosphere and troposphere interferences and multipath (Genrich & Bock, 2006). Hence, GPS data are systematically noisier than seismic data.

The correction for acceleration baseline offsets through comparison with 30 s GPS data was introduced by Nikolaidis et al. (2001) for the 1999 M_w7.1 Hector Mine, California earthquake. Emore et al. (2007) used 1 Hz GPS data from the 2003 M_w8.3 Tokachi-oki, Japan earthquake to correct the acceleration wavefoRMS and determine the characteristics and timing of the baseline offset errors, however the least squares method requires the use of the entire GPS waveform so cannot be applied in real time. The optimal combination of GPS and accelerometer data with a Kalman filter (Smyth & Wu, 2007), suitable for real-time analysis, was shown to yield both broadband displacement and velocity wavefoRMS that incorporate the strengths of each data type while minimizing their weaknesses (Bock et al., 2011; Geng et al., 2013). Unlike GPS alone, the seismogeodetic combination of GPS and accelerometer data can distinguish P-wave arrivals in the estimated velocity wavefoRMS, a distinct advantage for earthquake early warning and rapid

magnitude estimation, in particular for large earthquakes (Crowell et al., 2012; Melgar & Bock, 2015).

Bock et al. (2011) introduced the seismogeodetic combination using a Kalman filter with data from an experiment on the Network for Earthquake Engineering Simulation at University of California, San Diego (NEES@UCSD) Large High-Performance Outdoor Shake Table (LHPOST) as well as data from the 2010 M_w7.2 El Mayor-Cucapah, Mexico earthquake. The Kalman filter does not require any assumption as to the nature of baseline offsets incurred with accelerometer data. With every acceleration data point, the Kalman filter computes displacement and velocity from acceleration assuming a constant acceleration between samples. When the filter encounters a sample that contains both an acceleration measurement and a GPS observation, it uses a predetermined weighting scheme to correct the computed displacement and velocity using the GPS displacement observation. Thus, the Kalman filter corrects for baseline drift due to accelerometer integration. Although the Kalman filter combination procedure for the datasets in Bock et al. (2011) and this paper were applied retrospectively, the Kalman filter operates on a sample-by-sample basis so it can function in real time without user interaction. The addition of a backwards Kalman smoother in the seismogeodetic combination yields better solutions than the simple forward Kalman filter because the Kalman smoother incorporates multiple GPS and acceleration observations in the computation of the solution (Bock et al., 2011). However, the backwards Kalman smoother requires a moving time window to operate in real time. A time sample ratio of 1:20 for GPS to accelerometer sampling was sufficient to remove sawtooth artifacts from the combined solution (Bock et al., 2011). Increasing the GPS sampling frequency to 5 Hz would then allow the Kalman smoother to operate with only a 2 second lag, with little increase in computation time. Some compromise in data rate and accuracy would be necessary for application to earthquake early warning. An alternate option for reducing data transmission rates for GPS data would be to calculate precise point GPS solutions and the Kalman filter combination on-site rather than transmitting the 5 Hz GPS observables.

The choice of weights for each data type (GPS and accelerometer) is important to avoid baseline drift while still allowing the combined dataset to be informed by the most reliable information of both data types. Bock et al. (2011) chose the Kalman filter weights by computing the variance of pre-event noise in both data sets and scaling up the pre-event acceleration variance. This accounts for an increase in error caused by baseline offsets incurred during strong motion not present in the ambient pre-event accelerations. In their analysis, Bock et al. (2011) determined an acceleration variance multiplier of 10-100 to be optimal for use in the forward Kalman filter, while the multiplier did not significantly change the solution using the Kalman smoother. We will show that while this is the case for observatory-grade accelerometer data, an acceleration variance multiplier is necessary when using Micro-Electro-Mechanical Systems (MEMS) accelerometer data.

The implementation of real-time seismogeodetic analysis requires collocated seismic and geodetic instrumentation. Unfortunately, the independent development of seismic and geodetic networks has resulted in only a sparse set of collocated stations in the Western U.S. and elsewhere. Upgrading GPS monitoring stations with observatory-grade accelerometers to form collocated stations is prohibitive for a large network due to the high costs of these instruments. A more affordable option can be found by utilizing MEMS sensors. MEMS accelerometers have been tested for seismic applications (Evans et al., 2014), incorporated into dense concentrated seismic networks (Cochran et al., 2009; Clayton et al., 2012), and considered in combination with inexpensive smart-phone GPS receivers for earthquake early warning (Minson et al., 2015). The proof-of-concept of the seismogeodetic approach to baseline correction was performed using MEMS-Piezoresistive MSI model 3140 accelerometers with 50 Hz Navcom NCT-200D GPS receivers on a full-scale seven-story building at the NEES@UCSD LHPOST (Bock et al., 2011). In that study, seismogeodetic solutions were found to have a root mean square accuracy of 1.5-3.8 mm (Bock et al., 2011) when the seismogeodetic wavefoRMS were compared with input displacements to the LHPOST based on accelerometer data collected for several earthquakes.

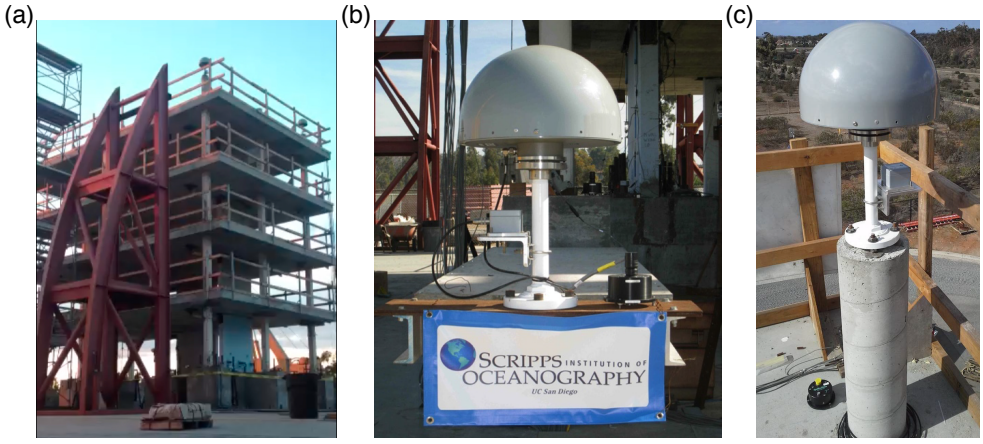

Figure 4.1: **(a)** View of the southwest corner of the half-scale, four-story structure used in the NEES@UCSD LHPOST experiment. Two of the GPS antenna/SIO MEMS accelerometer collocations can be seen on the roof. **(b)** The GPS/SIO MEMS collocation on the foundation extension beam. The Topcon NET-G3A GPS receiver is beneath the radome on the top and the SIO MEMS is housed in the gray box on the side of the steel antenna mount. The EpiSensor accelerometer EPIA is the small black instrument located to the right of the GPS antenna mount. A second EpiSensor, EPIB, is located on the LHPOST foundation and can be seen in the background. **(c)** The GPS/SIO MEMS collocation on the northwest corner of the roof. The roof antenna mount is bolted to concrete pillars attached to the rooftop. The rooftop EpiSensor is located on the floor next to the pillar mount.

For the purposes of affordable seismogeodetic monitoring for earthquake early warning and rapid response, we developed the SIO Geodetic Module and low-cost MEMS Accelerometer Package ("GAP") designed as a simple plug-in for existing GPS stations. The Geodetic Module is an instrument that receives, time tags, buffers, analyzes, and transmits data from multiple sensors (GPS receivers, accelerometers, and meteorological instruments). To date, SIO GAPs have been installed at 17 existing GPS stations in southern California; ten are EarthScope Plate Boundary Observatory (PBO) stations operated by UNAVCO for the NSF, and seven are stations from the Southern California Integrated GPS Network (SCIGN). This network covers the San Andreas, San Jacinto, and Elsinore faults. There are also SIO GAPs installed at 10 PBO GPS stations in the San Francisco Bay Area spanning the Hayward and Rodger's Creek faults.

Here, we assess the performance of the SIO GAP with a MEMS accelerometer ("SIO MEMS") compared to seismogeodetic monitoring with an observatory-grade Quanterra Q330

recorder with three-component Kinemetrics EpiSensor ES-T accelerometer using experiments on a half-scale four-story structure on the NEES@UCSD LHPOST in December 2013 and January 2014. We first compare the two types of accelerometers directly in the frequency domain. Then, we find the optimal acceleration weights in the Kalman filter for each instrument, and compare the seismogeodetic solutions using both accelerometer types. Finally, we assess the performance of the SIO GAPs in recording several ∼M4 earthquakes in the Bay Area and the Salton trough in southern California.

4.3 Testing the SIO GAP Performance using a Shake Table Building Experiment

In order to assess how the SIO GAP seismogeodetic solutions will perform in the field when a significant event occurs, we tested the instruments in an experiment of a building structure at the NEES@UCSD LHPOST. Here, we compare the seismogeodetic solutions using the SIO MEMS accelerometer to those using the more sensitive three-component Kinemetrics EpiSensor ES-T accelerometer for a series of input motions.

4.3.1 Experimental Setup on the NEES@UCSD LHPOST

The seismogeodetic instrument sets, GPS geodetic receivers with SIO GAPs, were installed on a partially precast concrete four-story structure constructed at half-scale on the LHPOST (Figure 4.1a). The LHPOST moves along a single axis in the east-west direction. However, the building design included three main earthquake resisting walls in an eccentric layout, resulting in significant torsional response that was observed on the north-south axis of the instruments (Fleischman et al., 2015). The asymmetrical building design produced tilts and rotations on the roof that far exceeded the expected response for a typical building or regional monitoring station.

Table 4.1: Design Basis Earthquake (DBE) simulations used during this NEES@UCSD LHPOST experiment. Waveform frequencies were scaled by square root 2 to account for the half-scale structure.

EQ Name	Intensity	Site	Target Level	Historic Earthquake	Record	Scaled PGA (g)	Scale Factor
SE05	Moderate	Seattle, WA	DBE	1979 Imperial Valley	El Cerrito Array #5	0.59	1.14
BE05	High	Berkeley, CA	DBE	1989 Loma Prieta	Los Gatos Presentation Center	0.41	0.72

Still, it serves as a test of the SIO GAP seismogeodetic combination under extreme conditions.

Shake table input control accelerations were based on finite impulse response bandpass-filtered recordings of observed ground motions between 0.25 and 25 Hz, with the highest operational frequency of the LHPOST being 33 Hz (Conte et al., 2004; Fleischman et al., 2015). This frequency band is well below the Nyquist frequencies of the accelerometers. White noise tests at 0.03g RMS (with peak acceleration amplitudes of approximately 0.1g) were run for a variable duration of 100 to 200 seconds at the beginning and end of each series of tests to detect modal changes due to structural weakening.

Earthquake tests were based on strong-motion recordings from previous events and scaled by the square root of two in frequency to meet similitude requirements. A recording from the 1979 M_w6.6 Imperial Valley earthquake, scaled by 1.14 (PGA 0.59g), was used to represent the Design Basis Earthquake (DBE) appropriate for seismic hazard in Seattle, WA. Similarly, a recording of the 1989 M_w6.9 Loma Prieta earthquake, scaled by 0.72 (PGA 0.41g), was used to represent the DBE in Berkeley, CA (Merritt, 1996; FEMA, 2004; Petersen et al., 2014; Fleischman et al., 2015). In addition to testing the DBE-type event, the structure was subjected to simulations of lesser and greater intensity, corresponding to the Service Earthquake (SE) and Maximum Considered Earthquake (MCE). A detailed summary of input testing is available in Table 4.1.

Topcon NET-G3A GPS receivers were installed in six locations on the building: each of

the four corners of the roof, the roof center, and the northwest corner of the foundation (Figure 4.1). The roof instruments were mounted on short steel masts bolted to concrete pillars while the foundation instruments were mounted on a steel beam supported by an A-frame for enhanced rigidity extending west from the northwest corner of the structure. The purpose of this setup at the foundation was to increase GPS satellite coverage. Nonetheless, multipath effects and obstructed sky visibility caused problems at this location during many of the tests. The tests for which good-quality GPS solutions were possible at the foundation are listed in Table 4.2. At all six locations, the SIO MEMS accelerometers were attached to the masts used to mount the GPS antennas (Figure 4.1) and leveled and orientated in a local frame. Observatory-grade Kinemetrics EpiSensor accelerometers were installed in three locations: the first on the roof next to the northwest GPS antenna, a second collocated with the foundation GPS antenna at the end of the foundation extension beam, and a third on the foundation adjacent to the base of the extension beam (Figure 4.1b,c). The EpiSensor collocated on the extension beam failed part-way through the experiment and was replaced with a new instrument.

Relative displacements were computed in real time at 10 Hz using only the GPS data using the Real Time Displacement (RTD) software (Bock et al., 2000) using IGS ultra-rapid orbits. We recorded, but did not process, the GLONASS data for this experiment. A GPS reference station was placed 70 m west of the LPHOST. Relative positioning using a nearby reference station allows us to avoid a factor of 10.4 increase in GPS data variance caused by errors incurred through the ionosphere correction, compared to processing the L1 and L2 phase observations independently (Genrich & Bock, 1992). In practice, however, it is desirable to run a GPS monitoring network using precise point positioning (PPP) at individual stations so that the retrieved ground displacements at a site are not affected by ground motion at the reference site. A comparison of the real-time relative displacement solutions to retrospective PPP-AR (PPP with ambiguity resolution; Geng et al., 2013) displacements for one of the rooftop stations is shown in Figure 4.2. PPP-AR displacements could not be computed for the foundation station

Table 4.2: Information about the shake table tests that were performed during the NEES@UCSD LHPOST experiment. MCE is Maximum Considered Earthquake, using 1.5 times the amplitude of the DBE. SE is the Service Earthquake using 2/3 the amplitude of the DBE.

Test Day	Total Test #	Test #	Simulation Type	Good Foundation East GPS?
1	1	1-W1	White Noise	
	2	1-1	Berkeley SE	yes
2	3	1-W2	White Noise	
	4	1-2	Berkeley SE	yes
	5	1-3	Seattle DBE	
	6	1-4	Berkeley DBE	
	7	1-W3	White Noise	
3	8	1-W4	White Noise	
	9	1-5	Berkeley SE	
	10	1-6	Seattle DBE	
	11	1-7	Berkeley DBE	
	12	1-W5	White Noise	
	13	1-W6	White Noise	
	14	1-8	Berkeley DBE	
	15	1-9	Seattle MCE	yes
	16	1-10	Berkeley MCE	yes
	17	1-W7	White Noise	
4	18	1-W8	White Noise	
	19	1-11	Berkeley DBE	yes
	20	1-12	Berkeley MCE	yes
	21	1-W9	White Noise	
5	22	1-W10	White Noise	
	23	1-13	Berkeley DBE	yes
	24	1-14	Berkeley MCE	
	25	1-W11	White Noise	
6	26	1-W12	White Noise	
	27	1-15	Seattle DBE	
	28	1-16	Berkeley SE	yes
	29	1-17	Berkeley DBE	yes
	30	1-W13	White Noise	
7	31	1-W14	White Noise	
	32	1-18	Berkeley DBE	
	33	1-W15	White Noise	
	34	1-19	Berkeley MCE	yes
	35	1-W16	White Noise	
8	36	1-W17	White Noise	
	37	1-20	Berkeley DBE	yes
	38	1-W18	White Noise	
	39	1-21	Berkeley MCE	yes
	40	1-22	Berkeley MCE	
	41	1-W19	White Noise	

due to the inhibited satellite visibility. The close agreement between the two types of solutions on the rooftop, in particular in the east direction corresponding to the primary platen motion, indicates that the accuracy level achievable using PPP-AR is indicative of a real-world scenario, with slightly increased background noise in the vertical component (up to 1 cm) representing the limiting noise level. This will be illustrated further in the analysis of the field recording of earthquake data using the PPP-AR method in the second part of the paper.

The accelerometer data were streamed in real time at 100 Hz into the central servers at the Scripps Orbit and Permanent Array Center (SOPAC). Seismogeodetic displacement and velocity solutions were computed after-the-fact using the Kalman filter with backwards smoothing described in Bock et al. (2011), using a smoothing window of 50 s. The pre-event means of the first 15 s of both displacement and acceleration data were removed from the time series before computing the seismogeodetic solutions. For real-time implementation, the bias in both the GPS and accelerometer time series will be calculated from data stored in a pre-event buffer when strong shaking is detected on the accelerometer. In addition, an acceleration bias can be added as a parameter in the Kalman filter algorithm (Melgar & Bock, 2015).

The scope of the experiment included a total of 19 white noise tests and 22 earthquake tests that we have used to assess the performance of the SIO MEMS accelerometers in the SIO GAPs through direct comparison with the observatory-grade EpiSensor accelerometer in the frequency domain. Of the earthquake simulations, 12 tests had high-quality GPS displacements in the primary direction of motion at the foundation station, with no evidence of offsets due to apparent cycle slips or incorrectly resolved integer-cycle phase ambiguities (Table 4.2). We use these earthquake simulations to optimize the seismogeodetic solutions using both types of accelerometers, demonstrating the appropriate choice of Kalman filter weight for each instrument. We show that with proper weighting, the seismogeodetic combinations using the SIO MEMS are in agreement with those using the observatory-grade accelerometers.

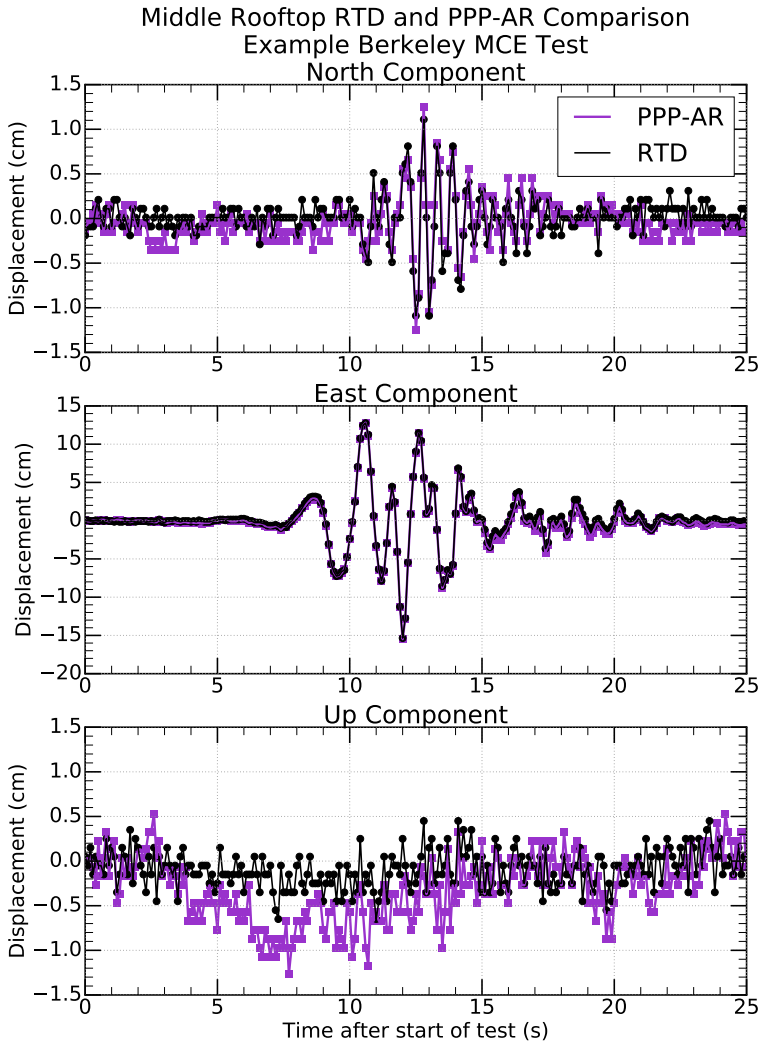

Figure 4.2: Comparison between the Real Time Displacement (RTD) and PPP-AR GPS displacements for the middle roof GPS station during an example LHPOST test. The RTD network solutions were computed in real time using a reference station 70 m from the shake table and are the input GPS data for the seismogeodetic combination analysis. The PPP-AR solutions were processed after-the-fact using the final orbits and satellite clock parameters. PPP-AR is the positioning technique used for the earthquake field observations examined in this work, which is required for an earthquake when the nearby reference sites may also be moving. This figure quantifies the small decrease in accuracy (1.5 cm in the vertical) of typical field observations, compared to the optimal experimental conditions available at the shake table.

4.3.2 Direct Comparison of SIO MEMS and Observatory-Grade EpiSensor Accelerations

The MEMS accelerometer in the SIO GAP contains a 12-bit 3-axis digital Kionix KXR94-2353 (MEMS) accelerometer with a range of $\pm 2g$ (1 bit sensitivity of 0.01 m/s^2) and maximum bandwidth of 800 Hz. The MEMS sensor is lowpass filtered to 50 Hz via a single pole filter then decimated to 100 Hz before output. The sensitivity of the instrument is stated to be -38 decibels (dB). The accelerometer chip itself is installed on a circuit card inside a waterproof enclosure. Its microprocessor precisely controls sample timing; it is slaved to the station GPS receiver time 1 PPS outputs that are received from the Geodetic Module. The accelerometer package bolts to the vertical leg of a PBO/SCIGN antenna monument or the antenna mount on a building monitoring site (Figure 4.1b) and has all-axis mechanical leveling and orientation capabilities. The SIO Geodetic Module streams over IP the time-tagged 100 Hz SIO MEMS accelerometer data. The Geodetic Module is packaged in a rugged enclosure measuring 7.09" x 5.51" x 2.75" and is designed to control up to three external sensors (e.g., MEMS accelerometer, meteorological instrument package, gyroscope) as well as any geodetic-quality GPS receiver that streams RTCM3 messages. The Geodetic Module also has two TCP ports for I/O operations.

The Kinemetrics EpiSensor force balance accelerometer, FBA ES-T, consists of three EpiSensor force balance accelerometer modules mounted orthogonally in one package with a user selectable range of up to $\pm 4g$, dynamic range of 155 dB+, and bandwidth from DC to 200 Hz. A 24-bit Quanterra digital recorder was used with a 40 Hz lowpass anti-aliasing filter sampling at 200 Hz. The instrument response is flat from DC to 200 Hz, thus we take the EpiSensor accelerations as the true recording of the shake table motion.

We compare the SIO MEMS with the EpiSensor in the frequency domain, computing acceleration power spectra using a multi-time window method with Slepian tapers (Slepian, 1978). All acceleration power spectra are shown in dB relative to 1 (m/s^2)^2/Hz. Figure 4.3 shows

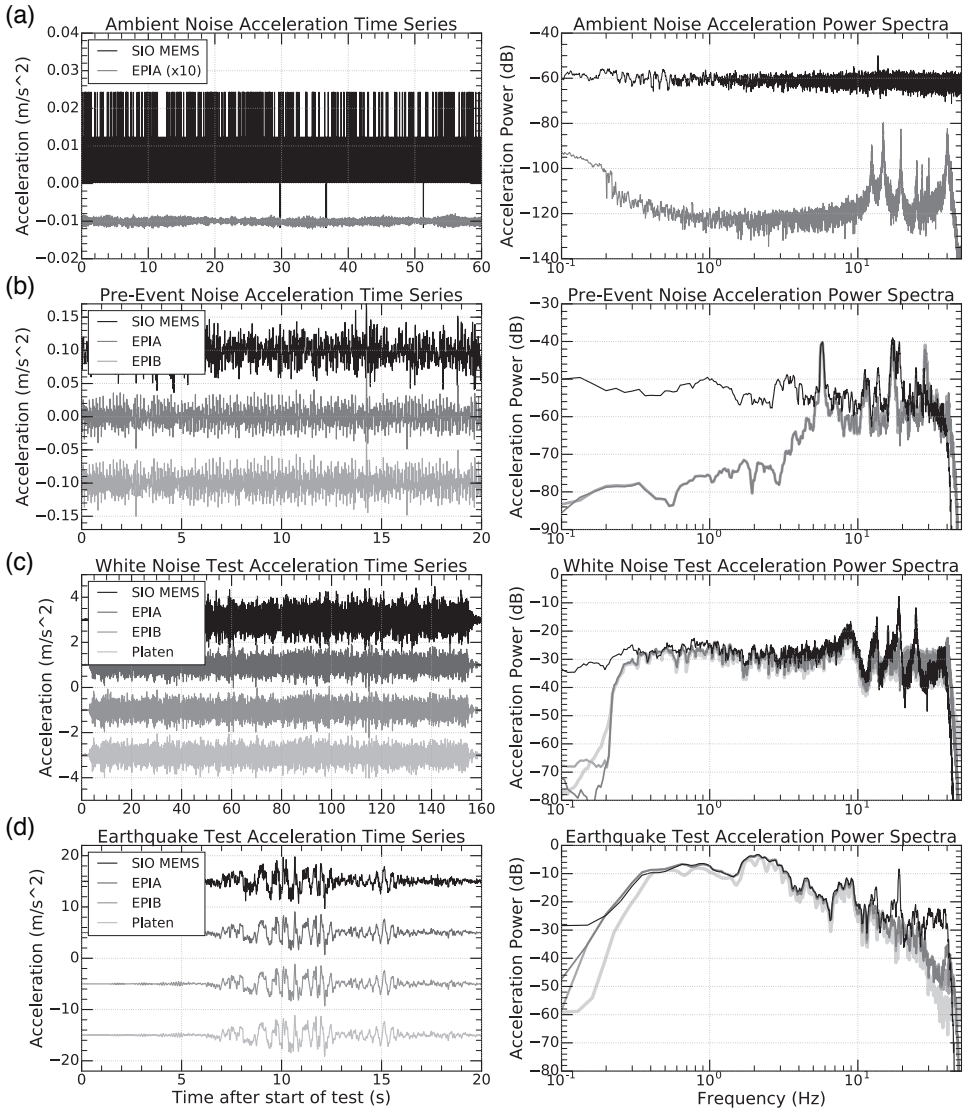

Figure 4.3: Foundation accelerometer comparison in the east component in both the time domain (left column) and frequency domain (right column). Acceleration time series are offset for comparison purposes, and corresponding power spectra for these accelerations are shown in decibels relative to 1 $(m/s^2)^2$/Hz. **(a)** Ambient noise comparison between the SIO MEMS and EPIA, the EpiSensor installed next to the GNSS/SIO MEMS on the foundation extension beam. The amplitude of the EpiSensor acceleration was multiplied by a factor of 10. The LHPOST was not in operation during this time. **(b)** Example pre-event noise for the SIO MEMS, EPIA, and EPIB. EPIB was the EpiSensor installed on the LHPOST foundation next to the extension beam. The LHPOST equipment was powered on during this time, but no test was in progress. **(c)** Example white noise test (Test 36) for the SIO MEMS, EPIA, EPIB, and the measured platen acceleration. **(d)** Example earthquake simulation test (Test 37, a Berkeley DBE simulation) for the SIO MEMS, EPIA, EPIB, and the measured platen acceleration.

example acceleration time series (left) and power spectra (right) for the collocated foundation instruments during the four types of motion experienced by the instruments: ambient noise (when the LHPOST was not in operation), the pre-event noise (when the LHPOST instrumentation was powered on, but no test was in progress), white noise tests, and earthquake simulation tests.

First, we compare the acceleration spectra of 10 minutes of ambient noise to verify the sensitivity of the SIO MEMS (Figure 4.3a). The EpiSensor is sensitive enough to measure the small vibrations in the foundation extension beam while the LHPOST was not in operation. The SIO MEMS ambient instrument noise is flat at -60 dB, too high to measure the motions recorded by the EpiSensor. This corresponds to less than 1 bit resolution. Figure 4.3(b) compares example pre-event noise. The vibrations due to operation of the LHPOST are large enough to reflect similar power amplitudes in all three foundation accelerometers at frequencies above 5 Hz. However, this still corresponds to less than 1 bit resolution for the SIO MEMS. The variances of the pre-event accelerations contribute to the assigned weighting of each instrument in the calculation of the seismogeodetic combination. Since the pre-event variance reflects a resolution lower than the sensitivity of the SIO MEMS, this variance estimate will not appropriately weight its data in the seismogeodetic combination in the case of large-amplitude dynamic motion. Thus, it is necessary to apply a multiplier to the pre-event variance. This is described in greater detail in the next section.

Figures 4.3(c) and 4.3(d) compare east-component accelerations for an example white noise test (Test 36) and an example earthquake simulation test (Test 37), respectively, for all three foundation sensors as well as the motion recorded by the shake table platen accelerometer. The shake table input control motion is modified to account for resonances and nonlinearities incurred during operation of the LHPOST, and the platen accelerometer verifies that the resulting shaking corresponds to the desired earthquake record (Conte et al., 2004). The SIO MEMS measures accelerations comparable to the EpiSensors above 0.25 Hz, the lower limit of the LHPOST shaking frequency typically used in testing. As expected given the high sensitivity of

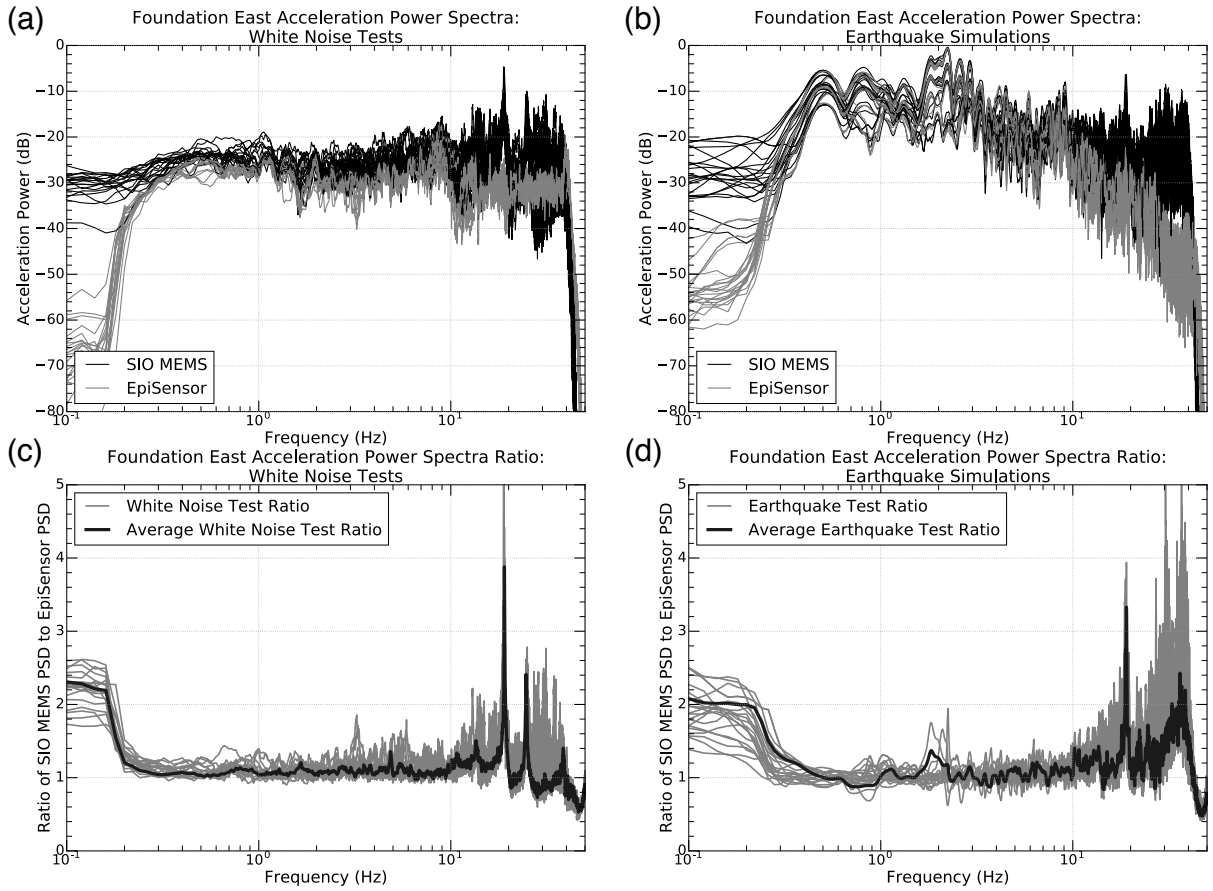

Figure 4.4: SIO MEMS and EpiSensor Foundation East component acceleration power spectra for all white noise tests **(a)** and earthquake tests **(b)** as listed in Table 2. Ratios of the SIO MEMS and EpiSensor acceleration power spectra ratios for **(c)** the white noise tests and **(d)** the earthquake simulations, with the average ratio plotted on top of the individual ratios. Power is shown in decibels relative to 1 $(m/s^2)^2$/Hz.

the observatory-grade accelerometers, the acceleration observations of both EpiSensors mounted on the building foundation are very similar to the shake table platen accelerometer in the band from 0.25 to 25 Hz. The platen motion recorded by the EpiSensor instruments was used as a ground-truth since its response is well understood by the seismological community. In the remaining comparisons, we use whichever foundation EpiSensor accelerometer was operating at the time of the test.

Next, we examine the ratio of SIO MEMS power spectra to EpiSensor power spectra using the east component of the foundation. We compile all of the power spectra for the white

noise tests in Figure 4.4(a). Figure 4.4(b) shows each of the spectra for the earthquake simulation tests. The ratio between the SIO MEMS spectra and EpiSensor spectra are shown in Figure 4.4(c), illustrating the differences between the spectra of the two sensors. We distinguish between the white noise tests and earthquake simulations to investigate changes in instrument response with increasing shaking intensity. The earthquake simulations also resulted in greater rotations than the white noise tests. For both types of tests, the SIO MEMS power spectra agree with those of the EpiSensor from 0.25 Hz to just above 10 Hz. This frequency range covers that of interest to structural monitoring of low to mid-rise buildings, as structural modes of interest in building monitoring are typically 5 Hz and below (Fleischman et al., 2015). This frequency range also extends higher than the range required for seismological source inversions, our primary applications in earthquake rapid response. The SIO MEMS has resonances of unknown origin at 18 and 24 Hz, along with a systematically higher noise level from $\sim$10 Hz to 30 Hz when compared with the collocated EpiSensor. The EpiSensor accurately captures the fall off in power for the earthquake spectra, whereas the SIO MEMS noise level remains relatively constant, leading to higher spectra ratios, but this is above the frequency range of interest. The power spectra comparison suggests that the SIO MEMS accelerations should be lowpass filtered to a frequency of 10 Hz before use in the seismogeodetic combination.

The Kinemetrics EpiSensor accelerometer is inarguably the superior instrument over the MEMS accelerometer in the SIO GAPs. However, we are interested in the feasibility of the SIO GAP as an affordable option for upgrading field GPS stations to seismogeodetic stations for earthquake early warning applications. As the SIO GAP compares well to the observatory-grade EpiSensor in the large-magnitude earthquake simulations at the LHPOST for frequencies up to 10 Hz, the SIO GAP qualifies as a suitable alternative for early warning purposes.

4.3.3 Optimization of the Seismogeodetic Solutions

For optimal performance, the Kalman filter seismogeodetic combination requires assignment of realistic weights to the accelerations and GPS displacements in order to better correct the integrated displacement waveform when a GPS displacement observation is present in the time series. In Bock et al. (2011), the weights are determined from the pre-event variances of each data type, such that a noisy instrument will have less effect on the combination dataset. To account for baseline offsets incurred in the accelerometer data during strong motion, a multiplier is applied to the acceleration pre-event variance to downweight the acceleration data in the combination. The short-term precision of high-rate (1-50 Hz) GPS displacement measurements is well understood (Genrich & Bock, 2006). We have characterized the acceleration pre-event variances in the preceding section. Here we investigate how to assign an acceleration variance multiplier that accurately reflects the reliability and performance of the accelerometer used in the seismogeodetic combination.

The importance of the choice of acceleration multiplier is demonstrated in Figure 4.5, in which we compare seismogeodetic displacement solutions for an exponential range of acceleration variance multiplier values (10^0, 10^1, 10^2, and 10^3). We will use these comparisons to choose variance multiplier values for the two types of accelerometers. Then, we will directly compare the SIO GAP seismogeodetic solutions to the observatory-grade seismogeodetic solutions using the chosen variance multipliers.

Our comparisons use the 12 earthquake simulation tests with high-quality foundation east component GPS RTD-estimated displacements (listed in Table 4.2). The GPS displacements were computed in real time using relative positioning to a close reference station. It is necessary to make the GPS weights in the seismogeodetic combination comparable to those in the field for both network and precise point positioning approaches in order to determine the best weights for the acceleration data. To weight the GPS RTD displacements correctly, we multiply the GPS pre-event variance by a factor of 10.4, which accounts for additional noise expected in field GPS

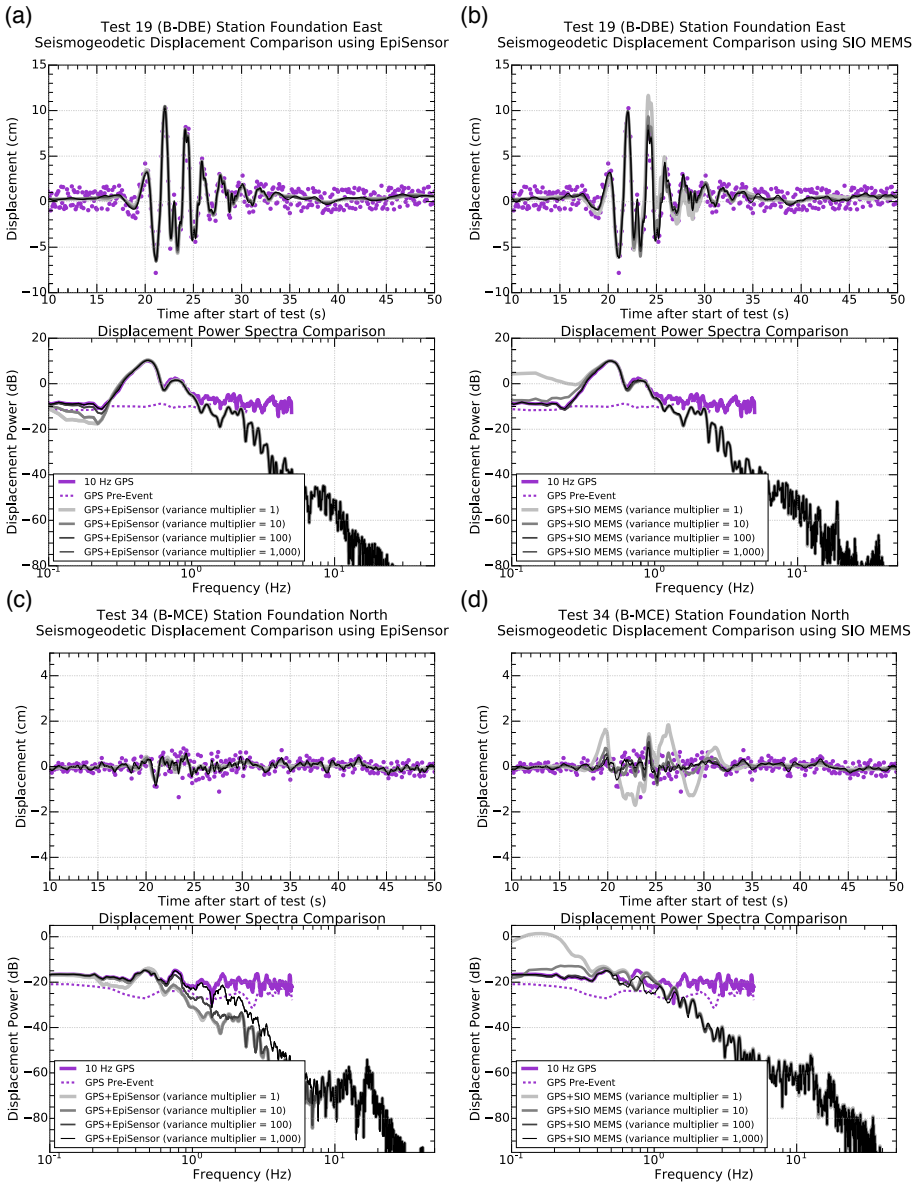

Figure 4.5: Example seismogeodetic displacements time series and corresponding power spectra using different acceleration pre-event variance multiplier values ranging exponentially from 10^0 to 10^3 for two LHPOST earthquake simulations: Test 19 (Berkeley DBE) east component using **(a)** EpiSensor and **(b)** SIO MEMS in the seismogeodetic combination; and Test 34 (Berkeley MCE) north component using **(c)** EpiSensor and **(d)** SIO MEMS in the seismogeodetic combination. The seismogeodetic displacements are compared to the GPS-only solutions. Pre-event GPS noise spectra are shown by the dashed lines. Displacement power spectra are in decibels relative to 1 cm_2/Hz. Smaller variance multiplier values correspond to greater weighting towards the acceleration solutions in the Kalman filter, while larger variance multiplier values correspond to a greater weighting towards the GPS solutions in the Kalman filter. Low-frequency differences in the seismogeodetic combination using SIO MEMS (b and d) indicate that multiplier values of 10^2 and greater are required to minimize the impact of errors in the SIO MEMS accelerations in the seismogeodetic combination.

observations caused by the ionosphere correction (Genrich & Bock, 1992). In the seismogeodetic combination, the pre-event variances are computed from 15 seconds of data recorded prior to the beginning of each test.

Figure 4.5(a,c) demonstrate how different choices of acceleration variance multiplier affect the observatory-grade seismogeodetic combination. All of the choices in variance multiplier values for the EpiSensor accelerometer produce seismogeodetic displacements that match above 0.25 Hz during large amplitude shaking (Figure 5a). This is similar to the result in Bock et al. (2011). Figure 4.5c shows that too large of an acceleration variance multiplier (in this case, 10^3) in the observatory-grade combination yields a seismogeodetic solution matching the high frequency spectra of the GPS observations which is understood to be random noise in the GPS solutions (Genrich & Bock, 2006). We suggest that a variance multiplier of 10^0 (no variance multiplier, weighting based solely on pre-event variance) is the most appropriate for the EpiSensor accelerometers because these seismogeodetic solutions minimize the noise in the pre- and post-event displacements where no motion is occurring. For the SIO GAP seismogeodetic combination, too low of an acceleration variance multiplier can put too much weight on the acceleration data, causing overly large displacement amplitudes during motion because the Kalman filter does not remove all of the baseline drift or other effects on low frequencies in the SIO MEMS data (Figure 4.5b,d). Thus, we suggest that a variance multiplier of 10^2 is the most appropriate for the SIO MEMS acceleration, as it produces seismogeodetic displacements where the displacement power spectra below 0.5 Hz are consistent with the GPS spectra.

Next, we quantify the results of our choice in acceleration variance multipliers of 10^0 and 10^2 for the EpiSensor and SIO MEMS data, respectively. We compute seismogeodetic solutions using these variance multipliers for both the collocated foundation instruments as well as the collocated rooftop instruments to test the SIO MEMS given the increased uncertainty due to extreme rotations. We compute the root mean square (RMS) differences between the two types of seismogeodetic solutions, and we also compare the values of peak displacement, velocity, and

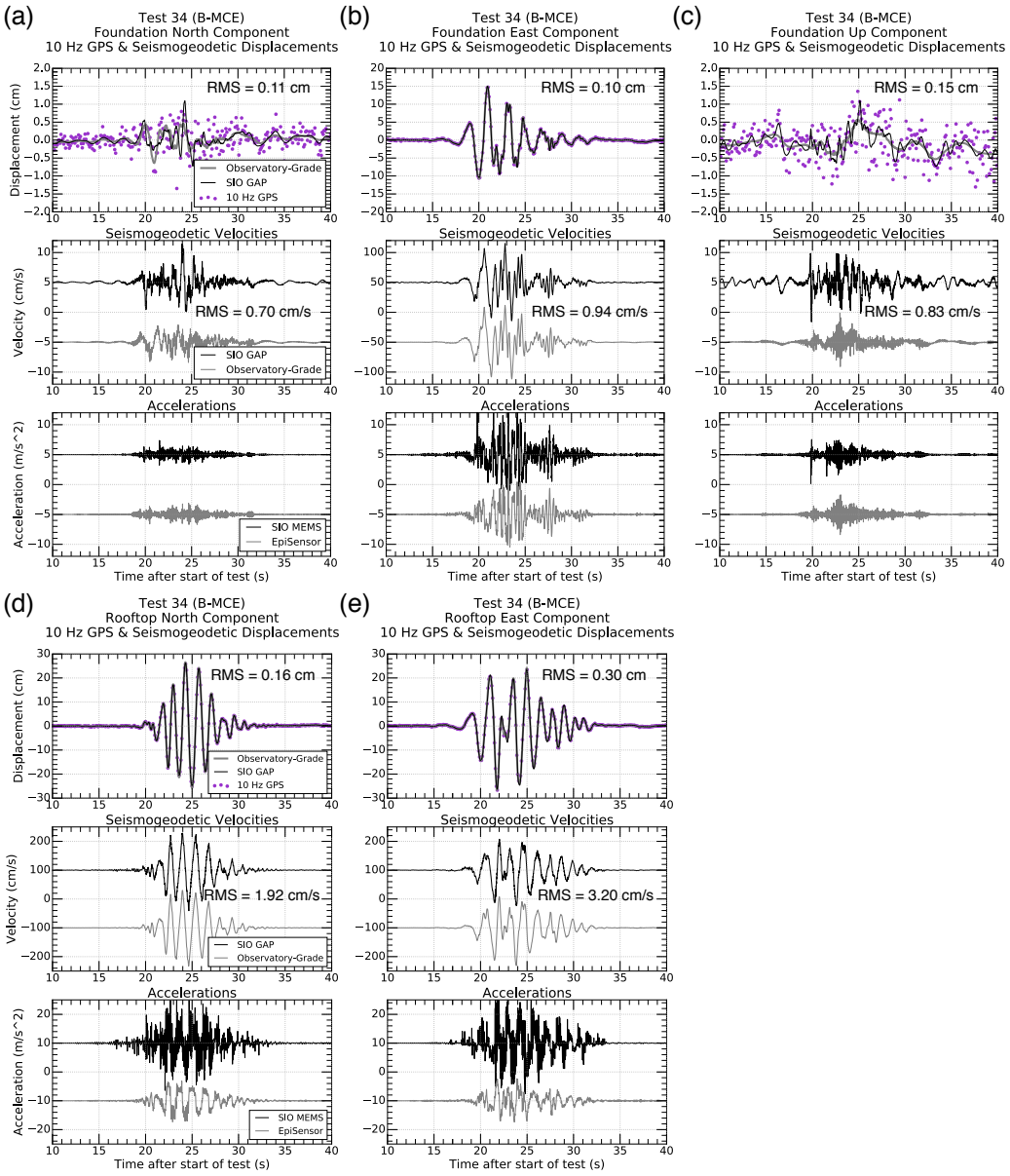

Figure 4.6: **(a-c)** Comparison of foundation seismogeodetic solutions using observatory-grade data and the SIO MEMS data with acceleration variance multipliers of 1 and 100, respectively, for Berkeley MCE Test 34. **(d-e)** Comparison of rooftop seismogeodetic solutions for the same earthquake simulation. The up component of the SIO MEMS was not functioning properly, so this component is excluded from this comparison. RMS differences between the SIO GAP and observatory-grade seismogeodetic solutions are also shown.

acceleration. An example set of seismogeodetic solutions for earthquake simulation test 34 (a Berkeley MCE ground motion) with high-quality foundation GPS in all three components, as well as the corresponding rooftop solutions, is shown in Figure 4.6. The rooftop MEMS accelerometer up component was not functioning properly during the LHPOST experiment, so this component is excluded from comparison. In Figure 4.7, the spectral power shown is higher above 10 Hz in the rooftop MEMS acceleration data compared to the MEMS on the foundation. The higher noise is likely in part caused by the response of the concrete pillar on which the rooftop GPS antenna/MEMS accelerometer instruments were mounted. This implies that some care should be taken when considering the mounting of the sensors in the field, although such high frequencies are of little importance for the earthquake early warning application. The SIO GAP was designed specifically to attach to the central, vertical member of stable Plate Boundary Observatory GPS stations, which are typically braced monuments with five legs, a design which avoids potential resonances that would be present in a single column. Different mount configurations could be tested in future opportunities for collocated experiments at the LHPOST. There are some interesting difference in the rooftop spectra at 1-2 Hz that are likely due to different responses to rotation between the two accelerometers under the extreme rotations due to the asymmetric structure. These, however, would not be present in a normal field deployment.

For example earthquake simulation test 34 (Figure 4.6), the SIO MEMS is able to produce seismogeodetic displacements that are within an RMS of 0.3 cm when compared to the seismogeodetic displacements calculated with the EpiSensor, and with a difference in the maximum displacement of 0.5 cm in the foundation north component. While the RMS differences in the seismogeodetic velocities are higher, Figure 4.4 indicates that this is due to the overall higher noise level of the SIO MEMS above 10 Hz. This implies that the SIO MEMS data should be lowpass filtered at 10 Hz prior to input in the seismogeodetic combination.

The means and standard deviations of the RMS differences, as well as the mean differences in the peak displacements, peak velocities, and peak accelerations, for each component with

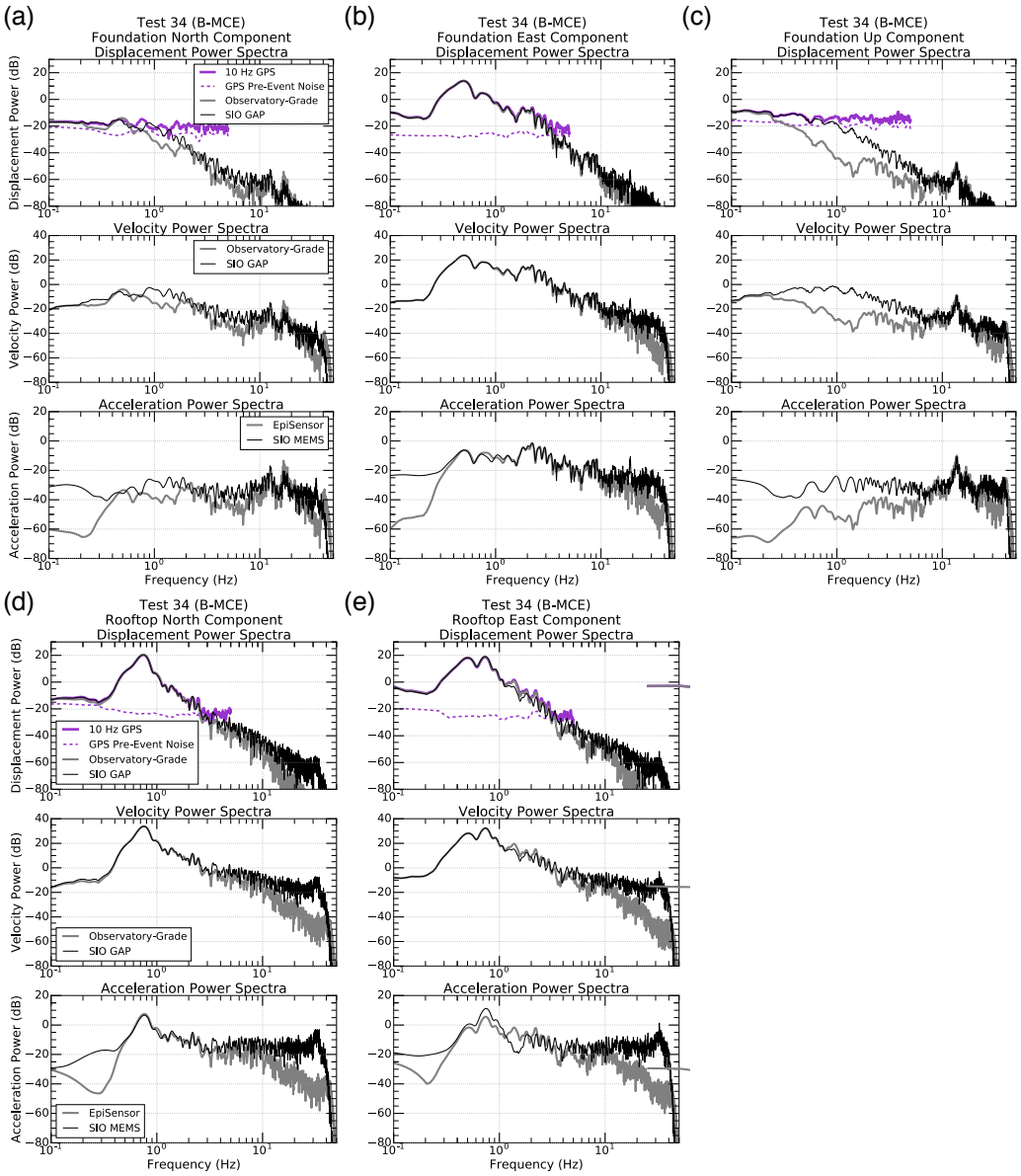

Figure 4.7: **(a-c)** Power spectra comparison of foundation seismogeodetic solutions shown in Figure 6. **(d-e)** Power spectra comparison of the rooftop seismogeodetic solutions for the same earthquake simulation. The power spectra for the GPS pre-event noise are shown by the dashed lines. Displacement power is shown in decibels relative to 1 cm^2/Hz, velocity power is shown in decibels relative to 1 $(cm/s)^2$/Hz, and acceleration power is shown in decibels relative to 1 $(m/s^2)^2$/Hz.

Table 4.3: Comparison between SIO GAP and observatory-grade seismogeodetic solutions using earthquake simulation tests for components with significant shaking. (PGD, peak ground displacement; PGV, peak ground velocity; SIO, Scripps Institution of Oceanography; RMS, root mean square; GAP, Geodetic Module and low-cost MEMS Accelerometer Package.)

	Foundation East Component	Roof East Component	Roof North Component
Displacement RMS difference (cm)	0.14 ± 0.09	0.50 ± 0.29	0.11 ± 0.05
Velocity RMS difference (cm/s)	1.0 ± 0.5	6.0 ± 3.1	1.4 ± 0.6
PGD difference (cm)	0.01 ± 0.42	0.61 ± 1.27	-0.12 ± 0.30
PGV difference (cm/s)	2.1 ± 1.9	-4.9 ± 12.4	1.4 ± 3.1
PGA difference (m/s^2)	2.0 ± 0.8	5.2 ± 2.3	4.5 ± 2.4

significant shaking are shown in Table 4.3, for all earthquake simulation tests with good quality GPS observations. While the differences in peak displacements are small during significant shaking above the noise level of the GPS, Figure 4.6(a) suggests that these differences are more significant for small-amplitude shaking. Because of the high frequency noise in the SIO MEMS, these seismogeodetic solutions cannot reliably capture the very high frequencies necessary for measuring PGA and PGV values, for example, that go into the USGS ShakeMap (Wald et al., 1999) for rapid response. Table 4.4 shows the same comparisons as Table 4.3 but with the MEMS accelerometer data lowpass filtered to 10 Hz prior to the seismogeodetic combination. While the average RMS differences in the seismogeodetic displacements and velocities are similar to the unfiltered comparison, the maximum 10 Hz filtered acceleration and velocity values are much closer to the observatory-grade values. Future upgrades to a MEMS sensor with improved high-frequency characteristics would add this desirable capability.

The seismogeodetic displacements using the SIO GAP instruments are nearly identical to seismogeodetic solutions using observatory-grade accelerations when calculated using the appropriate variance multipliers for large-amplitude shaking in the frequency band from 0 to 10 Hz. The SIO GAP seismogeodetic velocities match the observatory-grade seismogeodetic velocities below 10 Hz, but they contain a larger amount of high-frequency noise from the accelerometer above 10 Hz, which can be filtered out. These comparisons were made using earthquake simulations based on the M_w6.6 Imperial Valley and M_w6.9 Loma Prieta earthquakes,

Table 4.4: Comparison between SIO GAP (low-pass filtered to 10 Hz) and observatory-grade seismogeodetic solutions using earthquake simulation tests for components with significant shaking. (PGD, peak ground displacement; PGV, peak ground velocity; SIO, Scripps Institution of Oceanography; RMS, root mean square; GAP, Geodetic Module and low-cost MEMS Accelerometer Package.)

	Foundation East Component	Roof East Component	Roof North Component
Displacement RMS difference (cm)	0.21 ± 0.13	0.88 ± 0.50	0.18 ± 0.11
Velocity RMS difference (cm/s)	1.0 ± 0.5	8.6 ± 3.3	1.2 ± 0.5
PGD difference (cm)	-0.07 ± 0.38	2.0 ± 2.6	-0.10 ± 0.38
PGV difference (cm/s)	0.9 ± 1.9	-0.3 ± 18.4	-0.4 ± 3.6
PGA difference (m/s^2)	-0.08 ± 0.3	-0.2 ± 2.1	-0.24 ± 0.62

large events that are well within the magnitudes of interest to early warning.

4.4 Sensitivity of the Field GAPs in the Current Seismogeodetic Networks

Four $\sim$M4 earthquakes have occurred within the current seismogeodetic networks in southern California and the San Francisco Bay Area that were recorded by SIO GAPs in the field (Figure 4.8). Two events occurred within the southern California network in the Salton Trough near the cities of Obsidian Butte (M4.2) and Westmorland (M4.1) and were recorded by the two stations closest to the epicenters (Figure 4.8a). Two additional M4.0 events occurred in the San Francisco Bay Area in the cities of Fremont and Piedmont. The Fremont event was located south of the network and was recorded by only one station (Figure 4.8b), and the Piedmont event was located well within the network and was recorded by five stations (Figure 4.8c). These events allow for the assessment of the lower detection limits of seismogeodesy using the SIO GAPs in real-world conditions.

For each of these events, we lowpass filtered the SIO MEMS acceleration data to 10 Hz as suggested by the direct comparison with the observatory-grade accelerometers in the NEES@UCSD LHPOST experiment. We first examine the SIO MEMS acceleration wavefoRMS, choosing the Piedmont earthquake for our example, since it was observed at the most stations.

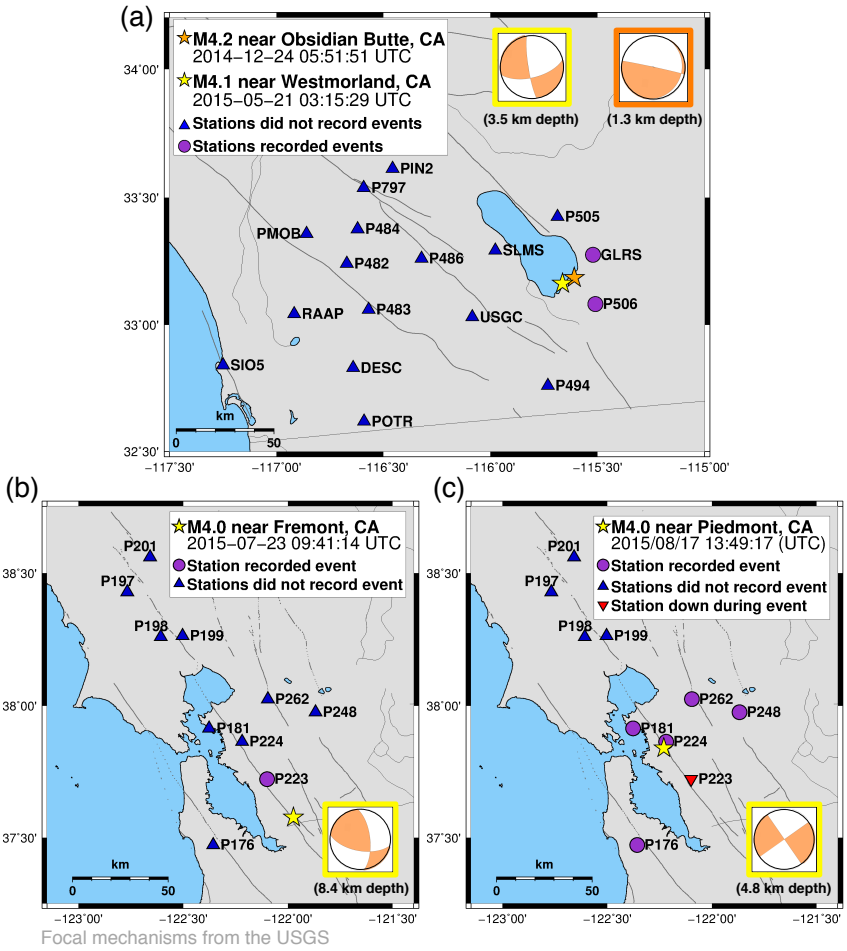

Figure 4.8: The four ∼M4 earthquakes used to determine the sensitivity of the SIO GAP seismogeodetic combination in the field for the purposes of earthquake early warning: **(a)** A M4.2 earthquake near Obsidian Butte, CA, and a M4.1 earthquake near Westmorland, CA; **(b)** a M4.0 earthquake in Fremont, CA; and **(c)** a M4.0 earthquake in Piedmont, CA. The stars indicate the epicenter locations of each event. The focal mechanisms for each earthquake are also shown. The triangles and circles show the locations of the stations in the current seismogeodetic networks, where the circles indicate stations where the SIO GAP's MEMS accelerometers detected the earthquakes.

The wave arrivals at the five seismogeodetic stations that recorded shaking are shown in Figure 4.9. The SIO MEMS recorded the P-wave arrival up to ∼24 km away from the epicenter and the S-wave arrival up to ∼42 km away from the epicenter. This demonstrates that the SIO GAP will be able to distinguish the P-wave within tens of kilometers for a magnitude 4 or above earthquake. Therefore, these instruments will be able to distinguish the P-wave in the near field

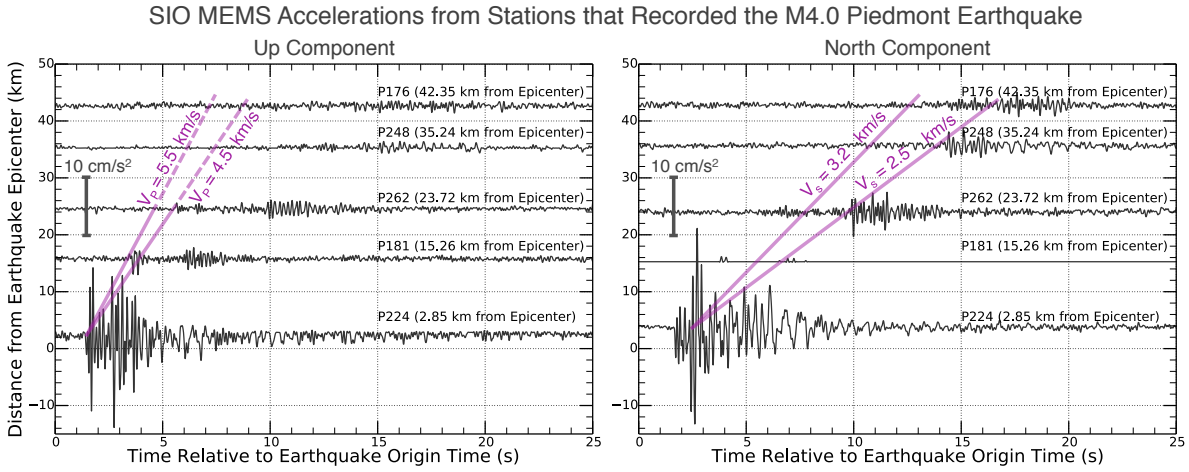

Figure 4.9: Accelerations for all seismogeodetic stations that recorded motion from the M4.0 Piedmont earthquake offset by epicentral distance. Left: Up component accelerations; Right: North component accelerations. East component accelerations have similar amplitudes to the north component and are not shown. Windows of appropriate P- and S-wave arrival times are also shown, indicating that the SIO GAP is sensitive enough to record the P-wave up to ∼24 km away from the epicenter and the S-wave up to ∼42 km away from the epicenter for this small earthquake. The north component of station P181 was not functioning properly during the time of the earthquake.

for all earthquakes of interest to early warning.

Next, we examine the SIO GAP seismogeodetic solutions for these M4 earthquakes. We compute 1 Hz GPS position observations for the Salton Trough events and 5 Hz GPS positions for the Bay Area events using PPP-AR (Geng et al., 2013). Unfortunately, data transmission problems during the events caused the SOPAC regional PPP service to miss the events in real time, so we compute the positions after-the-fact using a regional satellite clock solution using the network described in Geng et al. (2013) and IGS final orbits. We then compute the seismogeodetic solutions after-the-fact using the previously determined weighting scheme in the same loosely-coupled Kalman filter with backwards smoothing used in the LHPOST experiment. For comparison purposes only, we include in Figures 4.10-4.13 displacements and velocities obtained by integrating the acceleration data and highpass filtering the resulting wavefoRMS at 0.25 Hz to remove baseline drift. The integrated accelerations allow us to visually

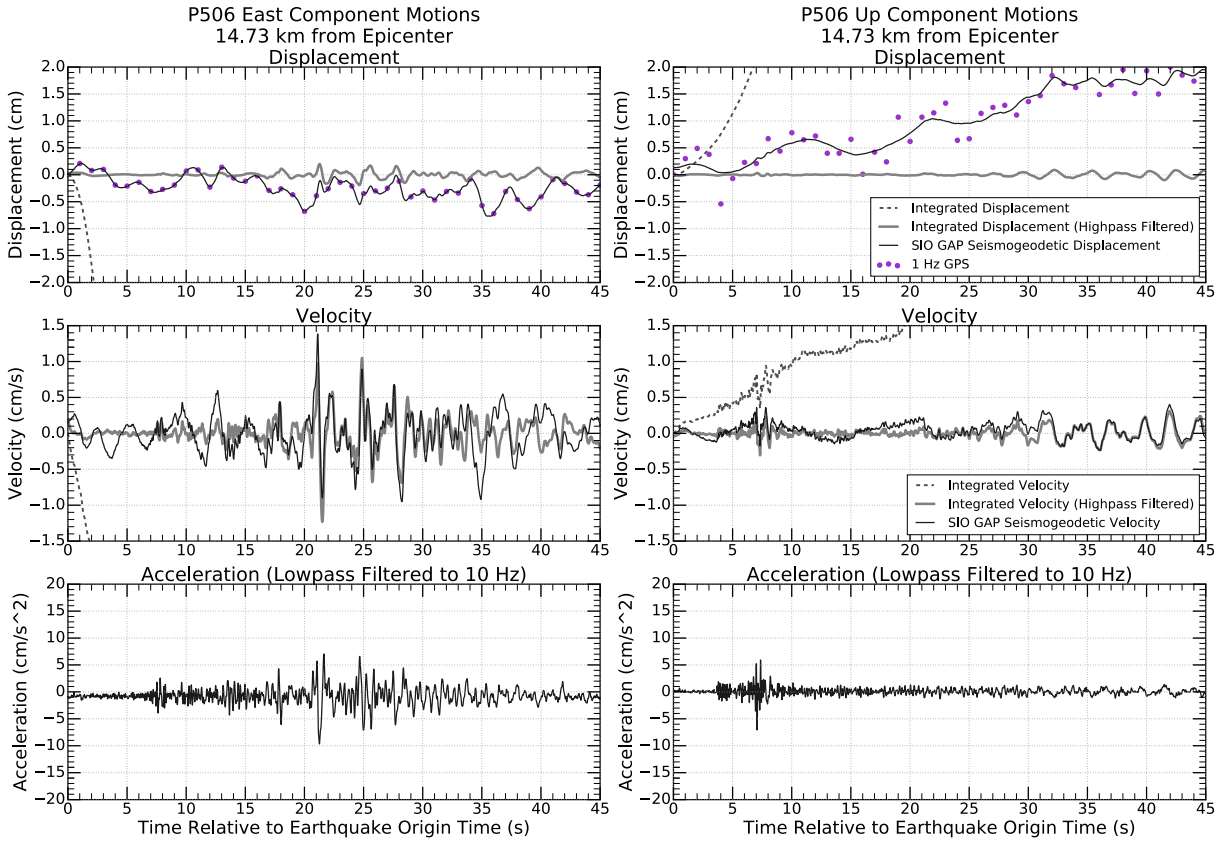

Figure 4.10: Example horizontal component (left) and up component (right) wavefoRMS for the December 2014 M4.2 Obsidian Butte earthquake for one of the stations that recorded the shaking. Top row: 1 Hz GPS displacement observations with seismogeodetic displacement and displacements integrated from acceleration (both unfiltered and highpass filtered to 0.25 Hz to remove baseline drift); Middle row: seismogeodetic velocity and velocities integrated from acceleration (with and without highpass filtering); Bottom row: acceleration lowpass filtered to 10 Hz

distinguish the high-frequency contributions of the SIO GAP accelerations to the seismogeodetic solutions.

The example wavefoRMS from the two Salton Trough earthquakes are shown in Figures 4.10 and 4.11. Most apparent in the GPS-only solutions are the long period variations ($>$ 5 s) on the order of 0.5 cm amplitude in the horizontal and 1.5 cm amplitude in the vertical that are clearly not seismic ground motions from a small event. This low level of long period variation is typical of high quality GPS solutions for field sites i.e., (Geng et al., 2013), and is also seen in

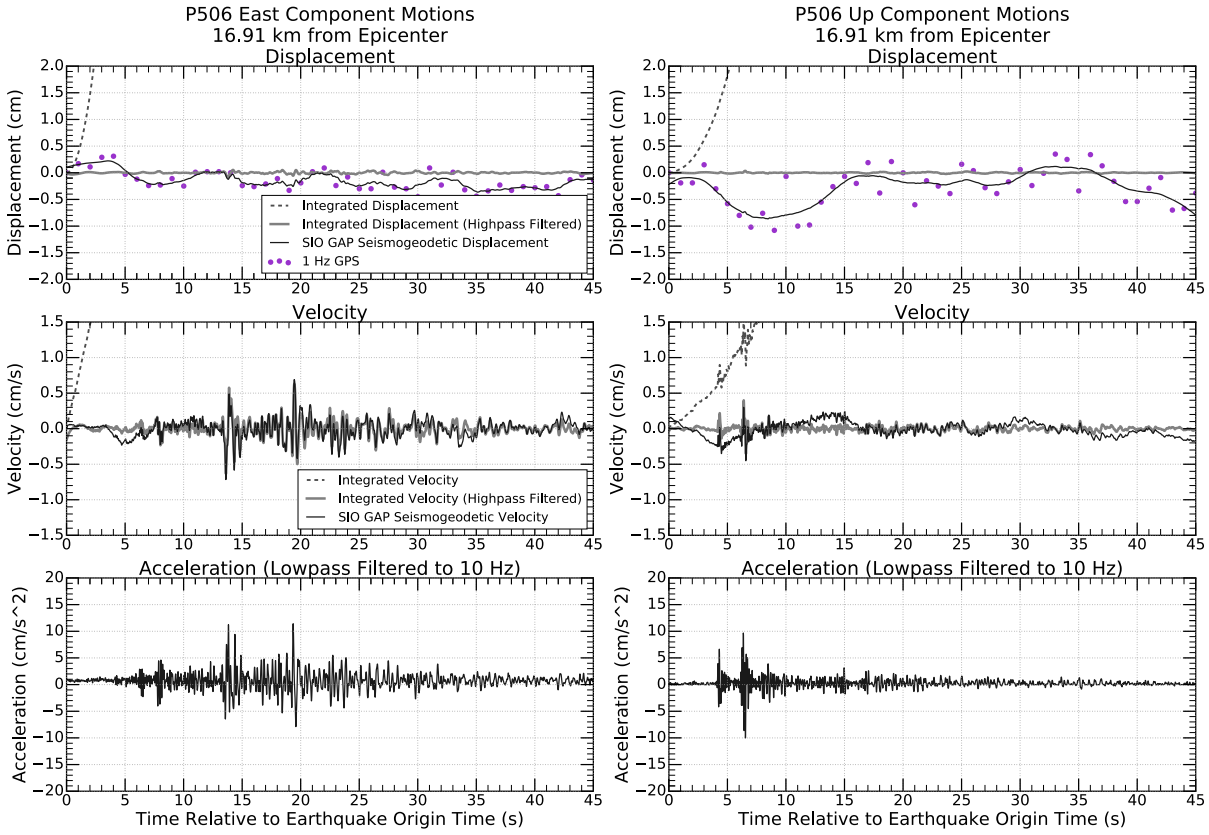

Figure 4.11: Example horizontal component (left) and up component (right) wavefoRMS for the May 2015 Westmorland earthquake for the same seismogeodetic station as Figure 10. Top row: 1 Hz GPS displacement observations with seismogeodetic displacement and displacements integrated from acceleration (both unfiltered and highpass filtered to 0.25 Hz to remove baseline drift); Middle row: seismogeodetic velocity and velocities integrated from acceleration (with and without highpass filtering); Bottom row: acceleration lowpass filtered to 10 Hz.

the LHPOST experiment GPS positions if similarly processed (Figure 4.2). The seismogeodetic solution does not eliminate this long period background noise.

As expected for these small earthquakes, the displacements at local distances (10s of km) are too small to be seen in the position observations alone. The SIO GAP seismogeodetic combinations produced stable solutions with no appreciable offset and no integration artifacts from baseline drift for both earthquakes.

While the velocity records showed ground motion indicative of a seismic event, the displacements did not exhibit significant variations. This null result provided definite evidence

that the event had not developed into a large rupture with significant displacements, an important datum for whether to issue a warning of an earthquake of consequence. While the integrated acceleration wavefoRMS in Figures 4.10-4.13 highlight the motion captured by the SIO GAP accelerometers above 1 Hz frequency, the seismogeodetic solution is the preferred dataset because the underlying methodology and resulting displacement error level is the same for the range of seismic frequencies from the static offset to 10 Hz and over the entire range of possible ground motion amplitudes without need to adapt the analysis method for the largest earthquakes. For small earthquakes with insignificant displacement, the seismogeodetic displacements are within the GPS noise level. The integrated acceleration records that include baseline offset errors produced unphysical wavefoRMS with drifts that increased without bound (Figure 4.10-4.13). For large events (>M6), the seismogeodetic displacements maintain the coseismic offsets once the dynamic motion passes, an inherent difficulty for displacement wavefoRMS derived from acceleration only, particularly in real-time situations (Bock et al., 2011; Melgar, Bock et al., 2013).

Figures 4.12 and 4.13 show the example wavefoRMS for the two Bay Area earthquakes. The 5 Hz position observations exhibit comparable scatter compared to the 1 Hz position observations. As expected, the SIO GAP seismogeodetic displacements show significant reduction in this scatter. Using the 5 Hz position observations yield no apparent reduction in the long-period noise in the seismogeodetic combination compared to using the 1 Hz positions. The lower limits of seismogeodesy using the SIO GAPs are therefore the amplitudes of these long-period fluctuations.

4.5 Discussion

Taking into account the results from these four ∼M4 earthquakes, we suggest that the SIO GAP seismogeodetic solutions have a long period noise limit around 0.8 cm in the horizontal and 2.5 cm in the vertical. These limits are governed by the GPS observations in the seismogeodetic

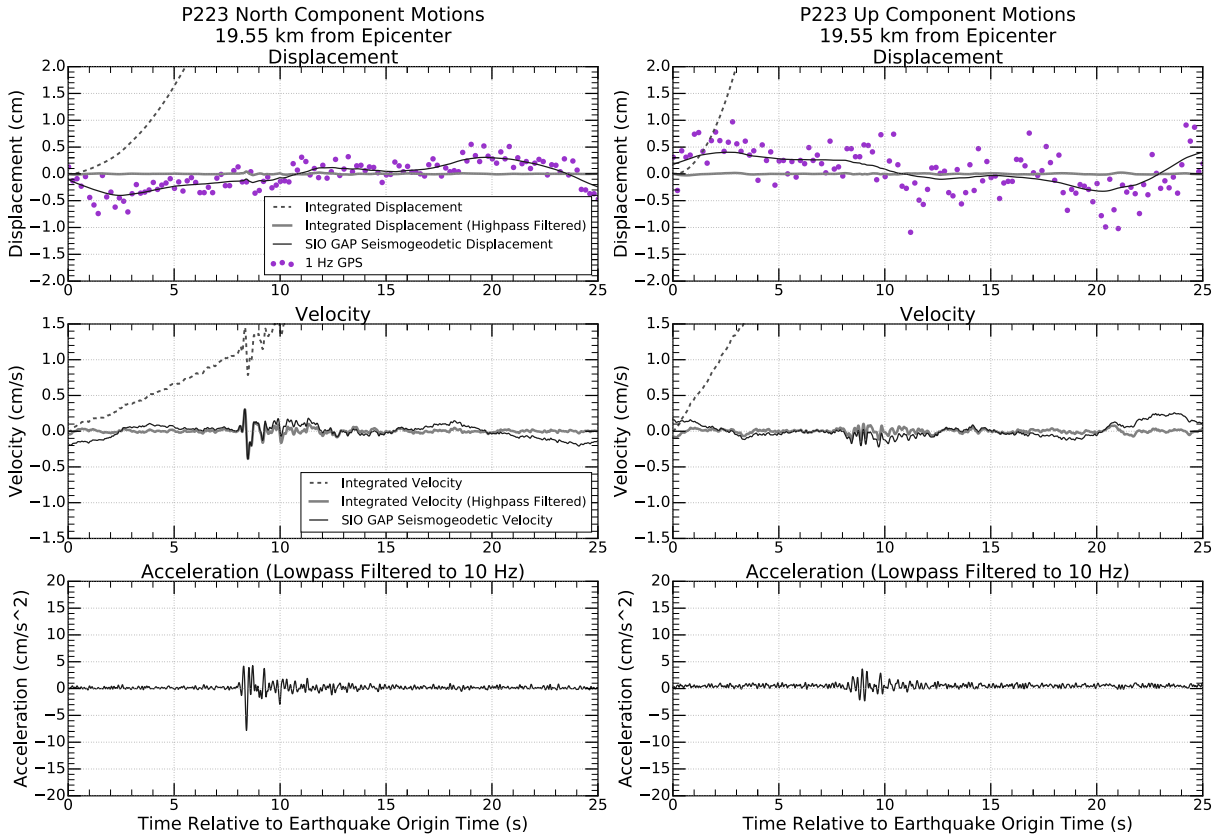

Figure 4.12: Example horizontal component (left) and up component (right) wavefoRMS for the July 2015 M4.0 Fremont earthquake for the seismogeodetic station that recorded the shaking. Top row: 1 Hz GPS displacement observations with seismogeodetic displacement and displacements integrated from acceleration (both unfiltered and highpass filtered to 0.25 Hz to remove baseline drift); Middle row: seismogeodetic velocity and velocities integrated from acceleration (with and without highpass filtering); Bottom row: acceleration lowpass filtered to 10 Hz.

combination and are lower than the noise of GPS-only solutions of around 1.5 cm in the horizontal and 5 cm in the vertical (Genrich & Bock, 2006). Thus, using a more sensitive observatory-grade accelerometer will not improve upon the seismogeodetic displacement accuracy achievable with the SIO GAPs for small events. This, in combination with the ability of the SIO GAP to record the P-wave for earthquakes of magnitude $\geq$4, demonstrates that employing a MEMS accelerometer is sufficient for seismogeodetic upgrades of GPS stations.

The reduction of random scatter in the seismogeodetic displacements compared to GPS

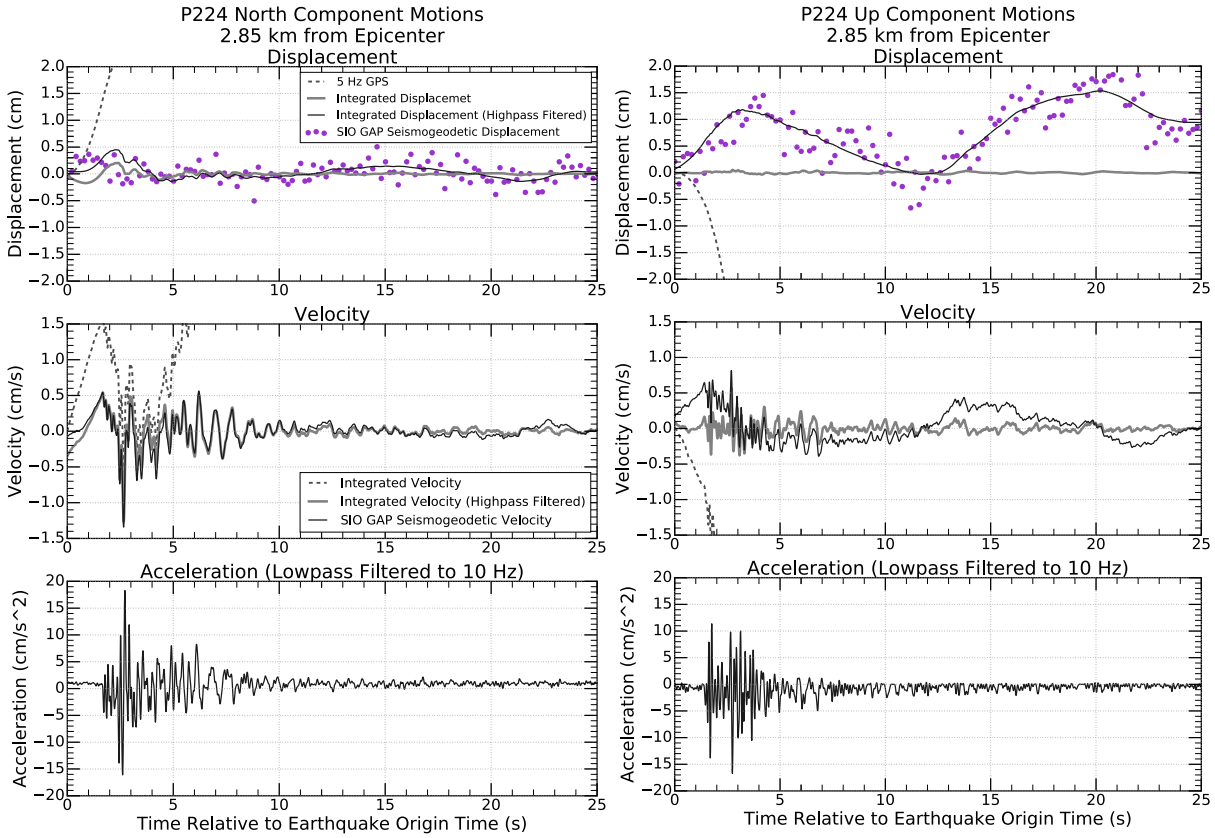

Figure 4.13: Example horizontal component (left) and up component (right) wavefoRMS for the August 2015 M4.0 Piedmont earthquake for the seismogeodetic station closest to the epicenter. Top row: 1 Hz GPS displacement observations with seismogeodetic displacement and displacements integrated from acceleration (both unfiltered and highpass filtered to 0.25 Hz to remove baseline drift); Middle row: seismogeodetic velocity and velocities integrated from acceleration (with and without highpass filtering); Bottom row: acceleration lowpass filtered to 10 Hz.

observations alone increases the accuracy of near-field seismic displacements as shown in Table 4.5. RMS differences between the GPS observations and observatory-grade seismogeodetic displacements retain the errors due to the long period, temporally correlated noise that ultimately limits the use of seismogeodetic solutions for small earthquakes. When seismogeodetic displacements are used as inputs in earthquake early warning and rapid response products, we anticipate that the more accurate displacements will improve solutions for line-source centroid moment tensor solutions and finite fault inversions (Melgar, Crowell et al., 2013) as well as near-shore

Table 4.5: RMS difference between observatory-grade seismogeodetic solutions (filtered and decimated to 10 Hz) and GPS observations for the LHPOST earthquake simulation tests for components with significant shaking.

	RMS Difference (cm)
Foundation east component	0.27 ± 0.21
Roof east component	0.18 ± 0.08
Roof north component	0.18 ± 0.09

rapid tsunami inundation models (Melgar & Bock, 2015). Although GPS observations alone may be sufficient for local tsunami warning if enough real-time stations are available in the near-field region, the seismogeodetic observations provide improved resolution of the earthquake source in static and kinematic inversions (Melgar & Bock, 2015).

Magnitude scaling relationships have been developed based on the peak ground displacement (PGD) before ground shaking has ended (Melgar et al., 2015) and P-wave displacement (P_d) calculated in the first 5 s of the waveform using both GPS-only and observatory-grade seismogeodetic displacements (Crowell et al., 2013). While both types of displacement wavefoRMS will be able to record the PGD for the largest magnitude earthquakes at regional hypocentral distances, the heightened sensitivity of the seismogeodetic displacements increases the hypocentral distance ranges that can be used for PGD scaling for intermediate events of interest to earthquake early warning.

While GPS-only positions are suitable for PGD scaling for the largest earthquakes, the data are not accurate enough to distinguish the P-wave arrival. In contrast, Geng et al. (2013) showed that for a M5.4 earthquake at 30 km (with 8.4 km hypocentral depth), the seismogeodetic combination with observatory-grade accelerometers could distinguish the P-wave arrival. The small $\sim$M4 earthquake example from Piedmont, CA illustrates that the SIO MEMS accelerometers are capable of capturing the P-wave arrival at distances less than 24 km from the earthquake epicenter and thus are not the limiting factor in applying the seismogeodetic method for P_d observations of larger earthquakes. While a practical lower limit for this magnitude calculation

has yet to be determined, the low-cost deployment of these sensors greatly increases the probability of having a nearby seismogeodetic recording of the earthquake, therefore decreasing the time between earthquake onset and issuance of an early warning.

It should be stressed that the seismogeodetic combination provides an improvement only when seismic shaking is occurring and measured by the accelerometer. There is no additional information during periods of quiescence that would enhance, say, the epoch-by-epoch GPS positioning.

It is possible that the long-period fluctuations in the GPS positions could be improved by reducing the multipath error using sidereal filtering techniques that remove the repeating pattern of displacement error (Choi et al., 2004). The reduction of the long-period fluctuations, which can typically decrease noise by about 12% at a high-quality geodetic site (Choi et al., 2004), may improve the sensitivity of the seismogeodetic solutions. These improvements may be helpful for determining magnitude using the P_d magnitude-scaling relationships and improving static offset estimates for small events. Spectral analysis of high-rate (1-50 Hz) GPS position time series indicate that high frequency errors (up to several seconds) are uncorrelated from epoch to epoch, but that low frequency errors due to multipath are temporally correlated up to several minutes (Genrich & Bock, 2006). At intermediate frequencies, it remains to be determined whether the increase in sensitivity outweighs the increased complexity of applying sidereal filtering in a real-time environment.

A few instances of lost data due to problems with the SIO MEMS sensors occurred at both the field stations and the stations installed at the LHPOST. Problems encountered with the Kionix KXR94-2353 sensor included: switching sample points of the east and up sensor components, time periods of reduced sensitivity of an individual component, increased high frequency noise levels at high amplitudes of acceleration, and clipping of values at intermediate acceleration levels. The data used here were screened for such problems and only reliably recorded ground motions were analyzed. Therefore, we cannot recommend the use of this particular model (KXR94-2353)

of MEMS accelerometer for earthquake early warning applications. With the advancement of technology, low-cost accelerometers are continually improving in quality. The next generation SIO GAP will include an improved MEMS accelerometer with 16-bit resolution. The Geodetic Module will also feature onsite precise point positioning that will enable analysis and transmission of higher-rate ($>$ 5 Hz) GPS displacements with lower bandwidth requirements than streaming more verbose raw GPS and accelerometer data to a central server.

4.6 Conclusions

The SIO GAPs, consisting of a MEMS accelerometer and Geodetic Module, were developed to upgrade existing real-time GPS monitoring stations for the purposes of using seismogeodesy for earthquake early warning and rapid earthquake characterization. Already, 27 SIO GAPs have been installed at established GPS monitoring stations in southern California and the San Francisco Bay Area. We first tested the performance of the SIO MEMS accelerometers against observatory-grade Kinemetrics EpiSensor accelerometers in an experiment on the NEES@UCSD Large High-Performance Outdoor Shake Table. These experiments allowed us to determine the accuracy of the low-cost MEMS accelerometer and resulting seismogeodetic solutions during strong shaking and demonstrate similar results from relative positioning techniques compared to the PPP techniques used in field conditions. Direct comparison between the accelerometers from 0.25 to 25 Hz shows that the SIO GAPs accurately record acceleration in frequency ranges of primary interest for earthquake early warning up to 10 Hz. Despite possible resonances at 18 and 24 Hz, and an overall higher noise level above 10 Hz in the MEMS accelerations, seismogeodetic displacements and velocities were in good agreement with those calculated using the observatory-grade data when appropriate Kalman filter weights were applied to account for MEMS acceleration noise levels.

Although we have not had the opportunity to observe a significant earthquake with the 27

SIO GAPs in the field, since their deployment they have recorded four magnitude 4 earthquakes in the Salton trough and the San Francisco Bay Area. We have shown that the seismogeodetic velocity wavefoRMS are sensitive enough to record P-wave arrivals in the near field of these four earthquakes, thus demonstrating the utility of the MEMS sensors for earthquake early warning based on P-wave metrics. We demonstrated that the seismogeodetic displacements are more precise than their GPS-only counterparts during strong ground motion, and also that the absence of permanent motion or significant horizontal displacements above the background noise level of 0.8 cm provides an extra datum to reduce false alaRMS in earthquake early warning. We conclude that seismogeodetic observations using MEMS accelerometers at collocated GPS stations, within regional monitoring networks such as those in Japan and the Western U.S., are suitable for early warning systems for any earthquake of significance without saturation at the highest magnitudes. Furthermore, the additional information provided by combining the geodetic and seismic data allows for improved imaging of the seismic source (Melgar & Bock, 2015). This study supports efforts to continue upgrading existing GPS stations to seismogeodetic capability with low-cost MEMS accelerometers and/or deployment of GPS at existing seismic stations with observatory-grade accelerometers.

4.7 Acknowledgements

This work is published in **Saunders, J.K., Goldberg, D.E., Haase, J.S., Bock, Y., Offield, D.G., Melgar, D., Restrepo, J., Fleischman, R.B., Nema, A., Geng, J., Walls, C., Mann, D., and Mattioli, G.S., 2016, "Seismogeodesy using GPS and low-cost MEMS accelerometers: Perspectives for earthquake early warning and rapid response,"** ***Bulletin of the Seismological Society of America*****, 106(6), 2469-2489. https://doi.org/10.1785/0120160062**. The dissertation author was the primary investigator and author of this paper.

We thank an anonymous reviewer for insightful comments. We thank Robert Clayton

and Ellen Yu at California Institute of Technology for archiving the MEMS accelerometer data at the Southern California Earthquake Data Center. We thank Frank Vernon for the loan of the Kinemetrics EpiSensors and data recorders and Peng Fang, Melinda Squibb, and Anne Sullivan at the Scripps Orbit and Permanent Array Center (SOPAC) for their contributions to this research. Data, engineering and data archiving services were provided by the EarthScope Plate Boundary Observatory operated by UNAVCO, and supported by the National Science Foundation (No. EAR-0732947 and EAR-1261833 for the GAGE Facility). We gratefully acknowledge funding support from the National Aeronautics and Space Administration grants Earth Science Technology Office, Advanced Information Systems Technology/NNX12AH55G, ROSES Earth Science Applications: Disasters/NNX14AT33G and ROSES Earth Surface and Interior/NNX14AQ53G; the National Science Foundation grants EarthScope/EAR-1252186, Instrumentation and Facilities/ EAR-1252187, NSF NEESR Grant CMMI-1135033; NSF Rapid Award CMMI-1208729 and the George E. Brown Jr. NSF Award CMMI-0429389; the Southern California Earthquake Center, University of Southern California NSF and USGS subaward Y865564.

The data used in this paper from the experiment at the NEES@UCSD LHPOST are available at ftp://garner.ucsd.edu/pub/projects/Shaketable/2013/SIO_MEMS_Analysis/. The data for the four earthquakes are available atftp://garner.ucsd.edu/pub/projects/Earthquakes/. Power spectra calculations were performed using the Nitime module for Python found in nipy.org/nitime/ (last accessed September 2015). The seismogeodetic data were generated using the Kalman filter software written by Melgar and Bock in Python. A Matlab version of the code (used inBock et al.,2011) can be found athttps://github.com/dmelgarm/Kalman. Python versions of the software modules are available upon request.

Chapter 5

Seismogeodetic building monitoring and synthetic induced earthquake scenarios for a 12-story structure in Oklahoma

In the previous chapter, seismogeodetic observations from collocated GNSS sensors and strong-motion accelerometers were demonstrated to provide broadband displacement information about the motion of buildings during strong shaking using a shake table experiment. This chapter provides an example of applying seismogeodetic instrumentation to record in-situ building motion in a region experiencing high rates of seismicity.

5.1 Abstract

Oklahoma has been experiencing an increase in seismicity due to wastewater injection related to oil and natural gas production. As many buildings in Oklahoma were constructed before this increase, it is imperative to determine the response of these building to significant ground motion. We use a combination of strong-motion accelerometers and a rooftop GNSS

sensor to monitor a 12-story aging reinforced concrete building at Oklahoma State University (OSU), located within the region of induced seismicity. The seismogeodetic method combines the GNSS and accelerometer data in a Kalman filter and provides a broadband view of the shaking, particularly the low-frequency motion and static offset information necessary for determining damage. Between September 2017 and September 2018, we have recorded shaking from ten M4+ earthquakes.

In a preliminary data assessment, we determine the building resonances to be 1.3 and 2.2 Hz in the north-south direction and 2.5 Hz in the east-west direction, which is consistent with the structure's rectangular shape and orientation. We use this information to evaluate a preliminary finite element model of the structure which will simulate the response of the building to ground motions from larger earthquakes. These ground motions will be synthesized using kinematic rupture scenarios of M_w6 earthquakes on the Lake Carl Blackwell Fault, the mapped fault closest to the study site that has high hazard due to its favorable orientation with the regional stress state. We discuss our approach to creating the kinematic rupture models and compare synthetic waveforms of the 2016 $M_w5.8$ Pawnee, Oklahoma, earthquake with regional observations.

5.2 Introduction

In 2008, Oklahoma began experiencing a dramatic increase in M3.5+ earthquakes (Ellsworth et al., 2015), with four M5+ earthquakes occurring since 2011 (Yeck et al., 2017). This unprecedented increase in seismicity in this region has been attributed to an increase in wastewater injection from oil and gas production (Rubenstein & Mahani, 2015). Near the wastewater injection well, changes in pore pressure can trigger earthquakes to occur on pre-existing faults. Further from the injection site, poroelastic stress changes dominate over pore pressure changes, and can trigger induced earthquakes up to nearly 35 km away from the injection well (Keranen et al., 2014). While modified regulations in wastewater disposal have now been implemented

because of this increased seismicity (Davis & Fisk, 2017; Stewart & Ingelson, 2017), numerical models of fluid diffusion for this region suggest that the current regulations may not be enough to prevent future M5+ earthquakes (Dempsey & Riffault, 2018). Seismicity has also been observed to occur years after injection ends (Ellsworth, 2013), further suggesting that Oklahoma continues to be a region of high seismic hazard (e.g., Petersen et al., 2018).

On September 3, 2016, the largest earthquake ever recorded in Oklahoma occurred. The M_w5.8 Pawnee earthquake caused damage to buildings near the epicenter, and prompted the governor to declare a state of emergency. Much of the damage observed included damage to unreinforced brick masonry and brick facades, as well as collapsed chimneys (Clayton et al., 2016). Many structures in Oklahoma are older conventional reinforced concrete (RC) systems or unreinforced masonry. Because of the low historic seismicity in the state, building codes were adopted later than other areas experiencing high seismic activity, so many existing structures do not comply with current standards. While the International Building Code has been in effect since 2000, retrofits are not required on buildings constructed prior to its implementation. Many of the aging buildings in Oklahoma were not originally designed to withstand the increase in seismic activity, so it is important to verify that models used to simulate building response are accurate for these kinds of structures as well as monitor these structures for signs of damage after an earthquake.

Two metrics used to detect building damage are permanent drift and changes in the fundamental period of the building. For taller structures, the fundamental period usually varies between 0.05 and 0.15 times the number of stories, depending on the flexibility of the building (Celebi, 2000). Strong-motion accelerometers are commonly used for building monitoring to characterize the spectral response, however they cannot be used to observe permanent offsets as the integrated acceleration data are subject to baseline drift at very long periods (Boore, 2011; Boore & Bommer, 2005). Automatic baseline correction methods that use objective methods have been shown to produce significant errors in the static offset estimate and in displacement waveforms

up to frequencies of 0.5 Hz (Emore et al., 2007; Melgar et al., 2013). Global Navigation Satellite System (GNSS) sensors have the advantage of measuring displacement directly, and are sensitive to low frequency motions and permanent displacements. Using a method that simultaneously solves for the acceleration baseline offsets and the integrated displacements, Emore et al. (2007) found that collocated GNSS observations with as low as 30 s sampling rates are sufficient for constraining the integrated accelerometer data and recovering displacement waveforms that include permanent offsets. Another approach is the *seismogeodetic combination*, which is a multi-rate Kalman filter to optimally combine accelerometer and high-rate GNSS data to produce broadband displacements and velocities (Smyth & Wu, 2007; Bock et al., 2011).

Saunders et al. (2016) demonstrated the value of the seismogeodetic combination for measuring the seismic response and permanent deformation simultaneously using an experiment on the Network for Earthquake Engineering Simulation (NEES) Large High-Performance Outdoor Shake Table (LHPOST). In this chapter, we use this technique to make in-situ measurements of building motion due to shaking from regional earthquakes. We instrument a building in Oklahoma with collocated GNSS and accelerometer instruments and observe the response of the building to shaking from events of M$\sim$4. These observations have helped to fine-tune a finite element model of the structure that simulates the building response to ground motions. We also discuss our approach to forming $\sim M_w 6$ kinematic rupture models for generating the synthetic acceleration time series used for input into the finite element simulations that will provide for investigations of the structural response to these larger events.

5.3 Instrument Deployment

Oklahoma State University (OSU) in Stillwater, Oklahoma, is a location that experiences shaking from M3.5+ earthquakes on a regular basis. Many of the buildings on campus consist of conventional RC structural systems or unreinforced masonry. The 2016 $M_w 5.8$ Pawnee earthquake

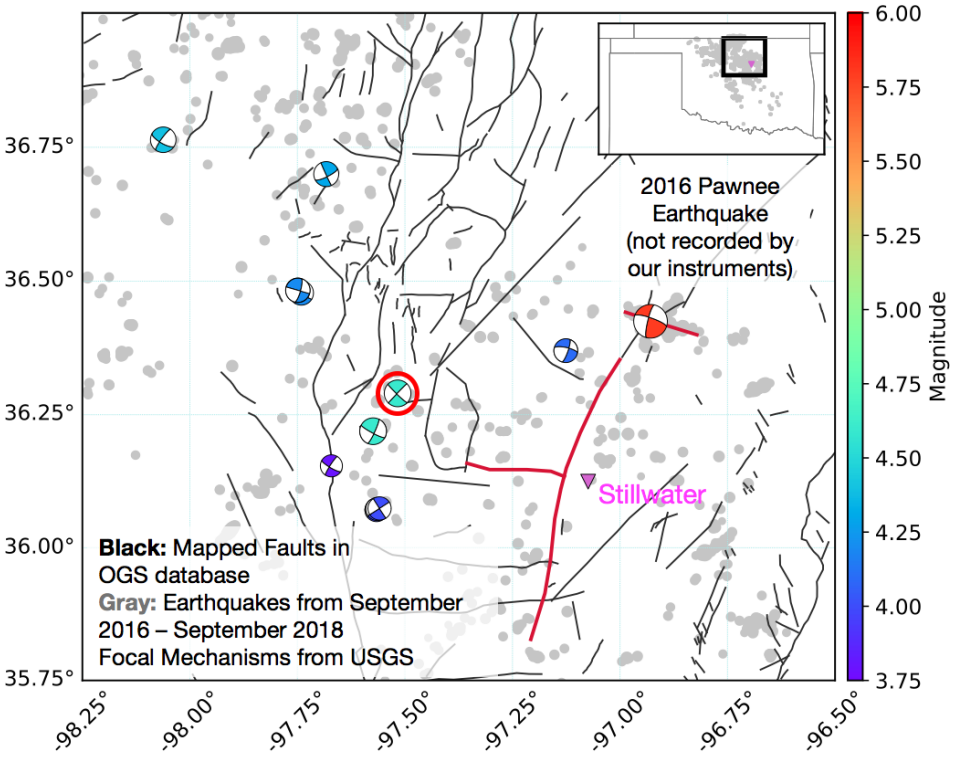

Figure 5.1: Mapped faults in Oklahoma with regional seismicity from September 2016 - September 2018 shown in the gray dots. Focal mechanisms from the 2016 M_w5.8 Pawnee earthquake and M4+ earthquakes occurring between September 2017 - September 2018 are shown, colored by magnitude. The Sooner Lake Fault, which ruptured during the 2016 Pawnee earthquake, is highlighted in red. Also highlighted in red are the Stillwater (N-S striking) and Lake Carl Blackwell (E-W striking) faults, the two mapped faults located closest to the Oklahoma State University structure we have instrumented (pink triangle). The M4.6 earthquake used in later figures is highlighted by the red circle.

occurred only 35 km away from the OSU campus, and the USGS Shake Map estimates that the campus experienced peak ground acceleration (PGA) values ranging between 0.12g and 0.15g. Several of the RC buildings on the campus were observed to have experienced damage such as cracking in walls.

The tallest structure on the OSU campus is Kerr-Drummond Hall, measuring twelve stories (Figure 5.2). It is an RC structural system consisting of RC columns and RC slabs on all stories. The ground floor has a conventional slab-beam construction, and the other floors were constructed as flat slabs with lightweight partitioning. It was built in 1965, prior to the

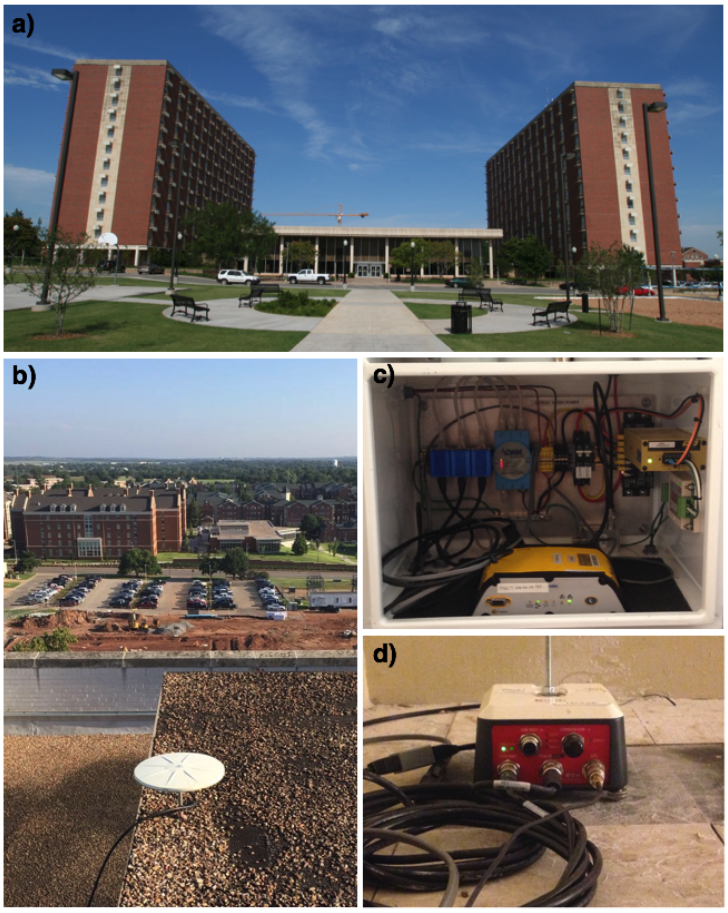

Figure 5.2: Photographs of Kerr-Drummond Hall and instruments used for building monitoring. **(a)** Kerr-Drummond Hall, facing the East-West direction. The Kerr building is located on the left. **(b)** GNSS antenna located on the roof of the Kerr building. **(c)** Trimble NET-RS GNSS receiver located inside the stairwell on the roof next to the strong-motion accelerometer. **(d)** Kinemetrics Etna-2 strong-motion accelerometer located in the rooftop stairwell. Another strong-motion accelerometer of the same make and model is installed in the basement of the building. Photo credit: **(a)** www.facebook.com/Kerr.Drummond, **(b-d)** Mohamed Soliman.

implementation of earthquake design and detailing provisions for RC structures, the first being in 1970 by the American Concrete Institute. This makes Kerr-Drummond Hall a representative example of an aging RC structure not originally designed to withstand seismic shaking but is now subject to much larger ground motions due to the dramatic increase in the number of felt earthquakes in recent years.

In July 2017, seismic and geodetic instruments were deployed at Kerr Hall to record the

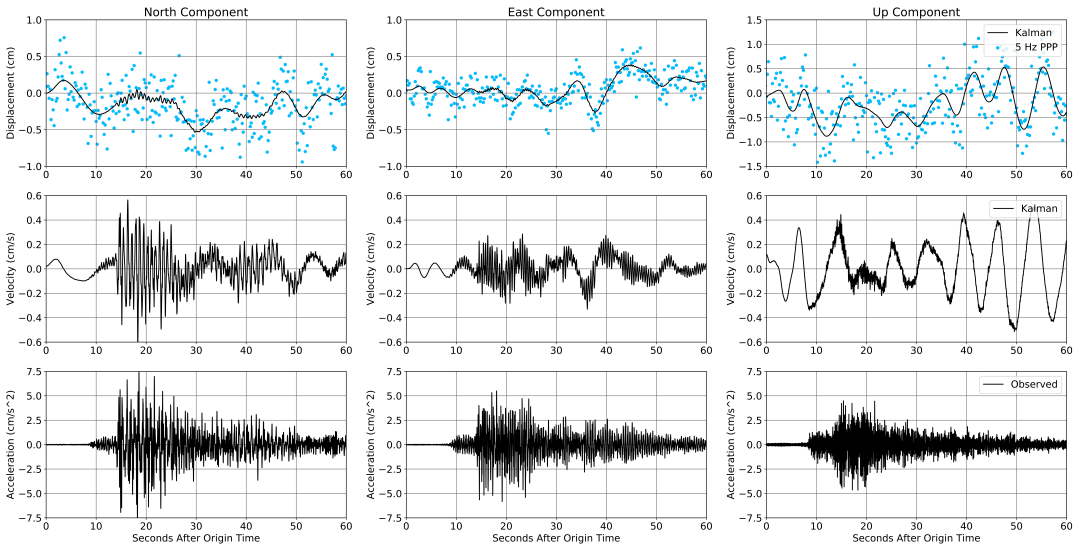

Figure 5.3: Rooftop displacement, velocity, and acceleration time series for an example M4.6 earthquake that occurred on April 7, 2018. The columns are, from left to right, the north, east, and up components, and the rows show, from top to bottom, the displacement, velocity, and acceleration time series for this earthquake. The 5 Hz GNSS displacements were processed using the PPP method. The black lines in the displacement and velocity subplots show the Kalman filtered solution of the combined GNSS and accelerometer data. The location of the earthquake relative to the building is highlighted in Figure 4.1.

building's response to shaking and to monitor the building for any signs of cumulative damage due to frequent shaking (Figure 5.2). Two Kinemetrics Etna-2 strong-motion accelerometers were installed in the building, one in the stairwell on the roof of the building and the other on the ground floor. One GNSS antenna with a Trimble NET-RS receiver was installed on the roof 3 m above the rooftop accelerometer. The accelerometers record at 100 Hz and the GNSS receiver records at 5 Hz. The GNSS data are processed into displacements using a kinematic precise point positioning approach with ambiguity resolution (Zumberge et al., 1997; Shi et al., 2008). In the following section, we describe analysis of the building response from earthquakes recorded by these instruments.

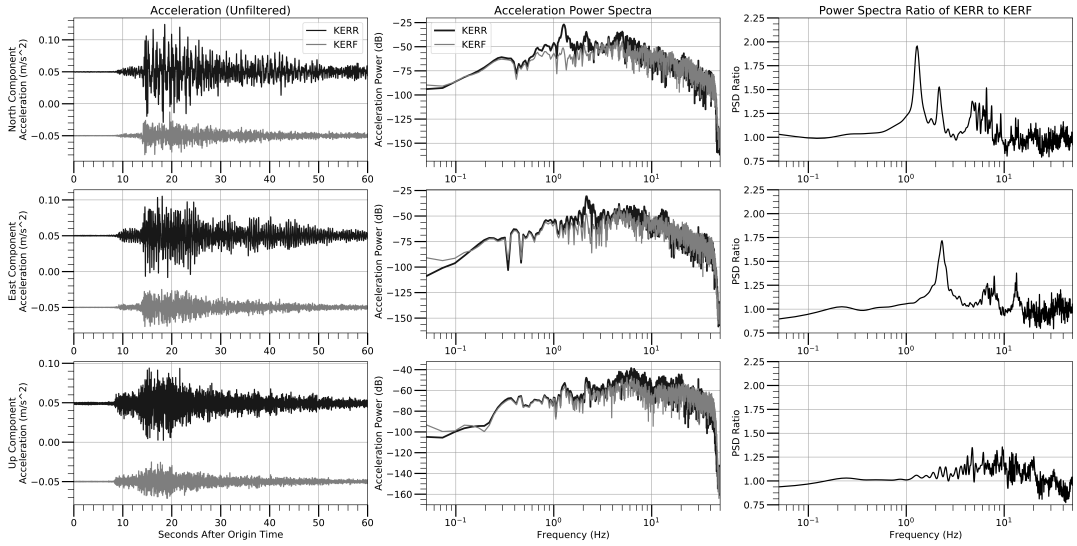

Figure 5.4: Power spectra comparison between the rooftop (KERR) and foundation (KERF) accelerometers for the same example M4.6 earthquake as the previous figure. The columns show, from left to right, the acceleration time series (where black is the rooftop acceleration and gray is the foundation acceleration), the acceleration power spectra, and the ratio of the rooftop to foundation power spectra. The rows are, from top to bottom, the north, east, and up components. The power spectra ratios show building resonances of 1.3 and 2.2 Hz in the north component and 2.5 Hz in the east component.

5.4 Observations of Building Motion from Regional M4+ Earthquakes

Between September 2017 and September 2018, the instruments installed on Kerr Hall recorded 10 M4.0-4.6 regional earthquakes in Oklahoma, shown by the focal mechanisms in Figure 5.1. Figure 5.3 shows the rooftop acceleration and GNSS displacement time series for a M4.6 earthquake that occurred on April 7, 2018. Also included in this figure are seismogeodetic displacement and velocity waveforms computed by combining the acceleration and GNSS displacements in a Kalman filter (Saunders et al., 2016). While the accelerometers are sensitive enough to record motion from this earthquake, the shaking is not above the GNSS noise level. The analysis demonstrates the sensitivity of the combined waveforms.

We compared the rooftop acceleration with the acceleration recorded on the foundation

for this earthquake (Figure 5.4), and calculated the spectral properties of the building response. A comparison of the acceleration time series for these two instruments shows, expectedly, that the shaking is amplified at the roof compared to the foundation with spectral peaks above 1 Hz. There are resonances in the north component at 1.3 Hz and 2.2 Hz, and in the east component there are resonances at 2.5 Hz. This is generally consistent with the shape and orientation of the building: the rectangular structure has the long axis oriented E-W, so the inferred stiffness would be greater in that direction, resulting in higher-frequency resonances than along the shorter axis. However, the frequencies are higher than expected given the height of the building (Çelebi, 2000).

When we examine the acceleration power spectra ratios for all 10 M4.0-4.6 earthquakes that we have recorded during this time period (Figure 5.5), we see that these resonance frequencies are consistent for the suite of earthquakes. The amplitude of the resonance depends on the station-hypocenter azimuth, where earthquakes with a more northerly back azimuth excite larger resonances in the north component compared to earthquakes that are located more to the west. This suggests a nonlinearity in the building response that is directionally dependent, even at these relatively small shaking amplitudes, that would be important to investigate further and consider when creating scenarios of larger earthquakes to use in dynamical models of the structure.

5.5 Comparison of Observed Building Motion with Simulated Motion

In our first year of monitoring, there have been no felt earthquakes with significant building motion observable above the noise level of the GNSS sensor. To determine how Kerr Hall will respond to strong ground motion, our colleagues at OSU are developing a finite element model (FEM) of the building. The preliminary FEM of Kerr Hall is an isolated model of the building frame, and contains no connections to Drummond Hall. The frame is composed of the weight-bearing elements of the building, where the load estimations and material properties

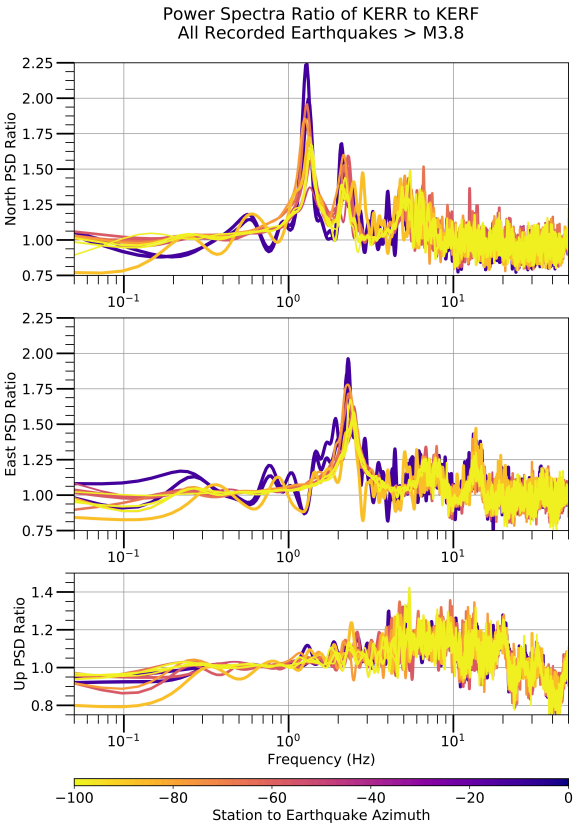

Figure 5.5: Rooftop (KERR) to foundation (KERF) acceleration power spectra ratios for all M4+ earthquakes that occurred between September 2017 - September 2018, colored by the station-hypocenter azimuth. The yellows indicate earthquakes that are located to the west of the building while purples indicate earthquakes located to the north of the building.

are as provided in the original structural drawings of the building (Omid Khandel, personal communication). Simulations are conducted using the SAP2000 software, where time series of horizontal accelerations at the base of the building are applied to the FEM and the acceleration at the roof is computed at the roof using direct integration time-history analysis (CSI, 2014). To verify that the preliminary FEM of Kerr Hall is correctly simulating the building response, we input foundation acceleration observations of the example M4.6 earthquake discussed in the previous section and compare the simulated rooftop accelerations with the observations.

Figure 5.6 shows the horizontal rooftop accelerations computed by the FEM simulation with the observed accelerations. The acceleration time series show that simulation is capturing

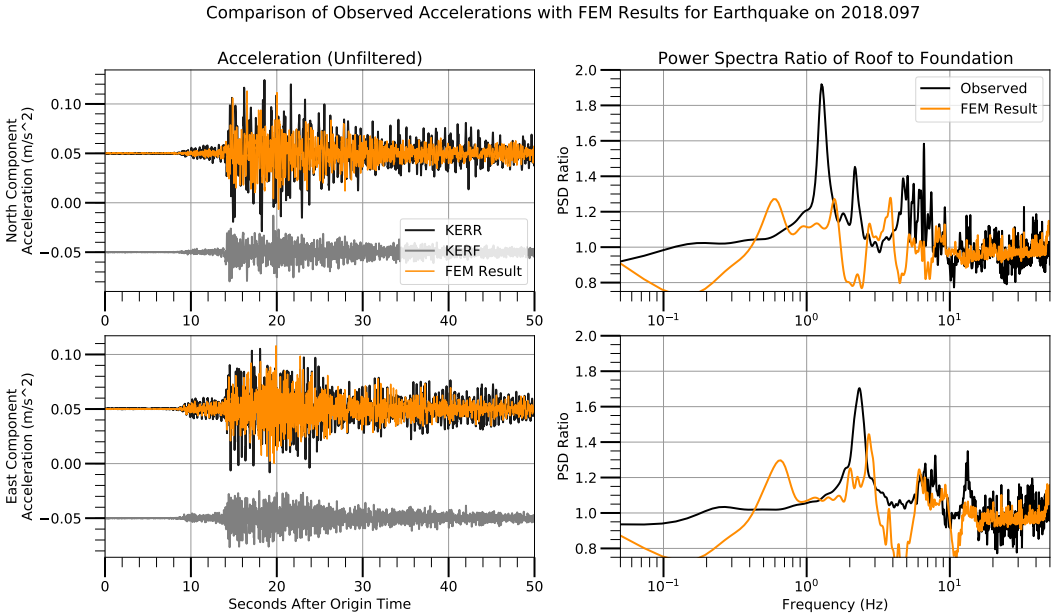

Figure 5.6: Comparison of observed accelerations with FEM simulation results for an example M4.6 earthquake in the horizontal components. The left column shows the unfiltered accelerations for the rooftop observations (KERR - black lines) and FEM simulation results (orange lines), where the gray lines show the foundation (KERF) acceleration time series input to the FEM simulation. The right column shows the power spectra ratios of the roof to the foundation for the observed (black) and FEM results (orange). The top row shows the comparison for the north component and the bottom row shows the comparison for the east component.

the general amplification of shaking on the roof compared to the foundation. However, when the acceleration power spectra ratios are compared, we see the FEM is simulating the building resonances at significantly lower frequencies than observed. This suggests that the weight-bearing elements of the structure are not the only contributors to the resonance frequencies. Increasing the complexity of the FEM by incorporating the external walls or the attachment to Drummond Hall may increase the stiffness of the building enable higher resonance frequencies for the FEM simulations. Further analysis and testing of these additions to the FEM are being conducted by our colleagues at OSU.

5.6 Synthetic Ground Motions from Kinematic Ruptures

To provide information for future engineering studies of the structural behavior under strong shaking from a large earthquake, we seek to provide realistic synthetic ground motions for near-field source scenarios. These will serve as input acceleration time series for a finite element model of the building to simulate the full nonlinear building response. There have been no large earthquakes that produced significant displacement at the roof of the building since the building was instrumented, and there where no strong-motion seismic instruments at the OSU campus during the 2016 M_w5.8 Pawnee earthquake. Synthetic kinematic rupture scenarios are the best option for producing region-specific ground motions for input to the finite element simulations. We will create kinematic rupture scenarios of M_w6 earthquakes on the Lake Carl Blackwell Fault, which is the closest fault to Stillwater, Oklahoma, that is oriented to the regional stress state in a way that favors slip (Walsh & Zoback, 2016). It also has surface expressions indicating possible recent activity (Jaiswal et al., 2017). In this section, we describe the modeling approach to the kinematic rupture scenarios and validate the synthetic waveforms using observations of the 2016 Pawnee earthquake at regional seismic stations (Figure 5.7).

5.6.1 Modeling Setup

We follow the methods of Melgar et al. (2016) and Graves and Pitarka (2010) to create semi-stochastic kinematic rupture models for the earthquake scenarios. A summary of the rupture generation process is described in Section 3.3 of this dissertation. The main differences between the approach described in that section and the approach here is that we assume right-lateral strike-slip motion which corresponds to the slip directions for induced earthquakes in this region. We allow 10° variation around a specified rake value. The background rupture speed v_r was

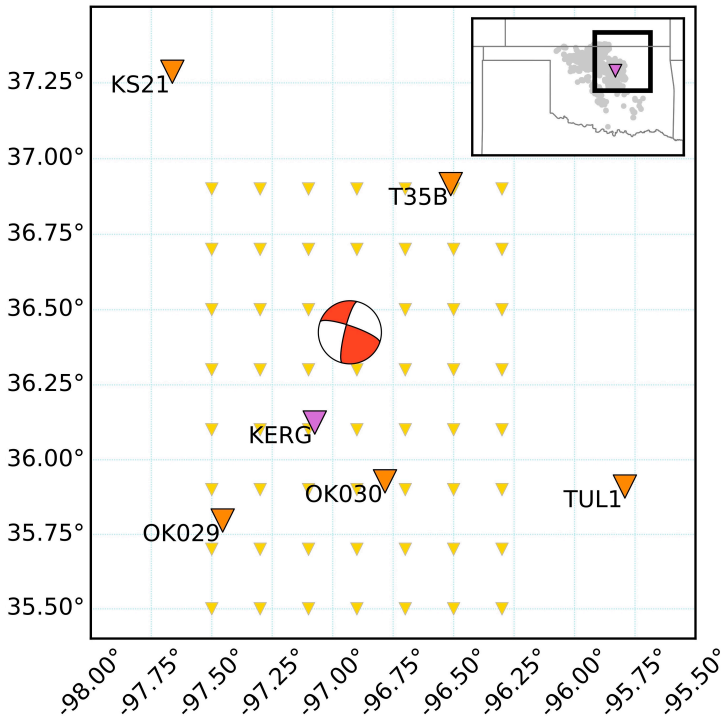

Figure 5.7: Map of stations used in synthetic waveform forward modeling. Orange triangles are regional seismic stations that recorded the 2016 Pawnee earthquake without clipping. The pink triangle is the location of the structure that is being monitored. And the yellow triangles are a grid of stations that we will use for validating the synthetic ground motions. Also included in the map is the focal mechanism of the 2016 Pawnee earthquake.

parameterized based on crustal strike slip events and varies with depth as

$$v_r = \begin{cases} 0.56 \times v_s & d < 2 \text{ km} \\ 0.8 \times v_s & d > 3.3 \text{ km} \end{cases} \tag{5.1}$$

where v_s is the shear wave speed in the velocity model at depth d, and there is a linear transition in rupture velocity between the two depth limits. We choose these depth limits because the north-central Oklahoma region has 2-3 km of sedimentary rock overlying crystalline basement (Walsh & Zoback, 2016), where the chosen deeper limit corresponds to the top of the basement in our preferred velocity model. We use the 1D Earth structure model in Sun and Hartzell (2014) because it produces synthetic waveforms of the 2016 M_w5.8 Pawnee earthquake that capture

the long-duration shaking observed at regional stations near Stillwater (Figure 5.8). Following Melgar et al. (2016), we choose a source time function with a Dreger-type functional form (Mena et al., 2010), where the local slip duration T_i scales with the local slip amount s_i and depth d following

$$T_i = \begin{cases} 2ks_i^{1/2} & d < 2 \text{ km} \\ ks_i^{1/2} & d > 3.3 \text{ km} \end{cases} \tag{5.2}$$

where the value k is specified such that the average slip duration over the total rupture region is equal to the empirical relationship to the seismic moment in Somerville et al. (1999):

$$\langle T_i \rangle = 4.308 \times 10^{-7} M_0^{1/3} \tag{5.3}$$

where the moment M_0 is in units of N-m. Synthetic displacement and velocity waveforms are computed at stations of interest at a 5 Hz sampling rate using the Zhu and Rivera (2002) frequency-wavenumber method.

5.6.2 Method Validation using Observations of the 2016 M_w5.8 Pawnee Earthquake

Generating realistic ground motions requires an accurate velocity model and an understanding of the local site effects. We verify that the simulation approach is appropriate for the Stillwater region by comparing to observations of the 2016 M_w5.8 Pawnee earthquake with the deterministic finite fault rupture as well as a distribution of randomly-generated rupture scenarios with magnitudes of the Pawnee event. Assuming the ground motion prediction equations (GMPEs) are appropriate for the region, the ground motion variability should match that of the GMPE uncertainties. We use the forward modeling procedure of Melgar and Bock (2015) to compute synthetic velocities, which uses the frequency-wavenumber approach of Zhu and Rivera (2002)

to compute the Green's functions.

We first examine the synthetic velocities computed from the deterministic finite fault rupture with observations from 5 broadband seismometers (Figure 5.7). We use the rupture model derived by Grandin et al. (2017), who performed a kinematic inversion using data from 10 teleseismic velocity waveforms, velocities from the 5 closest broadband seismometers that did not clip, and coseismic displacements from an interferogram. The velocity model the authors used in the slip inversion was derived from a centroid moment tensor solution and allowed for the inversion solution to fit the teleseismic data well, but the long-period resonances at some of the broadband stations were not replicated. The velocity model of Sun and Hartzell (2014) allows for the long-period resonances observed at stations OK029 and OK030, regional stations located closest to the instrumented structure in Stillwater. Figure 5.8 shows a comparison of these synthetic velocities with the observed waveforms. The ground level acceleration observations of the M4 earthquakes at the structure also exhibit extended duration of long-period shaking, so this is a characteristic we are interested in replicating with the synthetic waveforms from the earthquake scenarios.

Next, we simulate synthetic waveforms for 50 realizations of stochastic rupture scenarios with target magnitude of M_w5.8 on the Sooner Lake Fault, the previously unmapped fault that ruptured during the 2016 Pawnee earthquake. We created a planar fault model that has the strike and dip according to the USGS focal mechanism. The fault is discretized into 0.5 km $\times$ 0.5 km sections, with total fault dimensions corresponding to the fault model used in Grandin et al. (2017). We set the rake to correspond to the rake from the USGS focal mechanism of the 2016 Pawnee earthquake, but we allow the hypocenter of each stochastic rupture scenario to be random. We create 5 Hz synthetic waveforms at the five closest stations that observed the 2016 Pawnee earthquake without clipping, the location of the building that we are monitoring, and a grid of stations around the Stillwater, Oklahoma area (Figure 5.7). Figure 5.9 shows some example kinematic ruptures generated for this target earthquake.

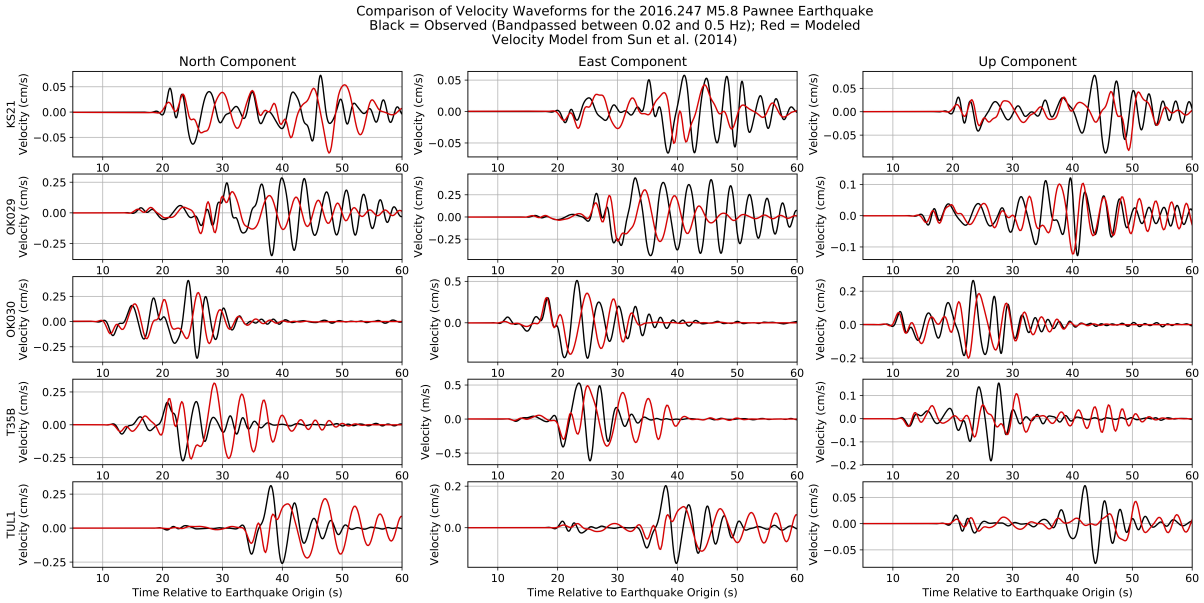

Figure 5.8: Comparison of velocity waveforms (bandpass filtered between 2-50 s periods) for the 2016 M_w5.8 Pawnee earthquake at regional seismic stations that did not clip in amplitude. Observations are shown by the black lines, and the red lines are synthetic velocities computed using the Grandin et al. (2017) static slip inversion solution.

For the earthquake observations as well as all of the synthetic waveforms, we compute the spectral accelerations (SA) at frequencies of 0.1, 0.2, 0.5, and 1.0 Hz in order to verify that the overall level of ground shaking produced by the synthetic ruptures is consistent with observations. We also compare these SA values to mean values of a regional ground motion prediction equation (GMPE) for the central United States (Atkinson & Boore, 2006). Figure 5.10 summarizes this comparison. We see that while the synthetic waveforms in Figure 5.7 capture the qualitative characteristics of shaking seen in the observed waveforms, and that the SA for the Sooner Lake Fault rupture scenarios are similar to the SA for the Grandin et al. (2017) source inversion, the synthetic waveforms are underestimating the SA observed at the stations. The SA of the synthetic waveforms are also underestimated compared to the SA of the GMPE, particularly at higher frequencies. This implies that uncertainties in velocity structure and site conditions are probably playing a significant role, and that further work should be done to investigate the relative uncertainties of velocity structure and fault slip.

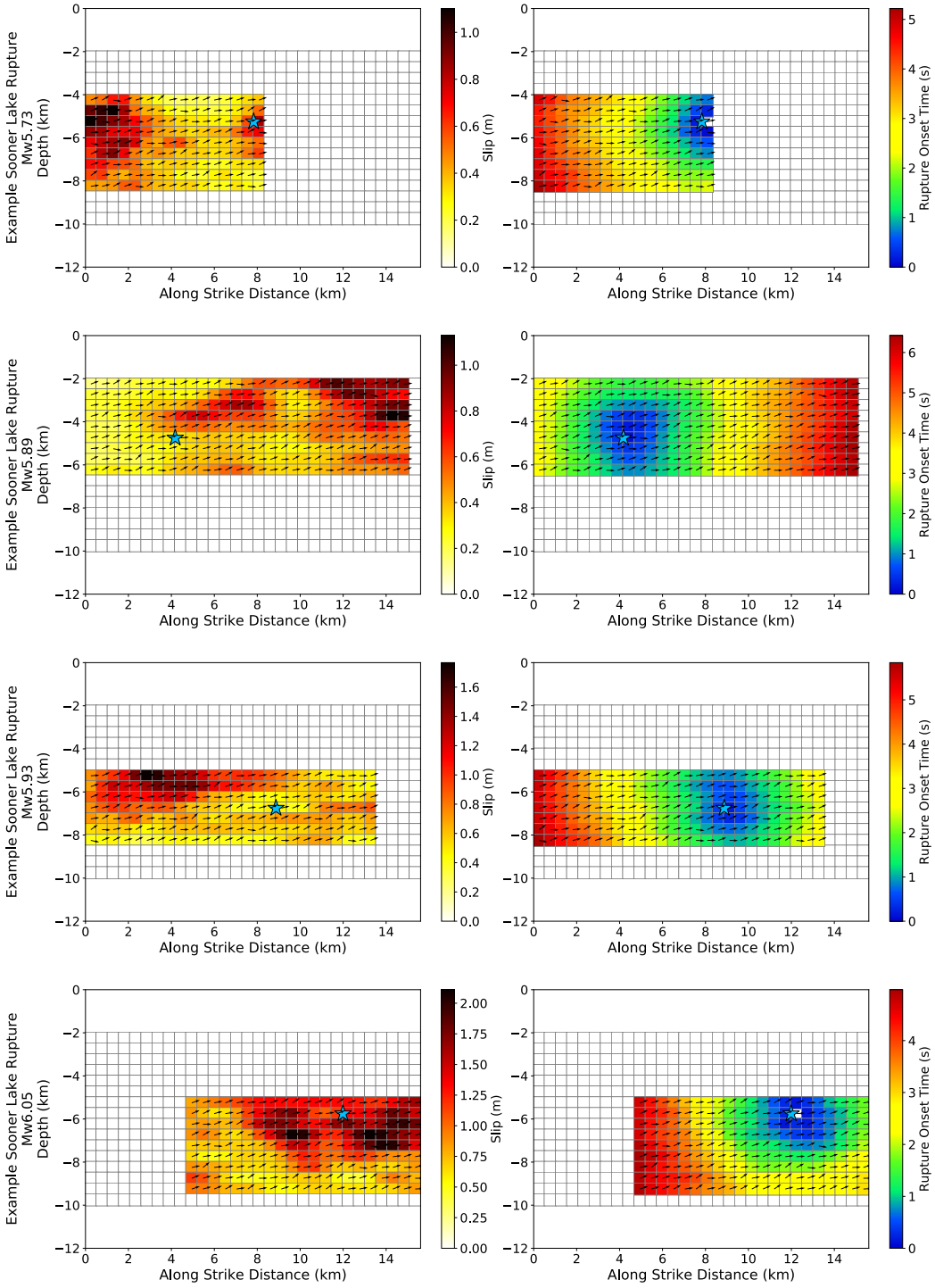

Figure 5.9: Example kinematic rupture scenarios for a Sooner Lake Fault earthquake, with target magnitude of M_w5.8. The left column shows the slip distribution and the right column shows the rupture onset time for the rupture models. The hypocenter of each rupture is shown by the blue star. Please note the different limits in the color scales for each rupture scenario.

5.7 Summary and Future Directions

Oklahoma has experienced an increase in seismicity in recent years due to wastewater injection related to oil and natural gas production. As many buildings in Oklahoma were constructed before this increase, it is important to verify that the response of the buildings to the seismicity is consistent with current models for structural response. We have installed GNSS and strong-motion accelerometers on a 12-story building on the Oklahoma State University campus to determine the response to seismic shaking in an aging reinforced concrete structure not originally designed to withstand seismic shaking. In the first year of building monitoring we have recorded 10 M4+ earthquakes, which we have used to compute the structural response. Analysis of the acceleration power spectra indicate that the dominant frequencies of the building motion are 1.3 Hz and 2.2 Hz for the north-south direction and 2.5 Hz for the east-west direction. This is consistent with the aspect ratio for the building, however, the frequencies are higher than expected given the height of the building.

We have used these observed resonances to assess a preliminary FEM of the building, which will be used to analyze the response of the building to strong ground motion from larger earthquake scenarios. The FEM consisted of the weight-bearing frame of the building, and when ground accelerations from an observed M4.6 earthquake was input to the building simulation, the FEM was shown to have resonances at lower frequencies than observed. This suggests that additional aspects of the building's construction contribute to the resonance of the building, and FEMs should contain more complexity than the building's frame in order to accurately simulate the shaking behavior. Future versions of the FEM for the building will assess whether adding the exterior walls of the building will increase the stiffness to where the simulated resonance frequencies coincide with observations.

As the observed earthquakes have not produced ground motions above the noise level of the rooftop GNSS, we plan to create kinematic rupture scenarios of M_w6 earthquakes on the Lake

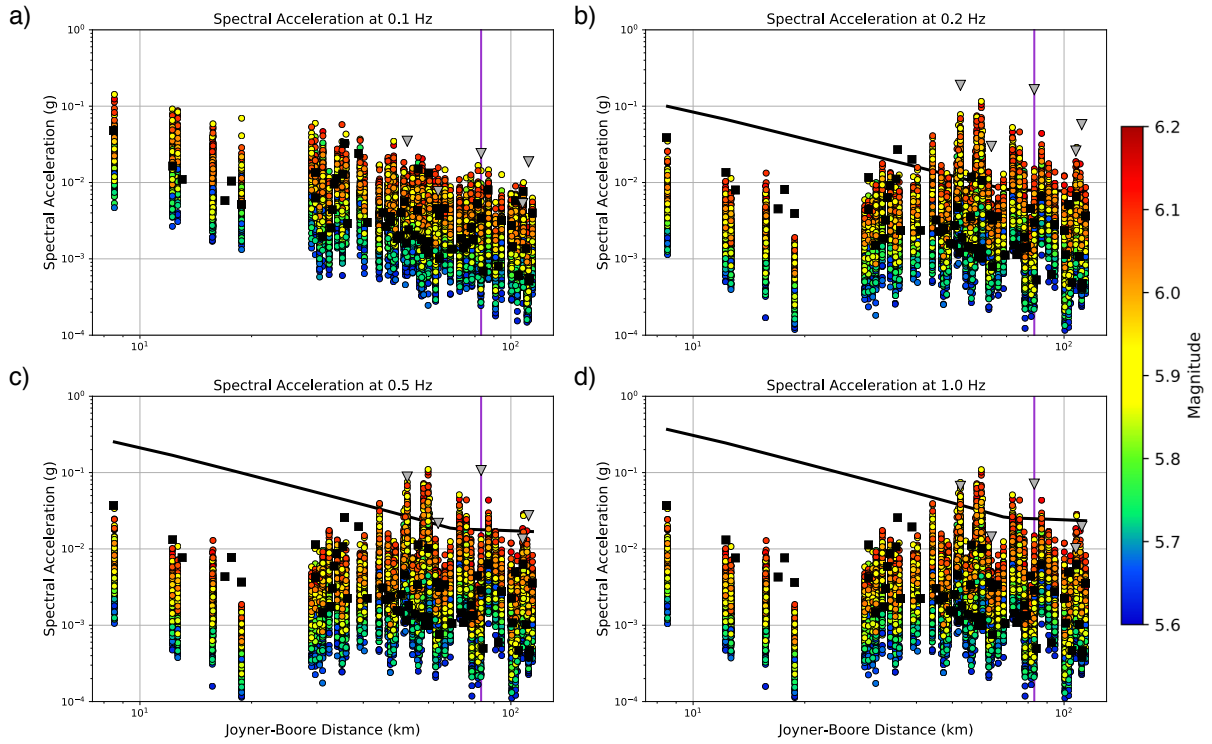

Figure 5.10: Comparison of spectral accelerations (SA) at **(a)** 0.1 Hz, **(b)** 0.2 Hz, **(c)** 0.5 Hz, and **(d)** 1.0 Hz as a function of the Joyner-Boore distance of the stations shown in Figure 5.6 to the Sooner Lake Fault model. The SA for the Sooner Lake Fault kinematic rupture scenarios are indicated by the circles and colored by final magnitude. The SA for the Grandin et al. (2017) source inversion of the 2016 Pawnee earthquake are shown by the black squares, and the SA for the earthquake observations are shown by the gray triangles. The theoretical spectral accelerations for each frequency computed using the Atkinson and Boore (2006) GMPE assuming M_w5.8 are plotted as the black lines. Also plotted in each subplot is the Joyner-Boore distance to the location of the instruments on Kerr Hall (purple line).

Carl Blackwell fault to use in the FEM simulations. We follow the approach of Melgar et al. (2016) to compute the kinematic rupture models. To validate our approach for the Stillwater, Oklahoma, area, we synthesized waveforms for the 2016 M_w5.8 Pawnee earthquake and similar scenarios, and we compared these to observations and a GMPE designed for the central United States (Atkinson & Boore, 2006). We find that the SA of the synthetic waveforms are underestimated compared to the mean SA values from the regional GMPE, and that the velocity structure used to compute the synthetic waveforms may need to be adjusted to improve the SA values expected for this region. After verification of the low-frequency content of the synthetic waveforms, future

analysis will also incorporate stochastic high-frequency components to the synthetic velocities through the SCEC Broadband Platform (Maechling et al., 2014) in order to increase the frequency content of the synthetic waveforms and allow us to compare peak ground acceleration values of the synthetic waveforms with the mean values from the GMPE. Increasing the frequency content to incorporate higher frequencies (up to 10 Hz) will make the synthetic waveforms appropriate for use in the finite element simulations of the building.

5.8 Acknowledgements

Chapter 5 is part of a larger study currently being prepared for publication which is coauthored with Jennifer Haase, Mohamed Soliman, Omid Khandel, Frankie Martinez, and Imran Sheikh. The dissertation author is the primary investigator and author of the material presented in this chapter.

Instrumentation was funded by UCSD Academic Senate Marine Research Grant RQ235R-HAASE and NSF grant OAC-183572. Mohamed Soliman, Omar Khalid, and Imran Sheikh (OSU) constructed the finite element model of Kerr Hall and assisted with instrument installation. We thank Priyank Jaiswal (OSU), Weixing Zhang (Wuhan University), and Haejo Kim for their contributions to this project. We thank D. Glen Offield (UCSD), Tim Sickbert, Brian Johnson, Chris Waite, and Joe Anthony (OSU) for assistance with instrument design and deployment. We thank Frank Vernon, Julian Reyes, Geoff Davis, Jennifer Eakins, and Jon Tytell with assistance with the Antelope System and implementing the data streams from the monitoring stations within the Array Network Facility at SIO. We thank Martin Vallee for providing the slip inversion solution described in Grandin et al. (2017). Kinematic rupture models and synthetic waveforms were computed using the FakeQuakes code (github/dmelgarm/FakeQuakes). Green's functions were computed using the frequency-wavenumber method of Zhu and Rivera (2002) (www.eas.slu.edu/People/LZhu/downloads/fk3.2.tar). Focal mechanisms are from the USGS

catalog (https://earthquake.usgs.gov). Mapped faults are from the Oklahoma Geological Survey (www.ou.edu/content/ogs/data/fault.html).

Chapter 6

Conclusions

Subduction zone earthquakes and the tsunamis generated by these earthquakes are highly hazardous to coastal populations. As these populations continue to rise, the risks posed by these natural hazards on damage to infrastructure and public safety increase. In this dissertation, we explored how GNSS data used in conjunction with other geophysical instrumentation can provide detailed information about strong ground motion for use in building monitoring and early warning applications.

We first discussed the applications to near-source tsunami early warning, particularly for tsunamis generated by $M_w \sim 8$ megathrust earthquakes. For a local tsunami caused by a megathrust earthquake, strong shaking from the earthquake is typically the first indication that a tsunami might be coming, and coastal populations should begin to evacuate to higher ground when shaking subsides. However, tsunami earthquakes, $M_w \sim 8$ megathrust earthquakes that occur in the shallowest portion of the subduction zone near the trench and generate anomalously large tsunamis, tend to be depleted in high-frequency energy and generally do not produce strong high-frequency shaking typical of large tsunamigenic earthquakes. This makes tsunami earthquakes particularly hazardous for local coastal populations, as people will not necessarily realize that they need to evacuate. Near-source tsunami early warning systems that alert coastal

populations of an incoming tsunami can help aid evacuation efforts.

In Chapter 2 we examined, using synthetic rupture scenarios of M_w8 Cascadia megathrust earthquakes, how coseismic offset estimates from onshore GNSS observations can be augmented with offshore coseismic estimates from seafloor geodetic instrumentation to improve static slip solutions that can lead to more accurate tsunami wave estimates at the coastline nearest the earthquake. Accurate estimation of tsunami impacts based on seafloor deformation from static slip inversions requires recovering the maximum fault slip and along-strike rupture extent. We found that onshore GNSS coseismic observations alone are not enough to reliably constrain thees values for the case of a shallow tsunami earthquake. We determined that an array of seafloor stations oriented in a trench-parallel profile located over the deformation front, when augmented with onshore coseismic observations, distinguishes both the depth location of the rupture and the along-strike slip extent. This work has demonstrated that a trench-parallel profile would be an optimal offshore network configuration when expanding real-time monitoring networks offshore.

We found that while the along-depth slip location can be constrained using vertical coseismic offset information that could potentially be derived using seafloor pressure sensors, determining the along-strike slip extent and slip amplitude using static slip inversions require horizontal coeismic data on the seafloor, particularly for shallow tsunami earthquakes. Instruments that measure horizontal coseismic displacements on the seafloor in real time have not yet been developed. Additionally, offshore vertical coseismic data is complicated by the superposition of the tsunami pressure signal with the ground motion vertical uplift signal (e.g., Saito & Tsushima, 2016), so static slip inversions using offshore data will have to wait before accurate offshore coseismic observations become available to incorporate into the inversion.

In Chapter 3 we turned to examining how the early portions of the seismic waveforms from presently-available instruments, high-rate GNSS sensors and three-component strong-motion accelerometers, can be used to determine slip location for M_w8 megathrust earthquakes. We use a set of rupture scenarios developed for the Cascadia subduction zone to investigate if imposing

depth-dependent slip constraints in modified kinematic slip inversions can help rapidly exclude or confirm the likelihood of shallow slip and therefore exclude or confirm the possibility of a shallow tsunami earthquake. To reduce the size of the inversion problem, we approximated the rupture velocity and local slip duration using the hypocenter, structural velocity model, and rapid magnitude estimate in order to only solve for fault slip. We found that PGD misfit is a robust criteria for distinguishing slip depth, but that further improvements in approximating rupture velocity in the waveform inversions are necessary to increase confidence in this technique.

As demonstrated in the previous chapters, knowing the displacement is crucial for characterizing source properties of large earthquake using near-field observations. Integrated strong-motion accelerometer data contain baseline drift effects that make it impractical for obtaining near-field coseismic offset information. Methods have been developed that constrain integrated accelerometer data with high-rate GNSS data to produce broadband displacement waveforms that preserve the low-frequency shaking and coseismic offset information (e.g., Emore et al., 2007; Smyth & Wu, 2007; Bock et al., 2011). These methods require the GNSS sensor and strong-motion accelerometer to be collocated, which is not usually the case in existing seismic and geodetic networks.

One approach to densifying seismogeodetic networks is to install collocated low-cost MEMS accelerometers at existing GNSS stations. In Chapter 4, we assessed the reliability of seismogeodetic displacement and velocity waveforms using MEMS accelerometer observations compared to those using observatory-grade accelerometers when subjected to strong ground motion on a shake table experiment. We also examined the practical sensitivity limits of these MEMS accelerometers by looking at recordings of near-source M$\sim$4 earthquakes at field stations. We determined that MEMS accelerometers with this comparatively low dynamic range compared to observatory-grade accelerometers are suitable for measuring ground motions at frequencies of interest for earthquake early warning and rapid response applications if sufficient quality control requirements are met.

The shake table experiment also demonstrated the ability of seismogeodetic instrumentation to measure the response of a building to seismic shaking. This motivated us to gather in-situ seismogeodetic measurements of building motion in a region experiencing high seismic activity. In Chapter 5, we described a building monitoring project in Oklahoma, where we have installed seismogeodetic instrumentation on an aging reinforced concrete structure that has experienced frequent shaking from regional induced seismicity. Observations of ten M4+ earthquakes in the first year of monitoring have allowed us to estimate the response of the building, which we used to determine that a finite element model of the building needed to contain more complexity than just the weight-bearing elements in order to simulate the building motion accurately. We also discussed the development of synthetic ground motions from M_w6 rupture scenarios on a nearby fault that we will use as input to these finite element simulations. Such studies will help quantify the hazard posed by aging reinforced concrete structures subjected to frequent shaking that these buildings were not originally designed to withstand.

References

Akaike, H. (1998). Likelihood and the bayes procedure. In *Selected Papers of Hirotugu Akaike* (pp. 309–332). Springer.

Allen, R. M., Gasparini, P., Kamigaichi, O., & Bose, M. (2009). The status of earthquake early warning around the world: An introductory overview. *Seismological Research Letters*, *80*(5), 682–693.

Allen, R. M., & Ziv, A. (2011). Application of real-time GPS to earthquake early warning. *Geophysical Research Letters*, *38*(16).

Ammon, C. J., Kanamori, H., Lay, T., & Velasco, A. A. (2006). (The 17 July 2006 Java tsunami earthquake. *Geophysical Research Letters*, *33*(24).

Atkinson, G. M., & Boore, D. M. (2006). Earthquake ground-motion prediction equations for eastern North America. *Bulletin of the seismological society of America*, *96*(6), 2181–2205.

Atwater, B. F., Nelson, A. R., Clague, J. J., Carver, G. A., Yamaguchi, D. K., Bobrowsky, P. T., ... others (1995). Summary of coastal geologic evidence for past great earthquakes at the Cascadia subduction zone. *Earthquake Spectra*, *11*(1), 1–18.

Berger, M. J., George, D. L., LeVeque, R. J., & Mandli, K. T. (2011). The GeoClaw software for depth-averaged flows with adaptive refinement. *Advances in Water Resources*, *34*(9), 1195–1206.

Bernard, E., & Titov, V. (2015). Evolution of tsunami warning systems and products. *Philosophical Transactions of the Royal Society A: Mathematical, Physical and Engineering Sciences*, *373*(2053), 20140371.

Bernard, E. N. (2005). *Developing tsunami-resilient communities: the national tsunami hazard mitigation program*. Springer Science & Business Media.

Blaser, L., Krüger, F., Ohrnberger, M., & Scherbaum, F. (2010). Scaling relations of earthquake source parameter estimates with special focus on subduction environment. *Bulletin of the Seismological Society of America*, *100*(6), 2914–2926.

Blewitt, G., Hammond, W. C., Kreemer, C., Plag, H.-P., Stein, S., & Okal, E. (2009). GPS for real-time earthquake source determination and tsunami warning systems. *Journal of Geodesy*, *83*(3-4), 335–343.

Blewitt, G., Kreemer, C., Hammond, W. C., Plag, H.-P., Stein, S., & Okal, E. (2006). Rapid determination of earthquake magnitude using GPS for tsunami warning systems. *Geophysical Research Letters*, *33*(11).

Blum, J. A., Nooner, S. L., & Zumberge, M. A. (2008). Recording Earth strain with optical fibers. *IEEE Sensors Journal*, *8*(7), 1152–1160.

Bock, Y., Melgar, D., & Crowell, B. W. (2011). Real-time strong-motion broadband displacements from collocated GPS and accelerometers. *Bulletin of the Seismological Society of America*, *101*(6), 2904–2925.

Bock, Y., Nikolaidis, R. M., Jonge, P. J., & Bevis, M. (2000). Instantaneous geodetic positioning at medium distances with the Global Positioning System. *Journal of Geophysical Research: Solid Earth*, *105*(B12), 28223–28253.

Bock, Y., Prawirodirdjo, L., & Melbourne, T. I. (2004). Detection of arbitrarily large dynamic ground motions with a dense high-rate GPS network. *Geophysical Research Letters*, *31*(6).

Boore, D. M. (1999). *Effect of baseline corrections on response spectra for two recordings of the 1999 Chi-Chi, Taiwan, earthquake*. US Department of the Interior, US Geological Survey.

Boore, D. M. (2001). Effect of baseline corrections on displacements and response spectra for several recordings of the 1999 Chi-Chi, Taiwan, earthquake. *Bulletin of the Seismological Society of America*, *91*(5), 1199–1211.

Boore, D. M., & Bommer, J. J. (2005). Processing of strong-motion accelerograms: needs, options and consequences. *Soil Dynamics and Earthquake Engineering*, *25*(2), 93–115.

Boore, D. M., Stephens, C. D., & Joyner, W. B. (2002). Comments on baseline correction of digital strong-motion data: Examples from the 1999 Hector Mine, California, earthquake. *Bulletin of the Seismological Society of America*, *92*(4), 1543–1560.

Brown, H. M., Allen, R. M., Hellweg, M., Khainovski, O., Neuhauser, D., & Souf, A. (2011). Development of the ElarmS methodology for earthquake early warning: Realtime application in California and offline testing in Japan. *Soil Dynamics and Earthquake Engineering*, *31*(2), 188–200.

Brune, J. N. (1970). Tectonic stress and the spectra of seismic shear waves from earthquakes. *Journal of Geophysical Research*, *75*(26), 4997–5009.

Bürgmann, R., & Chadwell, D. (2014). Seafloor Geodesy. *Annual Review of Earth and Planetary*

Sciences, *42*, 509–534.

Byrne, D. E., Davis, D. M., & Sykes, L. R. (1988). Loci and maximum size of thrust earthquakes and the mechanics of the shallow region of subduction zones. *Tectonics*, *7*(4), 833–857.

Çelebi, M. (2000). GPS in dynamic monitoring of long-period structures. *Soil Dynamics and Earthquake Engineering*, *20*(5-8), 477–483.

Center for International Earth Science Information Network - CIESIN - Columbia University. (2017). *Gridded Population of the World, Version 4 (GPWv4): Population Count, Revision 10.* NASA Socioeconomic Data and Applications Center (SEDAC). Retrieved from `https://doi.org/10.7927/H4PG1PPM)`

Chadwell, C. D. (2016). Initiation of GPS-acoustics measurements on the continental slope of the Cascadia subduction zone. In *Agu fall meeting abstracts.*

Chadwell, C. D., Schmidt, D. A., Webb, S. C., Nooner, S. L., Ericksen, T. L., Brooks, B. A., & Foster, J. H. (2018). Expansion of GPS-Acoustic Arrays offshore the Cascadia and Alaska Subduction Zones. In *Agu fall meeting abstracts.*

Chao, W.-A., Wu, Y.-M., & Zhao, L. (2010). An automatic scheme for baseline correction of strong-motion records in coseismic deformation determination. *Journal of seismology*, *14*(3), 495–504.

Choi, K., Bilich, A., Larson, K. M., & Axelrad, P. (2004). Modified sidereal filtering: Implications for high-rate GPS positioning. *Geophysical research letters*, *31*(22).

Clayton, P., Zalachoris, G., Rathje, E., Bheemasetti, T., Caballero, S., Yu, X., & Bennett, S. (2016). The geotechnical aspects of the September 3, 2016 M 5.8 Pawnee, Oklahoma earthquake. *GEER Association, Berkeley, California, doi*, *10*, G69885.

Clayton, R. W., Heaton, T., Chandy, M., Krause, A., Kohler, M., Bunn, J., ... others (2012). Community seismic network. *Annals of Geophysics*, *54*(6).

Cochran, E. S., Kohler, M. D., Given, D. D., Guiwits, S., Andrews, J., Meier, M.-A., ... Smith, D. (2018). Earthquake early warning ShakeAlert system: Testing and certification platform. *Seismological Research Letters*, *89*(1), 108–117.

Cochran, E. S., Lawrence, J. F., Christensen, C., & Jakka, R. S. (2009). The quake-catcher network: Citizen science expanding seismic horizons. *Seismological Research Letters*, *80*(1), 26–30.

Colombelli, S., Allen, R. M., & Zollo, A. (2013). Application of real-time GPS to earthquake early warning in subduction and strike-slip environments. *Journal of Geophysical Research: Solid Earth*, *118*(7), 3448–3461.

Computers & Structures, Inc. (2014). CSi Analysis Reference Manual [Computer software manual]. Berkeley, CA.

Conte, J. P., Luco, J. E., Restrepo, J., Seible, F., & Van Den Einde, L. (2004). UCSD-NEES large high performance outdoor shake table. In *Proceedings of the 17th ASCE engineering mechanics conference. Newark, DE: University of Delaware.*

Crowell, B. W., Bock, Y., & Melgar, D. (2012). Real-time inversion of GPS data for finite fault modeling and rapid hazard assessment. *Geophysical Research Letters*, *39*(9).

Crowell, B. W., Bock, Y., & Squibb, M. B. (2009). Demonstration of earthquake early warning using total displacement waveforms from real-time GPS networks. *Seismological Research Letters*, *80*(5), 772–782.

Crowell, B. W., Melgar, D., Bock, Y., Haase, J. S., & Geng, J. (2013). Earthquake magnitude scaling using seismogeodetic data. *Geophysical Research Letters*, *40*(23), 6089–6094.

Crowell, B. W., Schmidt, D. A., Bodin, P., Vidale, J. E., Baker, B., Barrientos, S., & Geng, J. (2018). G-FAST earthquake early warning potential for great earthquakes in Chile. *Seismological Research Letters*, *89*(2A), 542–556.

Crowell, B. W., Schmidt, D. A., Bodin, P., Vidale, J. E., Gomberg, J., Renate Hartog, J., ... others (2016). Demonstration of the Cascadia G-FAST geodetic earthquake early warning system for the Nisqually, Washington, earthquake. *Seismological Research Letters*, *87*(4), 930–943.

Davis, C., & Fisk, J. M. (2017). Mitigating risks from fracking-related earthquakes: assessing state regulatory decisions. *Society & natural resources*, *30*(8), 1009–1025.

Dempsey, D., & Riffault, J. (2018). Response of induced seismicity to injection rate reduction: models of delay, decay, quiescence, recovery and Oklahoma. *Water Resources Research*.

Duputel, Z., Rivera, L., Kanamori, H., Hayes, G. P., Hirshorn, B., & Weinstein, S. (2011). Real-time W phase inversion during the 2011 off the Pacific coast of Tohoku Earthquake. *Earth, planets and space*, *63*(7), 5.

Ellsworth, W. L. (2013). Injection-induced earthquakes. *Science*, *341*(6142), 1225942.

Ellsworth, W. L., Llenos, A. L., McGarr, A. F., Michael, A. J., Rubinstein, J. L., Mueller, C. S., ... Calais, E. (2015). Increasing seismicity in the US midcontinent: Implications for earthquake hazard. *The Leading Edge*, *34*(6), 618–626.

Emore, G. L., Haase, J. S., Choi, K., Larson, K. M., & Yamagiwa, A. (2007). Recovering seismic displacements through combined use of 1-Hz GPS and strong-motion accelerometers. *Bulletin of the Seismological Society of America*, *97*(2), 357–378.

Evans, J., Allen, R. M., Chung, A., Cochran, E., Guy, R., Hellweg, M., & Lawrence, J. (2014). Performance of several low-cost accelerometers. *Seismological Research Letters*, *85*(1), 147–158.

Federal Emergency Management Agency (FEMA). (2004). NEHERP Recommended Provisions for Seismic Regulations for New Buildings and Other Structures. *FEMA 450-1/2003 Edition, Part 1: Provisions, Federal Emergency Management Agency, Washington, D.C.*.

Fleischman, R., Restrepo, J., Nema, A., Zhang, D., Shakya, U., Zhang, Z., ... Monti, G. (2015). Inertial force-limiting anchorage system for seismic resistant building structures. In *Structures congress* (pp. 1302–1313).

Fritz, H. M., Borrero, J. C., Suwargadi, B., Lin, L., Qiang, Q., Pranantyo, I. R., ... Synolakis, C. E. (2011). Reconnaissance of the 25 October 2010 Mentawai Islands tsunami in Indonesia. *EGU2011-9512*.

Fujiwara, T., Kodaira, S., No, T., Kaiho, Y., Takahashi, N., & Kaneda, Y. (2011). The 2011 Tohoku-Oki earthquake: Displacement reaching the trench axis. *Science*, *334*(6060), 1240–1240.

Galetzka, J., Melgar, D., Genrich, J. F., Geng, J., Owen, S., Lindsey, E. O., ... others (2015). Slip pulse and resonance of the Kathmandu basin during the 2015 Gorkha earthquake, Nepal. *Science*, *349*(6252), 1091–1095.

Geng, J., Bock, Y., Melgar, D., Crowell, B. W., & Haase, J. S. (2013). A new seismogeodetic approach applied to GPS and accelerometer observations of the 2012 Brawley seismic swarm: Implications for earthquake early warning. *Geochemistry, Geophysics, Geosystems*, *14*(7), 2124–2142.

Genrich, J. F., & Bock, Y. (1992). Rapid resolution of crustal motion at short ranges with the Global Positioning System. *Journal of Geophysical Research: Solid Earth*, *97*(B3), 3261–3269.

Genrich, J. F., & Bock, Y. (2006). Instantaneous geodetic positioning with 10–50 Hz GPS measurements: Noise characteristics and implications for monitoring networks. *Journal of Geophysical Research: Solid Earth*, *111*(B3).

Goldfinger, C., Nelson, C., Morey, A., Johnson, J., Patton, J., Karabanov, E., ... others (2012). *Turbidite Event History: Methods and Implications for Holocene Paleoseismicity of the Cascadia Subduction Zone: US Geological Survey Professional Paper 1661-F, Reston, Virginia, US Geological Survey.*

Goldfinger, C., Nelson, C. H., Johnson, J. E., & Party, S. S. (2003). Holocene earthquake records from the Cascadia subduction zone and northern San Andreas fault based on precise dating of offshore turbidites. *Annual Review of Earth and Planetary Sciences*, *31*(1), 555–577.

González, F. I., Bernard, E. N., Meinig, C., Eble, M. C., Mofjeld, H. O., & Stalin, S. (2005). The NTHMP tsunameter network. *Natural Hazards*, *35*(1), 25–39.

Graizer, V. (1979). Determination of the true ground displacement by using strong motion records. *Izvestiya Phys. Solid Earth*, *15*(12), 875–885.

Grandin, R., Vallée, M., & Lacassin, R. (2017). Rupture process of the Mw 5.8 Pawnee, Oklahoma, earthquake from Sentinel-1 InSAR and seismological data. *Seismological Research Letters*, *88*(4), 994–1004.

Grapenthin, R., Johanson, I. A., & Allen, R. M. (2014). Operational real-time GPS-enhanced earthquake early warning. *Journal of Geophysical Research: Solid Earth*, *119*(10), 7944–7965.

Graves, R. W., & Pitarka, A. (2010). Broadband ground-motion simulation using a hybrid approach. *Bulletin of the Seismological Society of America*, *100*(5A), 2095–2123.

Gregor, N. J., Silva, W. J., Wong, I. G., & Youngs, R. R. (2002). Ground-motion attenuation relationships for Cascadia subduction zone megathrust earthquakes based on a stochastic finite-fault model. *Bulletin of the Seismological Society of America*, *92*(5), 1923–1932.

Hartzell, S. H., & Heaton, T. H. (1983). Inversion of strong ground motion and teleseismic waveform data for the fault rupture history of the 1979 Imperial Valley, California, earthquake. *Bulletin of the Seismological Society of America*, *73*(6A), 1553–1583.

Haskell, N. (1964). Total energy and energy spectral density of elastic wave radiation from propagating faults. *Bulletin of the Seismological Society of America*, *54*(6A), 1811–1841.

Hayes, G. P., Earle, P. S., Benz, H. M., Wald, D. J., & Briggs, R. W. (2011). 88 Hours: The US Geological Survey National Earthquake Information Center Response to the 11 March 2011 Mw 9.0 Tohoku Earthquake. *Seismological Research Letters*, *82*(4), 481–493.

Herring, T. A., Melbourne, T. I., Murray, M. H., Floyd, M. A., Szeliga, W. M., King, R. W., ... Wang, L. (2016). Plate Boundary Observatory and related networks: GPS data analysis methods and geodetic products. *Reviews of Geophysics*, *54*(4), 759–808.

Hill, E. M., Borrero, J. C., Huang, Z., Qiu, Q., Banerjee, P., Natawidjaja, D. H., ... others (2012). The 2010 Mw 7.8 Mentawai earthquake: Very shallow source of a rare tsunami earthquake determined from tsunami field survey and near-field GPS data. *Journal of Geophysical Research: Solid Earth*, *117*(B6).

Hirshorn, B., Weinstein, S., & Tsuboi, S. (2013). On the application of Mwp in the near field and the March 11, 2011 Tohoku earthquake. *Pure and Applied Geophysics*, *170*(6-8), 975–991.

Hoshiba, M., & Ozaki, T. (2014). Earthquake Early Warning and Tsunami Warning of the Japan

Meteorological Agency, and Their Performance in the 2011 off the Pacific Coast of Tohoku Earthquake (Mw9.0). In *Early Warning for Geological Disasters* (pp. 1–28). Springer.

Hu, Y., & Wang, K. (2008). Coseismic strengthening of the shallow portion of the subduction fault and its effects on wedge taper. *Journal of Geophysical Research: Solid Earth*, *113*(B12).

Hyndman, R. D., Yamano, M., & Oleskevich, D. A. (1997). The seismogenic zone of subduction thrust faults. *Island Arc*, *6*(3), 244–260.

Ide, S., Baltay, A., & Beroza, G. C. (2011). Shallow dynamic overshoot and energetic deep rupture in the 2011 Mw 9.0 Tohoku-Oki earthquake. *Science*, *332*(6036), 1426–1429.

Ide, S., Takeo, M., & Yoshida, Y. (1996). Source process of the 1995 Kobe earthquake: determination of spatio-temporal slip distribution by Bayesian modeling. *Bulletin of the Seismological Society of America*, *86*(3), 547–566.

Iwan, W. D., Moser, M. A., & Peng, C.-Y. (1985). Some observations on strong-motion earthquake measurement using a digital accelerograph. *Bulletin of the Seismological Society of America*, *75*(5), 1225–1246.

Jaiswal, P., Gregg, J. M., Parks, S., Holman, R., Mohammadi, S., & Grammer, G. M. (2017). Evidence of fault/fracture "Hydrothermal" reservoirs in the southern midcontinent Mississippian carbonates. *Mississippian Reservoirs of the Mid-Continent, U.S.A.: American Association of Petroleum Geologists Memoir*.

Ji, C., Larson, K. M., Tan, Y., Hudnut, K. W., & Choi, K. (2004). Slip history of the 2003 San Simeon earthquake constrained by combining 1-Hz GPS, strong motion, and teleseismic data. *Geophysical Research Letters*, *31*(17).

Kanamori, H. (1972). Mechanism of tsunami earthquakes. *Physics of the Earth and Planetary Interiors*, *6*(5), 346–359.

Kanamori, H., & Kikuchi, M. (1993). The 1992 Nicaragua earthquake: a slow tsunami earthquake associated with subducted sediments. *Nature*, *361*(6414), 714.

Kanamori, H., & Rivera, L. (2008). Source inversion of Wphase: speeding up seismic tsunami warning. *Geophysical Journal International*, *175*(1), 222–238.

Kawaguchi, K., Kaneda, Y., & Araki, E. (2008). The DONET: A real-time seafloor research infrastructure for the precise earthquake and tsunami monitoring. In *OCEANS 2008-MTS/IEEE Kobe Techno-Ocean* (pp. 1–4).

Kelley, D. S., Delaney, J. R., & Juniper, S. K. (2014). Establishing a new era of submarine volcanic observatories: Cabling Axial Seamount and the Endeavour Segment of the Juan de Fuca Ridge. *Marine Geology*, *352*, 426–450.

Keranen, K. M., Weingarten, M., Abers, G. A., Bekins, B. A., & Ge, S. (2014). Sharp increase in central Oklahoma seismicity since 2008 induced by massive wastewater injection. *Science*, *345*(6195), 448–451.

Kobayashi, R., Miyazaki, S., & Koketsu, K. (2006). Source processes of the 2005 West Off Fukuoka Prefecture earthquake and its largest aftershock inferred from strong motion and 1-Hz GPS data. *Earth, planets and space*, *58*(1), 57–62.

Kodaira, S., No, T., Nakamura, Y., Fujiwara, T., Kaiho, Y., Miura, S., ... Taira, A. (2012). Coseismic fault rupture at the trench axis during the 2011 Tohoku-oki earthquake. *Nature Geoscience*, *5*(9), 646–650.

Kohler, M. D., Cochran, E. S., Given, D., Guiwits, S., Neuhauser, D., Henson, I., ... others (2018). Earthquake early warning ShakeAlert system: West coast wide production prototype. *Seismological Research Letters*, *89*(1), 99–107.

Kozdon, J. E., & Dunham, E. M. (2013). Rupture to the Trench: Dynamic Rupture Simulations of the 11 March 2011 Tohoku Earthquake. *Bulletin of the Seismological Society of America*, *103*(2B), 1275–1289.

Langbein, J., & Bock, Y. (2004). High-rate real-time GPS network at Parkfield: Utility for detecting fault slip and seismic displacements. *Geophysical Research Letters*, *31*(15).

Larson, K. M. (2009). GPS seismology. *Journal of Geodesy*, *83*(3-4), 227–233.

Larson, K. M., Bodin, P., & Gomberg, J. (2003). Using 1-Hz GPS data to measure deformations caused by the Denali fault earthquake. *Science*, *300*(5624), 1421–1424.

Lay, T., Ammon, C. J., Kanamori, H., Xue, L., & Kim, M. J. (2011). Possible large near-trench slip during the 2011 M w 9.0 off the Pacific coast of Tohoku Earthquake. *Earth, Planets and Space*, *63*(7), 32.

Lay, T., Ammon, C. J., Kanamori, H., Yamazaki, Y., Cheung, K. F., & Hutko, A. R. (2011). The 25 October 2010 Mentawai tsunami earthquake (Mw 7.8) and the tsunami hazard presented by shallow megathrust ruptures. *Geophysical Research Letters*, *38*(6).

Lay, T., Bilek, S., Dixon, T., & Moore, C. (2007). Anomalous earthquake ruptures at shallow depths on subduction zone megathrusts. *The Seismogenic Zone of Subduction Thrust Faults*, 476–511.

Lay, T., Kanamori, H., Ammon, C. J., Koper, K. D., Hutko, A. R., Ye, L., ... Rushing, T. M. (2012). Depth-varying rupture properties of subduction zone megathrust faults. *Journal of Geophysical Research: Solid Earth*, *117*(B4).

LeVeque, R. J., George, D. L., & Berger, M. J. (2011). Tsunami modelling with adaptively

refined finite volume methods. *Acta Numerica*, *20*, 211–289.

Li, S., Wang, K., Wang, Y., Jiang, Y., & Dosso, S. E. (2018). Geodetically inferred locking state of the cascadia megathrust based on a viscoelastic earth model. *Journal of Geophysical Research: Solid Earth*, *123*(9), 8056–8072.

Maechling, P. J., Silva, F., Callaghan, S., & Jordan, T. H. (2014). SCEC Broadband Platform: System architecture and software implementation. *Seismological Research Letters*, *86*(1), 27–38.

Mai, P. M., & Beroza, G. C. (2002). A spatial random field model to characterize complexity in earthquake slip. *Journal of Geophysical Research: Solid Earth*, *107*(B11), ESE–10.

McCrory, P. A., Blair, J. L., Waldhauser, F., & Oppenheimer, D. H. (2012). Juan de Fuca slab geometry and its relation to Wadati-Benioff zone seismicity. *Journal of Geophysical Research: Solid Earth*, *117*(B9).

Melgar, D., Allen, R. M., Riquelme, S., Geng, J., Bravo, F., Baez, J. C., ... others (2016). Local tsunami warnings: Perspectives from recent large events. *Geophysical Research Letters*, *43*(3), 1109–1117.

Melgar, D., & Bock, Y. (2015). Kinematic earthquake source inversion and tsunami runup prediction with regional geophysical data. *Journal of Geophysical Research: Solid Earth*, *120*(5), 3324–3349.

Melgar, D., Bock, Y., & Crowell, B. W. (2012). Real-time centroid moment tensor determination for large earthquakes from local and regional displacement records. *Geophysical Journal International*, *188*(2), 703–718.

Melgar, D., Bock, Y., Sanchez, D., & Crowell, B. W. (2013). On robust and reliable automated baseline corrections for strong motion seismology. *Journal of Geophysical Research: Solid Earth*, *118*(3), 1177–1187.

Melgar, D., Crowell, B. W., Bock, Y., & Haase, J. S. (2013). Rapid modeling of the 2011 Mw 9.0 Tohoku-Oki earthquake with seismogeodesy. *Geophysical Research Letters*, *40*(12), 2963–2968.

Melgar, D., Crowell, B. W., Geng, J., Allen, R. M., Bock, Y., Riquelme, S., ... Ganas, A. (2015). Earthquake magnitude calculation without saturation from the scaling of peak ground displacement. *Geophysical Research Letters*, *42*(13), 5197–5205.

Melgar, D., Fan, W., Riquelme, S., Geng, J., Liang, C., Fuentes, M., ... Fielding, E. J. (2016). Slip segmentation and slow rupture to the trench during the 2015, Mw8. 3 Illapel, Chile earthquake. *Geophysical Research Letters*, *43*(3), 961–966.

Melgar, D., Geng, J., Crowell, B. W., Haase, J. S., Bock, Y., Hammond, W. C., & Allen, R. M. (2015). Seismogeodesy of the 2014 mw6. 1 napa earthquake, california: Rapid response and modeling of fast rupture on a dipping strike-slip fault. *Journal of Geophysical Research: Solid Earth*, *120*(7), 5013–5033.

Melgar, D., LeVeque, R. J., Dreger, D. S., & Allen, R. M. (2016). Kinematic rupture scenarios and synthetic displacement data: An example application to the Cascadia subduction zone. *Journal of Geophysical Research: Solid Earth*, *121*(9), 6658–6674.

Mena, B., Mai, P. M., Olsen, K. B., Purvance, M. D., & Brune, J. N. (2010). Hybrid broadband ground-motion simulation using scattering Green?s functions: Application to large-magnitude events. *Bulletin of the Seismological Society of America*, *100*(5A), 2143–2162.

Menke, W. (2012). *Geophysical Data Analysis: Geophysical Inverse Theory*. Academic Press, Waltham, MA.

Merritt, F. (1996). Minimum design loads for buildings and other structures: American Society of Civil Engineers Standard 7-95. *Journal of Architectural Engineering*, *2*(2), 80–81.

Minson, S. E., Brooks, B. A., Glennie, C. L., Murray, J. R., Langbein, J. O., Owen, S. E., ... Hauser, D. L. (2015). Crowdsourced earthquake early warning. *Science advances*, *1*(3), e1500036.

Minson, S. E., Murray, J. R., Langbein, J. O., & Gomberg, J. S. (2014). Real-time inversions for finite fault slip models and rupture geometry based on high-rate GPS data. *Journal of Geophysical Research: Solid Earth*, *119*(4), 3201–3231.

Miyazaki, S., Larson, K. M., Choi, K., Hikima, K., Koketsu, K., Bodin, P., ... Yamagiwa, A. (2004). Modeling the rupture process of the 2003 September 25 Tokachi-Oki (Hokkaido) earthquake using 1-Hz GPS data. *Geophysical Research Letters*, *31*(21).

Moore, J. C., & Saffer, D. (2001). Updip limit of the seismogenic zone beneath the accretionary prism of southwest Japan: An effect of diagenetic to low-grade metamorphic processes and increasing effective stress. *Geology*, *29*(2), 183–186.

Nelson, A. R., Kelsey, H. M., & Witter, R. C. (2006). Great earthquakes of variable magnitude at the Cascadia subduction zone. *Quaternary Research*, *65*(3), 354–365.

Newman, A. V., Hayes, G., Wei, Y., & Convers, J. (2011). The 25 October 2010 Mentawai tsunami earthquake, from real-time discriminants, finite-fault rupture, and tsunami excitation. *Geophysical Research Letters*, *38*(5).

Nikolaidis, R. M., Bock, Y., Jonge, P. J., Shearer, P., Agnew, D. C., & Van Domselaar, M. (2001). Seismic wave observations with the Global Positioning System. *Journal of Geophysical Research: Solid Earth*, *106*(B10), 21897–21916.

Ohta, Y., Kobayashi, T., Tsushima, H., Miura, S., Hino, R., Takasu, T., ... others (2012). Quasi real-time fault model estimation for near-field tsunami forecasting based on RTK-GPS analysis: Application to the 2011 Tohoku-Oki earthquake (Mw 9.0). *Journal of Geophysical Research: Solid Earth*, *117*(B2).

Okada, Y. (1985). Surface deformation due to shear and tensile faults in a half-space. *Bulletin of the seismological society of America*, *75*(4), 1135–1154.

O'Toole, T. B., Valentine, A. P., & Woodhouse, J. H. (2012). Centroid–moment tensor inversions using high-rate GPS waveforms. *Geophysical Journal International*, *191*(1), 257–270.

Ozawa, S., Nishimura, T., Suito, H., Kobayashi, T., Tobita, M., & Imakiire, T. (2011). Coseismic and postseismic slip of the 2011 magnitude-9 Tohoku-Oki earthquake. *Nature*, *475*(7356), 373.

Petersen, M., Moschetti, M., Powers, P., Mueller, C., Haller, K., Frankel, A., ... others (2014). Documentation for the 2014 update of the National Seismic Hazard Maps. *US Geol. Surv. Open-File Rept. 2014-1091*.

Petersen, M. D., Mueller, C. S., Moschetti, M. P., Hoover, S. M., Rukstales, K. S., McNamara, D. E., ... others (2018). 2018 One-Year Seismic Hazard Forecast for the Central and Eastern United States from Induced and Natural Earthquakes. *Seismological Research Letters*, *89*(3), 1049–1061.

Polet, J., & Kanamori, H. (2000). Shallow subduction zone earthquakes and their tsunamigenic potential. *Geophysical Journal International*, *142*(3), 684–702.

Pollitz, F., & Evans, E. (2017). Implications of the earthquake cycle for inferring fault locking on the Cascadia megathrust. *Geophysical Journal International*, *209*(1), 167–185.

Popovici, R., Andonie, R., Szeliga, W. M., Melbourne, T. I., & Scrivner, C. W. (2015). Real-time monitoring of tectonic displacements in the Pacific Northwest through an array of GPS receivers. *International Journal of Computers Communications & Control*, *10*(1), 78–88.

Rubinstein, J. L., & Mahani, A. B. (2015). Myths and facts on wastewater injection, hydraulic fracturing, enhanced oil recovery, and induced seismicity. *Seismological Research Letters*, *86*(4), 1060–1067.

Ruhl, C., Melgar, D., Grapenthin, R., & Allen, R. (2017). The value of real-time GNSS to earthquake early warning. *Geophysical Research Letters*, *44*(16), 8311–8319.

Ruhl, C. J., Melgar, D., Geng, J., Goldberg, D. E., Crowell, B. W., Allen, R. M., ... others (2018). A Global Database of Strong-Motion Displacement GNSS Recordings and an Example Application to PGD Scaling. *Seismological Research Letters*, *90*(1), 271–279.

Saffer, D. M., & Tobin, H. J. (2011). Hydrogeology and mechanics of subduction zone forearcs: Fluid flow and pore pressure. *Annual Review of Earth and Planetary Sciences*, *39*, 157–186.

Saito, T., & Tsushima, H. (2016). Synthesizing ocean bottom pressure records including seismic wave and tsunami contributions: Toward realistic tests of monitoring systems. *Journal of Geophysical Research: Solid Earth*, *121*(11), 8175–8195.

Sandwell, D. T., Müller, R. D., Smith, W. H., Garcia, E., & Francis, R. (2014). New global marine gravity model from CryoSat-2 and Jason-1 reveals buried tectonic structure. *Science*, *346*(6205), 65–67.

Satake, K., Wang, K., & Atwater, B. F. (2003). Fault slip and seismic moment of the 1700 Cascadia earthquake inferred from Japanese tsunami descriptions. *Journal of Geophysical Research: Solid Earth*, *108*(B11).

Saunders, J. K., Goldberg, D. E., Haase, J. S., Bock, Y., Offield, D. G., Melgar, D., ... others (2016). Seismogeodesy using GPS and low-cost MEMS accelerometers: Perspectives for earthquake early warning and rapid response. *Bulletin of the Seismological Society of America*, *106*(6), 2469–2489.

Saunders, J. K., & Haase, J. S. (2017). Scenarios for slip characterization improvement for Cascadia subduction earthquakes by augmenting the existing onshore GNSS network with offshore observations. In *Early Warning Offshore Cascadia Workshop, Seattle, Washington.*

Saunders, J. K., & Haase, J. S. (2018). Augmenting onshore GNSS displacements with offshore observations to improve slip characterization for Cascadia subduction zone earthquakes. *Geophysical Research Letters*, *45*(12), 6008–6017.

Schmalzle, G. M., McCaffrey, R., & Creager, K. C. (2014). Central Cascadia subduction zone creep. *Geochemistry, Geophysics, Geosystems*, *15*(4), 1515–1532.

Shearer, P., & Bürgmann, R. (2010). Lessons learned from the 2004 Sumatra-Andaman megathrust rupture. *Annual Review of Earth and Planetary Sciences*, *38*.

Shi, C., Zhao, Q., Geng, J., Lou, Y., Ge, M., & Liu, J. (2008). Recent development of PANDA software in GNSS data processing. In *International conference on earth observation data processing and analysis (iceodpa)* (Vol. 7285, p. 72851S).

Shuto, N., & Fujima, K. (2009). A short history of tsunami research and countermeasures in Japan. *Proceedings of the Japan Academy, Series B*, *85*(8), 267–275.

Simons, M., Minson, S. E., Sladen, A., Ortega, F., Jiang, J., Owen, S. E., ... others (2011). The 2011 magnitude 9.0 Tohoku-Oki earthquake: Mosaicking the megathrust from seconds to centuries. *science*, *332*(6036), 1421–1425.

Singh, S. K., Pérez-Campos, X., Iglesias, A., & Melgar, D. (2012). A method for rapid estimation of moment magnitude for early tsunami warning based on coastal GPS networks. *Seismological Research Letters*, *83*(3), 516–530.

Slepian, D. (1978). Prolate spheroidal wave functions, Fourier analysis, and uncertainty?V: The discrete case. *Bell System Technical Journal*, *57*(5), 1371–1430.

Smyth, A., & Wu, M. (2007). Multi-rate Kalman filtering for the data fusion of displacement and acceleration response measurements in dynamic system monitoring. *Mechanical Systems and Signal Processing*, *21*(2), 706–723.

Somerville, P., Irikura, K., Graves, R., Sawada, S., Wald, D., Abrahamson, N., ... Kowada, A. (1999). Characterizing crustal earthquake slip models for the prediction of strong ground motion. *Seismological Research Letters*, *70*(1), 59–80.

Stewart, F. L., & Ingelson, A. (2017). Regulating energy innovation: US responses to hydraulic fracturing, wastewater injection and induced seismicity. *Journal of Energy & Natural Resources Law*, *35*(2), 109–146.

Sun, X., & Hartzell, S. (2014). Finite-fault slip model of the 2011 Mw 5.6 Prague, Oklahoma earthquake from regional waveforms. *Geophysical Research Letters*, *41*(12), 4207–4213.

Synolakis, C. E., & Bernard, E. N. (2006). Tsunami science before and beyond Boxing Day 2004. *Philosophical Transactions of the Royal Society of London A: Mathematical, Physical and Engineering Sciences*, *364*(1845), 2231–2265.

Tadokoro, K., Ikuta, R., Watanabe, T., Ando, M., Okuda, T., Nagai, S., ... Sakata, T. (2012). Interseismic seafloor crustal deformation immediately above the source region of anticipated megathrust earthquake along the Nankai Trough, Japan. *Geophysical Research Letters*, *39*(10).

Tang, L., Titov, V. V., Moore, C., & Wei, Y. (2016). Real-time assessment of the 16 September 2015 Chile tsunami and implications for near-field forecast. *Pure and Applied Geophysics*, *173*(2), 369–387.

Tanioka, Y. (2018). Tsunami simulation method assimilating ocean bottom pressure data near a tsunami source region. *Pure and applied geophysics*, *175*(2), 721–729.

Tanioka, Y., & Satake, K. (1996). Tsunami generation by horizontal displacement of ocean bottom. *Geophysical Research Letters*, *23*(8), 861–864.

Tatehata, H. (1997). The new tsunami warning system of the Japan Meteorological Agency. In *Perspectives on Tsunami Hazard Reduction* (pp. 175–188). Springer.

Titov, V. V., Gonzalez, F. I., Bernard, E., Eble, M. C., Mofjeld, H. O., Newman, J. C., & Venturato,

A. J. (2005). Real-time tsunami forecasting: Challenges and solutions. *Natural Hazards*, *35*(1), 35–41.

Trifunac, M. (1974). A three-dimensional dislocation model for the San Fernando, California, earthquake of February 9, 1971. *Bulletin of the Seismological Society of America*, *64*(1), 149–172.

Trifunac, M., & Todorovska, M. (2001). A note on the useable dynamic range of accelerographs recording translation. *Soil Dynamics and Earthquake Engineering*, *21*(4), 275–286.

Tsushima, H., Hino, R., Fujimoto, H., Tanioka, Y., & Imamura, F. (2009). Near-field tsunami forecasting from cabled ocean bottom pressure data. *Journal of Geophysical Research: Solid Earth*, *114*(B6).

Tsushima, H., Hino, R., Tanioka, Y., Imamura, F., & Fujimoto, H. (2012). Tsunami waveform inversion incorporating permanent seafloor deformation and its application to tsunami forecasting. *Journal of Geophysical Research: Solid Earth*, *117*(B3).

Tsushima, H., & Ohta, Y. (2014). Review on near-field tsunami forecasting from offshore tsunami data and onshore GNSS data for tsunami early warning. *Journal of Disaster Research*, *9*(3), 339–357.

Uchiike, H., & Hosono, K. (1995). Japan tsunami warning system; present status and future plan. In *Tsunami: Progress in prediction, disaster prevention and warning* (pp. 305–322). Springer.

Uehira, K., Kanazawa, T., Noguchi, S.-i., Aoi, S., Kunugi, T., Matsumoto, T., ... others (2012). Ocean bottom seismic and tsunami network along the Japan Trench. In *AGU Fall Meeting Abstracts.*

University of Washington. (2017).
In *Early Warning Offshore Cascadia Workshop, Seattle, Washington.*

Wald, D. J., Quitoriano, V., Heaton, T. H., Kanamori, H., Scrivner, C. W., & Worden, C. B. (1999). TriNet "ShakeMaps": Rapid generation of peak ground motion and intensity maps for earthquakes in southern California. *Earthquake Spectra*, *15*(3), 537–555.

Walsh III, F. R., & Zoback, M. D. (2016). Probabilistic assessment of potential fault slip related to injection-induced earthquakes: Application to north-central Oklahoma, USA. *Geology*, *44*(12), 991–994.

Wang, K., & Hu, Y. (2006). Accretionary prisms in subduction earthquake cycles: The theory of dynamic Coulomb wedge. *Journal of Geophysical Research: Solid Earth*, *111*(B6).

Wang, R., Parolai, S., Ge, M., Jin, M., Walter, T. R., & Zschau, J. (2013). he 2011 M w 9.0 Tohoku

earthquake: Comparison of GPS and strong-motion data. *Bulletin of the Seismological Society of America*, *103*(2B), 1336–1347.

Wang, R., Schurr, B., Milkereit, C., Shao, Z., & Jin, M. (2011). An improved automatic scheme for empirical baseline correction of digital strong-motion records. *Bulletin of the Seismological Society of America*, *101*(5), 2029–2044.

Whitmore, P., ten Brink, U., Caropolo, M., Huerfano-Moreno, V., Knight, W., Sammler, W., & Sandrik, A. (2009). NOAA/West Coast and Alaska Tsunami Warning Center Atlantic Ocean response criteria. *Science of Tsunami Hazards*, *28*(2), 86–107.

Wright, T. J., Houlié, N., Hildyard, M., & Iwabuchi, T. (2012). Real-time, reliable magnitudes for large earthquakes from 1 Hz GPS precise point positioning: The 2011 Tohoku-Oki (Japan) earthquake. *Geophysical Research Letters*, *39*(12).

Wu, Y.-M., & Wu, C.-F. (2007). Approximate recovery of coseismic deformation from Taiwan strong-motion records. *Journal of Seismology*, *11*(2), 159–170.

Yanagi, B. S. (n.d.). Tsunami preparedness in Hawaii. *(Coastal earthquakes and tsunamis: Reducing the risks*.

Yang, Y., Dunham, E. M., Barnier, G., & Almquist, M. (2019). Tsunami wavefield reconstruction and forecasting using the ensemble Kalman filter. *Geophysical Research Letters*.

Yeck, W., Hayes, G., McNamara, D. E., Rubinstein, J. L., Barnhart, W., Earle, P., & Benz, H. M. (2017). Oklahoma experiences largest earthquake during ongoing regional wastewater injection hazard mitigation efforts. *Geophysical Research Letters*, *44*(2), 711–717.

Yokota, Y., Ishikawa, T., Sato, M., Watanabe, S.-i., Saito, H., Ujihara, N., ... others (2015). Heterogeneous interplate coupling along the Nankai Trough, Japan, detected by GPS-acoustic seafloor geodetic observation. *Progress in Earth and Planetary Science*, *2*(1), 10.

Yokota, Y., Koketsu, K., Fujii, Y., Satake, K., Sakai, S., Shinohara, M., & Kanazawa, T. (2011). Joint inversion of strong motion, teleseismic, geodetic, and tsunami datasets for the rupture process of the 2011 Tohoku earthquake. *Geophysical Research Letters*, *38*(7).

Yun, N.-Y., & Hamada, M. (2014). Evacuation Behavior and Fatality during the 2011 Tohoku Tsunami. *Science of Tsunami Hazards*, *33*(3).

Zhao, X., Duputel, Z., & Yao, Z. (2017). Regional W-Phase Source Inversion for Moderate to Large Earthquakes in China and Neighboring Areas. *Journal of Geophysical Research: Solid Earth*, *122*(12).

Zhu, L., & Rivera, L. A. (2002). A note on the dynamic and static displacements from a point

source in multilayered media. *Geophysical Journal International*, *148*(3), 619–627.

Zumberge, J., Heflin, M., Jefferson, D., Watkins, M., & Webb, F. H. (1997). Precise point positioning for the efficient and robust analysis of GPS data from large networks. *Journal of Geophysical Research: Solid Earth*, *102*(B3), 5005–5017.

Zumberge, M. A. (1997). Precise optical path length measurement through an optical fiber: Application to seafloor strain monitoring. *Ocean Engineering*, *24*(6), 531–542.